Imaging Mass Spectrometry of Biomolecules Using Massive Cluster Impact

by

Jitao Zhang

A Dissertation Presented in Partial Fulfillment
of the Requirements for the Degree
Doctor of Philosophy

Approved July 2015 by the
Graduate Supervisory Committee:

Peter Williams, Chair
Mark Hayes
Randall Nelson

ARIZONA STATE UNIVERSITY

August 2015

ABSTRACT

Massive glycerol cluster ions with many charges (~ 10^6 Da, ~ ±100 charges) have been generated by electrospray to bombard biomolecules and biological sample surfaces. The low impact energy per nucleon facilitates intact sputtering and ionization of biomolecules which can be subsequently imaged. Various lipids, peptides and proteins have been studied. The primary cluster ion source has been coupled with an ion-microscope imaging mass spectrometer (TRIFT-1, Physical Electronics). A lateral resolution of ~3 μm has been demonstrated, which is acceptable for sub-cellular imaging of animal cells (e.g. single cancer cell imaging in early diagnosis). Since the available amount of target molecules per pixel is limited in biological samples, the measurement of useful ion yields (ratio of detected molecular ion counts to the sample molecules sputtered) is important to determine whether enough ion counts per pixel can be obtained. The useful ion yields of several lipids and peptides are in the 1-3 ×10^{-5} range. A 3 ×3 μm^2 lipid bilayer can produce ~260 counts/pixel for a meaningful 3 ×3 μm^2 pixel ion image. This method can probably be used in cell imaging in the future, when there is a change in the lipid contents of the cell membrane (e.g. cancer cells vs. normal cells).

ACKNOWLEDGMENTS

First of all, I want to express my sincere gratitude to my advisor, Professor Peter Williams, for his instruction and support on my Ph.D. study. He is one of the best teachers and advisors I have ever met. His profound knowledge, patience and kind consideration for students helped me a lot in my graduate study.

Besides my advisor, I want to thank Professor Mark Hayes and Professor Randall W. Nelson for their insightful comments on my thesis.

I want to thank my wife, Mian Yang, for her understanding and support throughout these five years at ASU and my parents for their encouragement in my Ph.D. process.

My sincere thanks also go to Dr. Klaus Franzreb, Dr. Maitrayee Bose, Dr. Sergei A. Aksyonov, Dr. Adam Monroe, Dr. Rick Sobers and Dr. Timothy Steimle for their help in the projects for my thesis.

I thank John Mahoney for the discussion of MCI source set-up, Physical Electronics (Dr. Scott Bryan) for the donation of TRIFT-I, Micron (Dr. Steve Hues) for the donation of TRIFT-II, Dr. Alexandra Ros for donating the microchannel sample, Dr. Ian Gilmore (NPL) for donating organic delta layer sample, Dr. Jiro Matsuo for donating α-NPD and 2-TNATA samples, and Dr. Joshua Labaer for donating cancer cell samples.

TABLE OF CONTENTS

Page

CHAPTER Page

CHAPTER Page

LIST OF TABLES

LIST OF FIGURES

Figure Page

Figure Page

Figure Page

CHAPTER 1

INTRODUCTION TO IMAGING MASS SPECTROMETRY

Imaging of biological structures in the past centuries has enhanced our understanding of the biological world. Optical microscopy allowed the discovery of cells (Robert Hooke 1665) which are the basic units for living organisms. This is still one of the most popular bioimaging methods nowadays. The introduction of fluorescence microscopy allowed localization of target molecules inside the biological structure (Ghiran 2011). Common fluorescent labeling strategies include small molecule staining (DAPI for DNA (Kapuscinski 1995)), fluorescent antibodies (Kawamura 1969) and green fluorescent protein (GFP) (Ormo et al. 1996). Confocal laser scanning microscopy (CLSM) provides 3D high resolution optical images (Cremer and Cremer 1978). Electron microscopy uses an electron beam instead of light. Because the wavelength of the electron is much shorter than that of light photons, it can resolve structures smaller than one nanometer (Erni et al. 2009) producing spectacular images of cells. But these two bioimaging methods exhibit a limitation that they are blind to molecular information without labeling. In optical microscopy, target molecules can be labeled with fluorescent tags in order to be visible. In electron microscopy, immunogold labeling (Faulk 1971)or staining is used to locate specific target biomolecules.

1.1 Immunohistochemistry

Immunohistochemistry is a well-established method in disease diagnosis, drug development and biological research. Antibodies are used to detect antigens (e.g. proteins)

through their specific binding in a tissue sample. In order to visualize the antibody-antigen interaction, fluorophores or enzymes are added to the antibody.

The general process of immunohistochemistry involves: tissue collection (e.g. biopsy); tissue fixation (e.g. formaldehyde); tissue embedding (e.g. paraffin); sectioning and mounting; epitope recovery; blocking nonspecific sites; sample labeling; sample visualization through optical microscope; morphological information; pathological diagnosis (Overview of Immunohistochemistry, Life Technologies, Thermo Fisher Scientific Inc.).

Due to the light wavelength, the best spatial resolution for an optical microscope is limited to ~ 200 nm. But this resolution is enough to produce spectacular images of cells (prokaryotes ~1-5 μm and eukaryotes ~10-30 μm). Usage of fluorescence or enzymatic amplification makes this method highly sensitive. Both of these two merits make it a widely used technology.

Immunohistochemistry has been studied extensively using tags (e.g. antibody) for cancer diagnosis. For example, Wei Huang at University of Wisconsin-Madison found that the expression of Spermidine/Spermine N1-Acetyl Transferase (SSAT) and the enzyme protein in human prostate cancer (PCa) is related to the cancer progression and metastasis(Huang et al. 2015). Two tissue microarrays (TMA) were used for the verification: progression TMA (pTMA) and outcome TMA (oTMA) (tissues were collected from 1999 to 2005 and followed until 2015 for disease outcome). The pTMA includes benign prostate hyperplasia (BPH), benign prostate tissues (BPT), high-grade intraepithelial neoplasia (HGPIN), localized PCa (PCa_local), aggressive PCa (PCa_aggr)

and metastatic PCa (Met). The oTMA includes none recurrence, biochemical recurrence and cancer recurrence (local or distant). Figure 1 shows the increased expression level of SSAT mRNA and SSAT protein from noncancerous to cancerous tissues and from no recurrence to cancer recurrence. The SSAT mRNA and SSAT protein might serve as a biomarker for prostate cancer grading and prognosis.

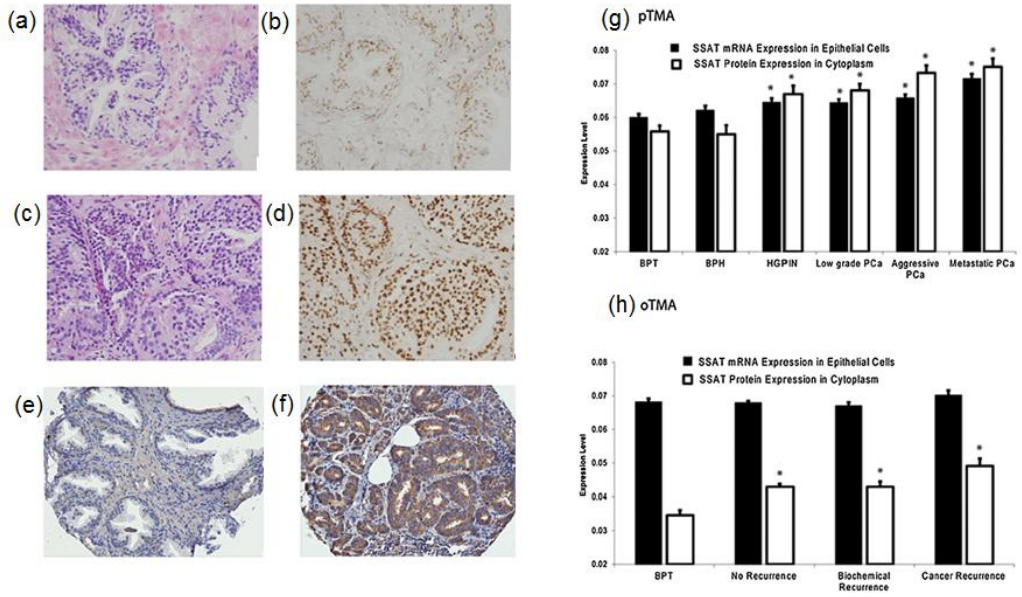

Figure 1. (a), normal epithelium sample by H&E; (b): normal epithelium tissue stained by RNA-ISH for SSAT mRNA; (c): patient biopsy tissue containing PCa stained by H&E; (d): patient biopsy tissue containing PCa stained by RNA-ISH for SSAT mRNA; (e): benign prostate tissue (BPT) stained by anti-SSAT antibody for SSAT enzyme protein; (f): prostate cancer tissue stained by anti-SSAT antibody for SSAT enzyme protein. (g): expression level of SSAT mRNA and SSAT protein increases from BPT (benign prostate tissue) to metastatic PCa; (h): expression level SSAT mRNA and SSAT protein increases from no recurrence to cancer recurrence samples. Reprinted with permission from Huang et al. (2015), Copyright 2015 Wiley Periodicals, Inc.

Although immunohistochemistry is widely used in disease diagnosis and biological research, it still has several limitations. For example, (1): it requires prior knowledge of the biomarker. The right antibody can be chosen only after the antigen is clearly known; (2): the antibody is expensive (a few hundred dollar at microgram); (3): in a single measurement, only one or several target molecules can be labeled; (4): lipid changes have been demonstrated to be associated with many diseases (e.g. cancer), but immunohistochemistry is not well-suited to image lipids; (5): complicated sample processing in immunohistochemistry makes the measurement time long (hours to days).

1.2 Imaging Mass Spectrometry

Imaging mass spectrometry (IMS), a technique derived from mass spectrometry, can provide a solution to the problems discussed above. The mechanism of IMS is different from immunohistochemistry. In mass spectrometry, molecules in a sample tissue are ejected as ions into the gas phase and extracted into a mass analyzer. The mass/charge ratios of the sample molecular ions are measured by magnetic or time of flight mass spectrometry. Moreover, tandem mass spectrometry can provide structural information of the molecules by fragmenting the parent molecules. In this way, sample molecules can be identified without the help of labeling. In imaging mass spectrometry, the spatial distribution of target molecules can be revealed by ejecting them with a spatially focused beam of photons or ions or using a microscope ion imaging mass spectrometer.

Advantages of IMS are: (1): tag (e.g. antibody) free; (2): simultaneous acquisition/imaging of many species; (3): potential biomarker discovery through the whole spectrum imaging; (4): well-suited for lipid imaging. Details are explained below.

1.2.1 MALDI Imaging

A typical MALDI (Matrix-Assisted Laser Desorption/Ionization) imaging mass spectrometry process is illustrated by Caprioli et al. (Stoeckli et al. 2001)at Figure 2 (reprinted with permission from Stoeckli et al. (2001), Copyright 2001 Nature Publishing Group). A section of frozen brain tissue was placed on a metal target. The tissue sample was coated with a MALDI matrix solution. The sample molecules are dissolved into a matrix solution. When the solution is being dried, the sample molecules co-crystallize with the matrix molecules. A pulsed laser beam is used to irradiate the sample surface, spot by spot. When the matrix molecules absorb photons from the laser beam, they become superhot and a small volume of the matrix explodes (Chou, Nelson, and Williams 2009). The explosion process ejects the ionized sample molecules into the gas phase. From each spot, a full spectrum was displayed with various molecular peaks. When a specific peak was chosen, its distribution inside the brain tissue was obtained. MALDI can eject intact molecular ions up to one MDa (Nelson, Dogruel, and Williams 1994). The invention of MALDI has a huge impact on the way people do imaging mass spectrometry of biological samples. Imaging of lipids (Chughtai et al. 2013), peptides (Cillero-Pastor et al. 2013; Stauber et al. 2010), proteins (Chaurand et al. 2008) in tissue samples has been done.

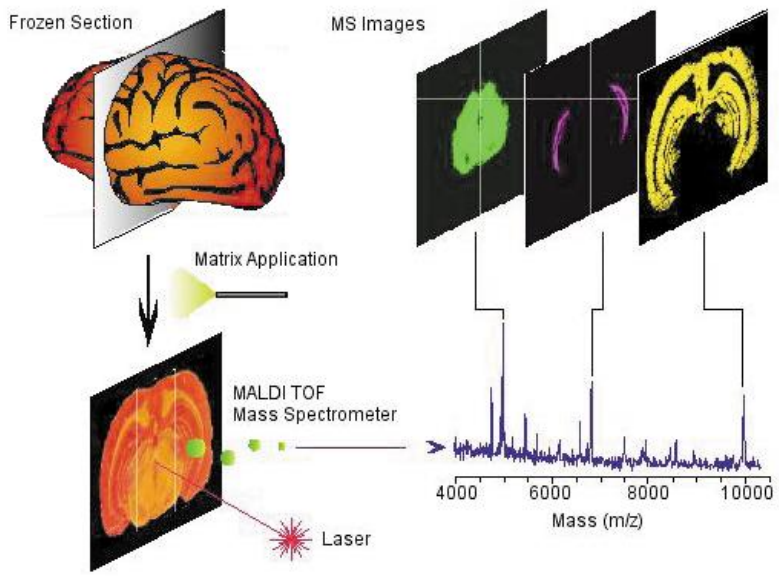

Figure 2. MALDI imaging process of a frozen brain tissue sample (Stoeckli et al. 2001). The surface of a sliced frozen brain tissue was coated with matrix solution. Scanning of laser beam on the surface revealed the distribution of molecules for each peak. Reprinted with permission from Stoeckli et al. (2001), Copyright 2001 Nature Publishing Group.

Professor Richard M. Caprioli at Vanderbilt University has done extensive research using MALDI imaging for biomarker discovery, disease diagnosis, proteomics and so on. An example of MALDI imaging in biomarker discovery was shown by Caprioli et al. (Chaurand, Schwartz, and Caprioli 2004) (Figure 3). A mouse brain tissue sample with a tumor section and normal section adjacent was tested by MALDI imaging. Imaging of many ion species simultaneously shows preferred distribution of some ions either in the tumor region or the normal region. For example, m/z 6924, 9910 (acyl coA-binding protein), 11,307 and 11,348 (histone H4), 13,804 and 15,350 (histones H2B1 and

H3) and m/z 24,807 are concentrated in the tumor region. These molecules maybe can serve as potential biomarkers for the mouse brain tumor.

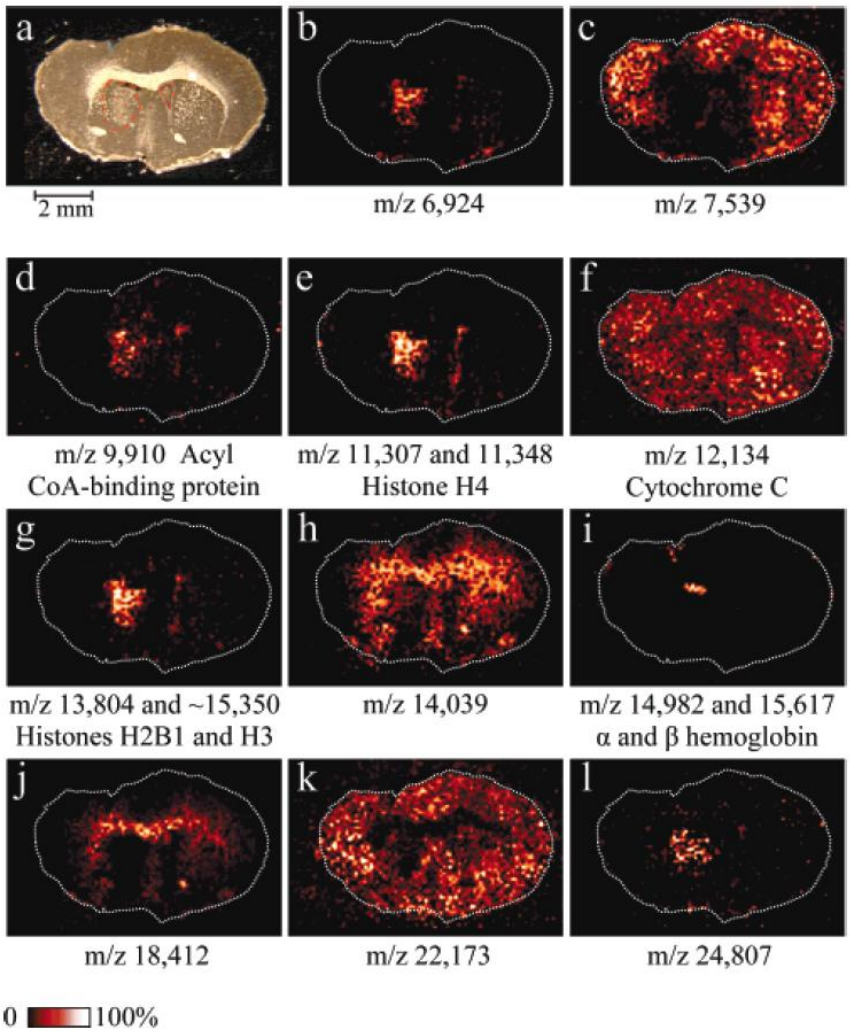

Figure 3. MALDI imaging of a mouse brain tissue with a tumor section and normal section adjacent. (A): Optical image of the mouse brain with the tumor area circled by red dots; (B-L): ion images of various m/z species. Some ions distribution are associated with the tumor specifically. These ions might serve as potential biomarker for the mouse brain tumor. Imaging resolution is ~110 μm. Reprinted with permission from Chaurand, Schwartz, and Caprioli (2004), Copyright 2004 American Chemical Society.

Imaging mass spectrometry has also been demonstrated to be successful using cell lipids. There are several reasons for this. First, the cell membrane lipids are abundant compared with proteins inside the cells. Second, the lipids are located at the outside surface of cells making them easily accessible for imaging. Third, lipid molecules are readily ionized including a phosphate and a quaternary ammonium center. All of these reasons make lipid a good target for imaging mass spectrometry. Various studies have shown that there is dramatic lipid changes in cancer cells compared with normal cells. For example, Shimma et al. (Shimma et al. 2007) demonstrated abnormal phospholipids distribution in human colon cancer liver metastasis (Figure 4). An increased expression of lipid at m/z 725.5 and a decreased expression of lipid at m/z 616.1 were observed in the cancer region compared with the normal region.

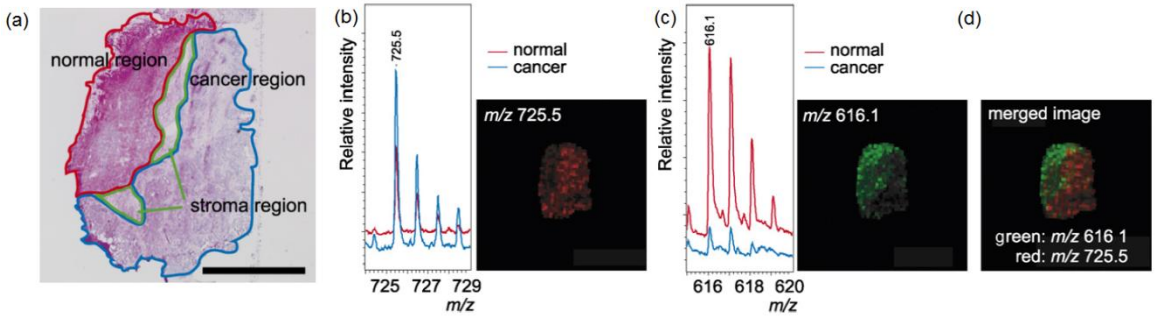

Figure 4. (a). Optical image of a H&E stained tissue sample obtained from a patient with colon cancer liver metastasis; (b): MALDI spectrum and ion image of m/z 725.5 show an increased expression in cancer region; (c): MALDI spectrum and ion image of m/z 616.1 show a decreased expression in cancer region. Reprinted with permission from Shimma et al. (2007), Copyright 2007 Elsevier B.V.

Guo et al. did MALDI imaging of cancer tissues and normal tissues for six different types of human cancers (thyroid cancer, gastric cancer, lung cancer, esophageal cancer, colorectal cancer and breast cancer) (Guo et al. 2014). Expression was different for various lipids between the cancer tissues and normal tissues (Figure 5).

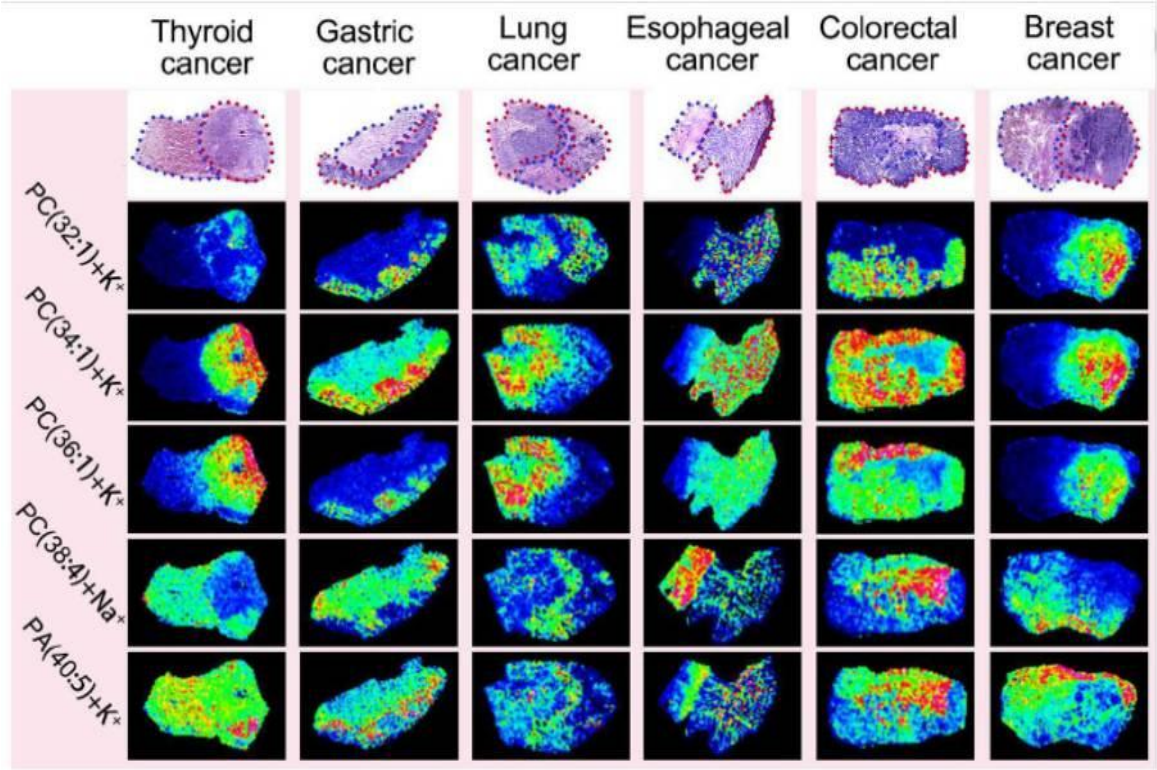

Figure 5. Top: Optical images of H&E stained tissue (red dots represented cancerous area, blue dots represented normal area). Lower: Dramatic differences for various lipids (PC: phosphatidylcholine, PA: phosphatidic acid) with different cancer tissue samples were observed by MALDI imaging. Spatial resolution was 200 μm. Reprinted with permission from Guo et al. (2014).

A direct comparison of H&E stained optical image and a MALDI image was demonstrated by Caprioli (Caprioli 2015). Figure 6 displays an optical image of a

transverse section of mouse brain (stained with hematoxylin/eosin) (left side) and an ion image of a lipid PI (38:4) (m/z 885.6) (right side). The lipid ion image provides another type of vision into the tissue sample compared with the H&E stained optical image. The scale bar is 1 mm. The ion image acquisition time is 35 hours.

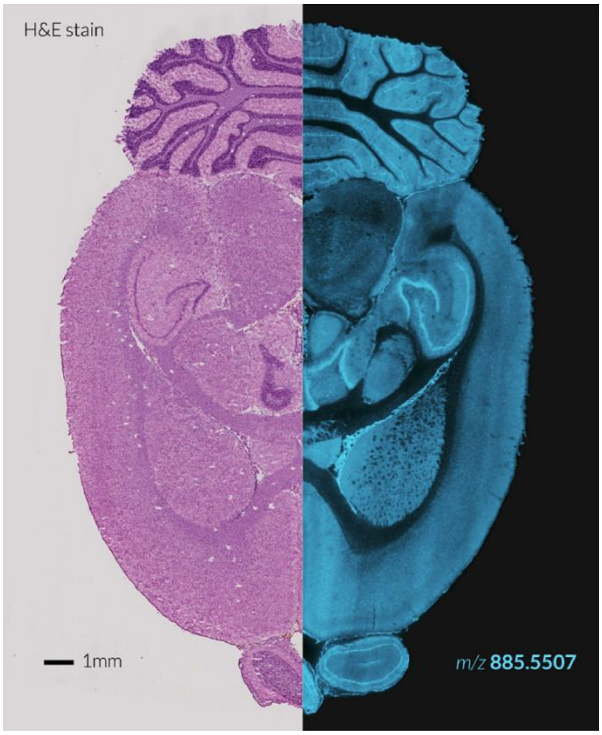

Figure 6. (left): optical image of a mouse brain section; (right): ion image of PI(38:4) (m/z 885.6). Spatial resolution is ~15 µm. Scale bar is 1 mm. The acquisition time for the ion image is 35 hours (0.35s/pixel, 364,740 pixels). Reprinted with permission from Caprioli (2015), Copyright 2015 American Society for Mass Spectrometry.

Higher spatial resolution (smaller laser spot diameter ~1 µm) MALDI imaging for proteins has been performed by Caprioli et al. (Zavalin et al. 2015) (Figure 7).

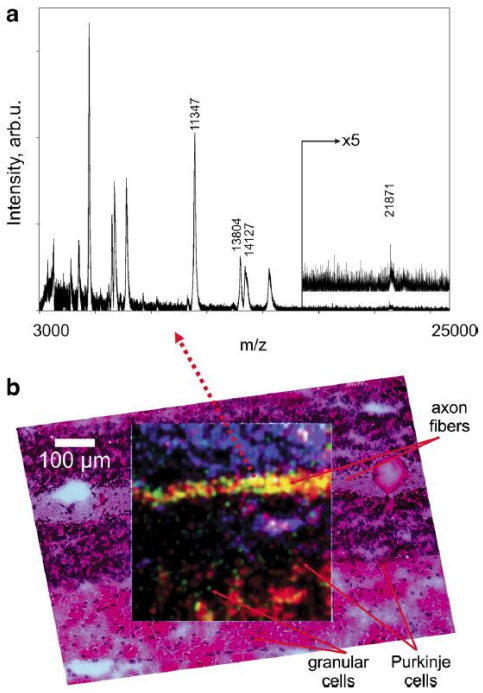

Figure 7. MALDI imaging of mouse cerebellum with 1 µm laser spot diameter. Red color represents m/z 14127 (myelin basic proteins); green color represents m/z 13804 (histone H2B); blue color represents m/z 11347 (histone H4). The scale bar is 100 µm. Reprinted with permission from Zavalin et al. (2015), Copyright 2015 Springer.

There are several limitations for MALDI imaging described above: (1): long imaging time, the ion image is formed by rastering a focused laser beam on the sample surface pixel by pixel; (2): matrix smear effect, the sample molecules need to be dissolved into the matrix solution then re-crystallized, thus they can move away from their original positions in the solution. The smear effect limits spatial resolution to ~10 µm (Passarelli et al. 2014) (Figure 8). A patterned sample with alternated PEG and lipid stripes was used to test the matrix smear effect. Migration of PEG and lipid molecules from their original position has been observed.

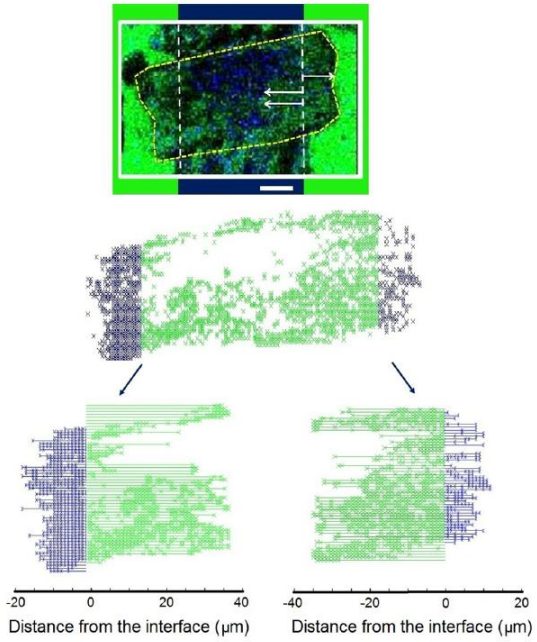

Figure 8. Matrix smear effect test. A test device with alternated stripe of polyethylene glycol (PEG) (blue color) and PC(16:0/16:0) (green color) was analyzed by TOF-SIMS with Bi_3^+ primary ion beam. After the application of a MALDI matrix (DHB), migration of PEG and lipid molecules are observed. The average migration distance of lipid and PEG is ~16 μm and ~6 μm accordingly. Reprinted with permission from Passarelli et al. (2014), Copyright 2014 American Chemical Society.

1.2.2 DESI Imaging

Desorption Electrospray Ionization is another popular imaging mass spectrometry method which uses electrospray in atmosphere to splash the sample surface. One major advantage for this method is that it can do ambient desorption and ionization. Samples do not need to be loaded into vacuum. This method can provide in situ analysis (e.g.

physician can use it to determine the boundary of cancer and normal tissue while removing the cancer tissue in a surgery).

The imaging is realized through scanning an electrospray ion beam on sample surface. First, the sample surface becomes coated with the electrospray solution in which the molecules at the surface can dissolve. Then, subsequent droplet impacts can splash the dissolved sample molecules into the gas phase. The splashed droplets are drawn into a mass spectrometer and heated to evaporate the solvent and produce free molecular ions. The intact mass range can go up to 66 kDa (Venter, Nefliu, and Cooks 2008). DESI has been used for imaging of lipids (Venter, Nefliu, and Graham Cooks 2008; Girod et al. 2010; Eberlin, Ferreira, et al. 2011; Eberlin, Liu, et al. 2011; Ellis et al. 2010) and peptides (Eberlin, Liu, et al. 2011) in tissue samples. Various applications have been developed for DESI. Some typical applications are listed below (Dill et al. 2011) (Figure 9) including cancer diagnosis (e.g. biomarker discovery), forensic analysis, drug discovery and so on.

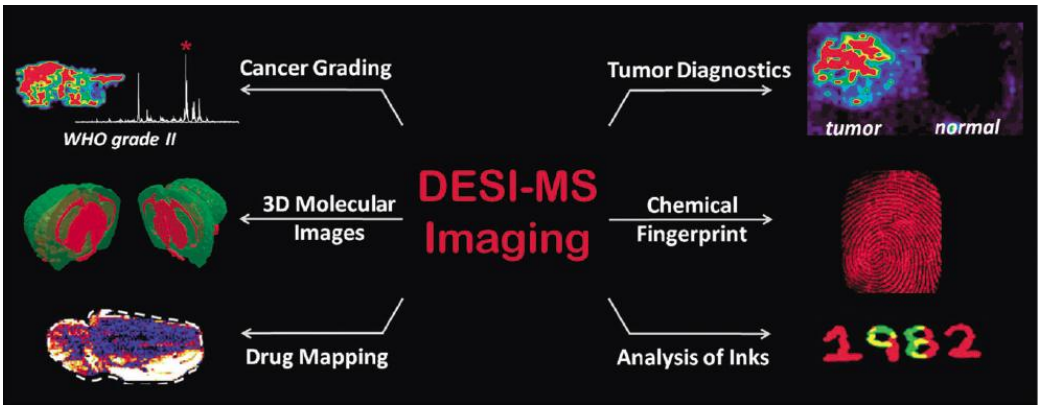

Figure 9. Applications of DESI include cancer grading, 3D molecular images, drug mapping, tumor diagnostics, chemical fingerprint and analysis of inks. Reprinted with permission from Dill et al. (2011), Copyright 2011 The Royal Society of Chemistry.

Graham Cooks and his colleagues at Purdue University demonstrated dramatic lipid pattern differences between the human papillary renal cancer tissues and normal tissues using DESI (Figure 10) (Eberlin, Ferreira, et al. 2011; Eberlin et al. 2012). Spatial resolution was low but the image contrast was high.

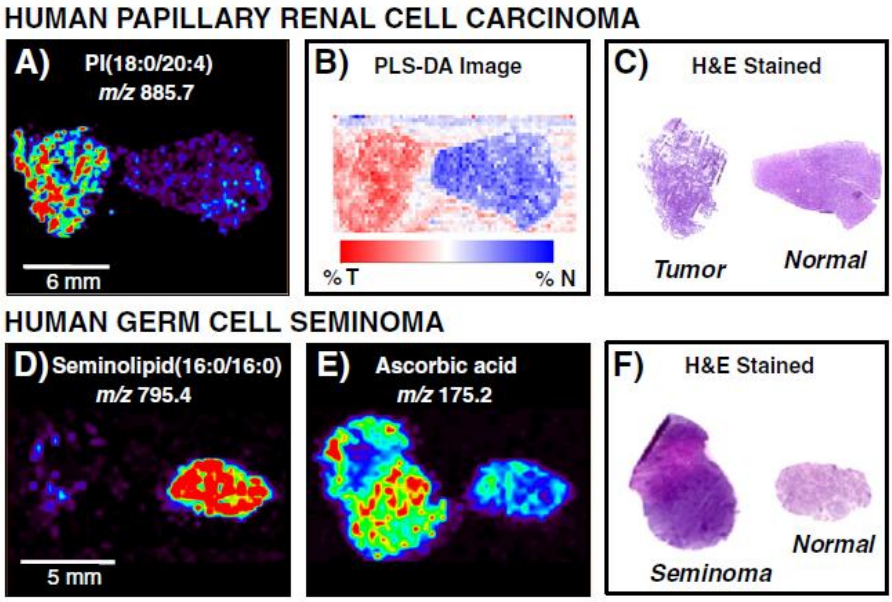

Figure 10. In human papillary renal cell carcinoma, a higher expression of lipid PI (Phosphatidylinositol) (18:0/20:4) (m/z 885.7) was observed compared with normal tissue by DESI imaging. A lower expression of seminolipid (16:0/16:0) (m/z 795.4) was observed in human germ cell seminoma compared with normal tissue. Reprinted with permission from Eberlin et al. (2011), Copyright 2011 Elsevier B.V.

One limitation of DESI is the imaging resolution. It is difficult to focus an electrospray beam in atmosphere. The lateral resolution is ~200 μm which is not enough for sub-cellular imaging (Venter, Nefliu, and Graham Cooks 2008).Attempts have been made to improve the DESI spatial resolution. One example is to shrink the capillary

diameter. Laskin et al. used Nanospray to do ambient desorption and ionization. The spatial resolution achieved is ~10 μm (Laskin et al. 2012) (Figure 11).

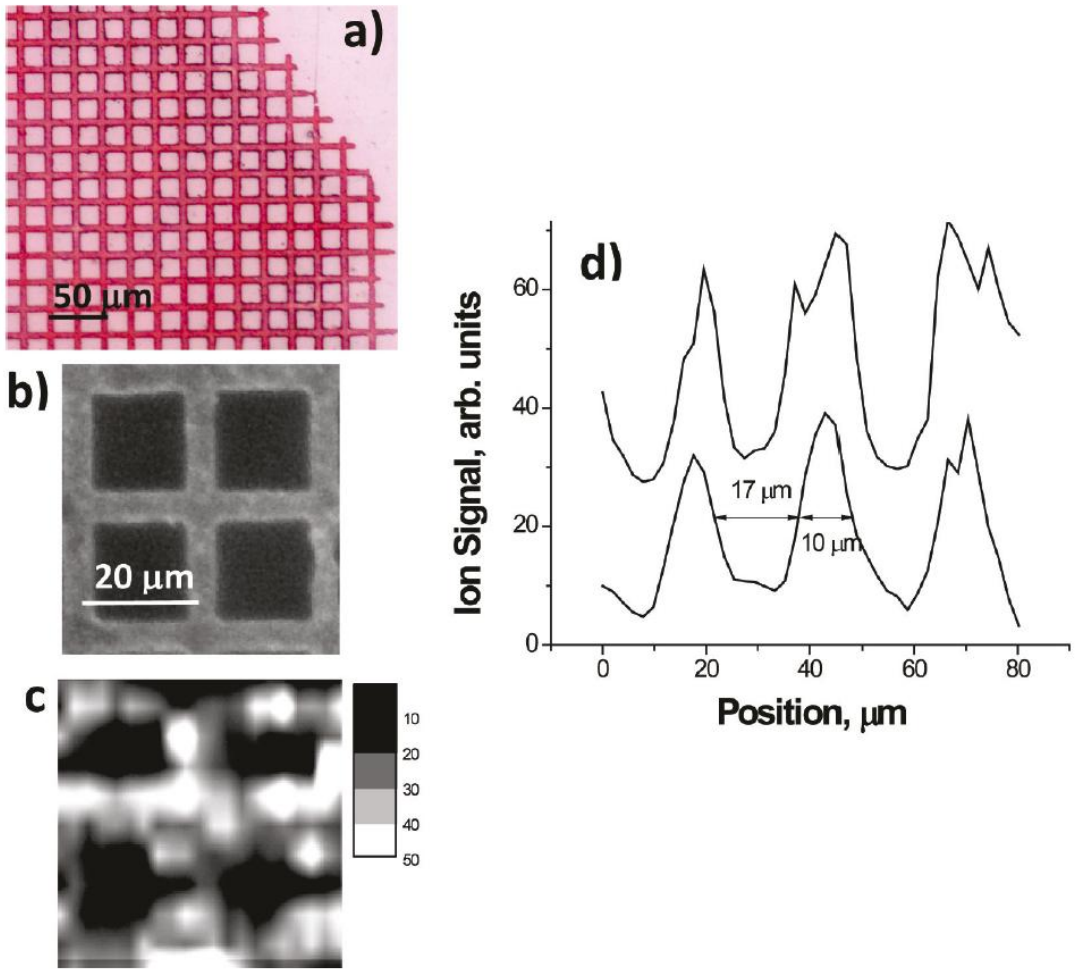

Figure 11. Spatial resolution test with nanospray desorption electrospray ionization. (a): optical image of a rhodamine grid; (b): higher magnification optical image of 2 ×2 grids; (c): Ion image of the grids in (b); (d): line scan and plot profile showing a spatial resolution ~ 10 μm. Reprinted with permission from Laskin et al. (2012), Copyright 2011 American Chemical Society.

1.2.3 SIMS with Atomic Ion Beam

In SIMS (secondary ion mass spectrometry), a primary ion beam sputters and ionizes sample molecules producing secondary ions (Figure 12). These secondary ions are accelerated by an extraction electric field into the mass spectrometer composed of electrostatic and magnetic sectors, or a field free drift region. Different m/z ions have different trajectories in the magnetic field or different flight time in a field free drift region. Through different trajectories or flight time, their mass to charge ratio can be measured.

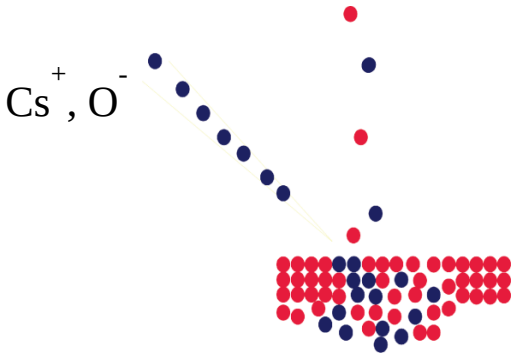

Figure 12. Secondary Ion Mass Spectrometry with atomic primary ion beam (e.g. Cs^+,O^-). Focused primary atomic ion beam is used to raster the sample surface. Ionized sample molecules and fragments are sputtered into the gas phase. Extensive surface and in-depth fragmentation of sample molecules is produced.

SIMS using atomic primary ions has been studied and developed for more than 50 years (Castaing and Slodzian 1961). Image resolution of ~50 nm (Slodzian et al. 1992; Lechene et al. 2006) has been achieved for NanoSIMS (developed by AMETEK, Inc. - CAMECA). The primary ions are usually accelerated to 16 keV. The primary ions with

high energy density damage the sample molecules extensively and generate mainly atomic secondary ions and small fragments, e.g. CN^-. It is difficult to get intact molecular secondary ions larger than a few hundred Da. The applications for this method are mainly in semiconductors (Kachan et al. 2004; Kudriavtsev et al. 2011), materials science (Thomen, Robert, and Remusat 2014), geology (Badro et al. 2007; Floss et al. 2006) and biological research with isotopic labeling (Tanji et al. 2008; Weber et al. 2010; Romer et al. 2006).

Dr. Claude Lechene at Harvard developed the Multi-isotope Imaging Mass Spectrometry (MIMS) based on the NanoSIMS from Cameca Inc (France). The biological samples are cultured in an isotopically labeled medium. Through the isotope enrichment at certain area inside the cell, a quantitative color contrast can be built to reveal the features of the cell. One example is to incorporate the cell with ^{15}N-thymidine (Steinhauser et al. 2012). The ^{15}N-thymidine is a material used in the DNA synthesis. So it is preferably concentrated inside the cell nucleus. In Figure 13, a fibroblast cell was labeled with the ^{15}N-thymidine. The left image in Figure 13 is an optical image obtained with differential contrast reflection microscopy. The central image is the ion image of ^{14}N which is the naturally most abundant isotope of nitrogen. The image of the $^{15}N/^{14}N$ ratio (right) shows the contrast of cell nucleus compared with the rest of the cell (^{15}N-thymidine is concentrated at the nucleus region). The scale bar is 10 μm.

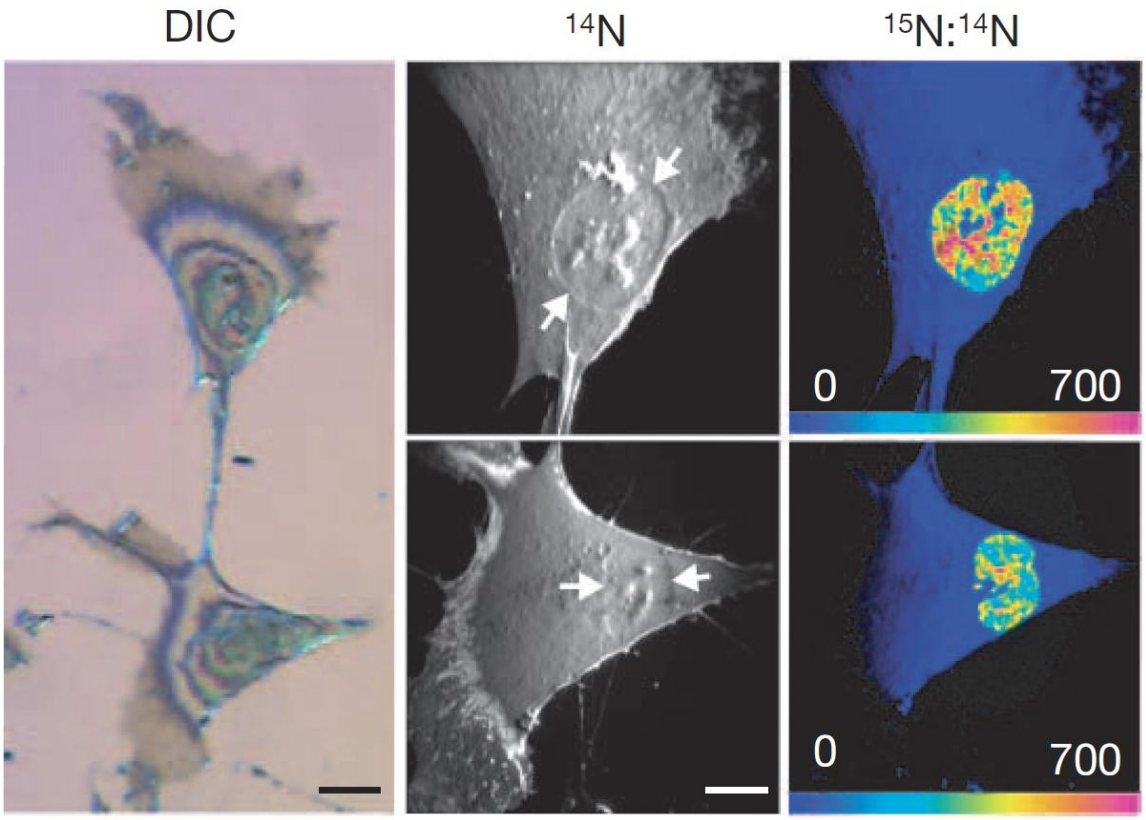

Figure 13. (a): Differential interference contrast reflection microscopy image of fibroblast cells; (b): Ion image of ^{14}N; (c): $^{15}N/^{14}N$ ion image shows a color contrast between the cell nucleus and the rest of the cell (the color scale represents ratio of $^{15}N/^{14}N$ from 0 to 700). The scale bar is 10 μm. Reprinted with permission from Steinhauser et al. (2012), Copyright 2012 Macmillan Publishers Limited.

Another example of high resolution imaging on a biological sample was demonstrated by Mary Kraft et al. (Frisz et al. 2013) using the NanoSIMS (Figure 14). Sphingolipid and cholesterol in the cell plasma membrane (clone 15 cell line) were labeled with ^{15}N and ^{18}O correspondingly. Through the isotope enrichment ($^{12}C^{15}N^-/^{12}C^{14}N^-$ or $^{18}O^-/^{16}O^-$ ratio), the cholesterol was found to be evenly distributed in the cell

membrane, whereas the distribution of sphingolipid was unevenly (concentrated at multiple locations). This experiment demonstrated that cholesterol and sphingolipid are not co-localized to form lipid rafts. This is different with prior understanding of the roles of sphingolipid and cholesterol in the cell membrane.

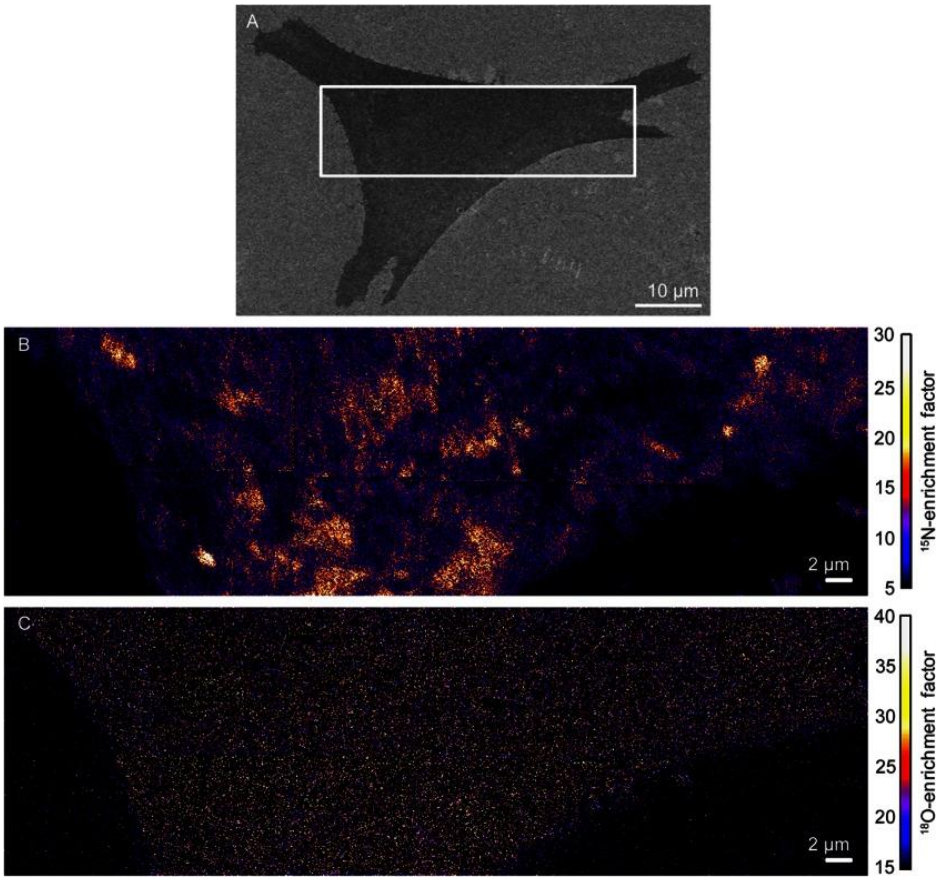

Figure 14. (a): SEM image of the cell membrane (clone 15 cell line); (b): ^{15}N enrichment high resolution image; (c): ^{18}O enrichment high resolution image. The evenly distributed ^{18}O-cholesterol and unevenly distributed ^{15}N-sphingolipids in the plasma membrane of a clone 15 cell revealed that sphingolipids and cholesterol are not co-localized in the cell membrane to form lipid rafts (Frisz et al. 2013). The scale bar is 2 µm.

1.2.4 C_{60} SIMS

Another IMS method uses a C_{60} primary ion beam instead of the atomic primary ion beam (Figure 15). Since C_{60} has a higher molecular weight (720 Da), the energy per nucleon (13.9 eV/nucleon with 10 kV) is smaller than for atomic ion beams (e.g. O^- 625eV/nucleon with 10 kV) with the same acceleration voltage. Smaller energy density helps in reducing fragmentation and increasing the survival probability for intact molecular ions. C_{60} SIMS can sputter and ionize intact molecules in the mass range up to a few hundred Da, but there is still a significant amount of fragmentation. A spatial resolution of ~250 nm has been achieved (Winograd 2005). C_{60} SIMS has been used broadly in imaging of lipid fragments in biological samples (Ostrowski et al. 2004; Piwowar et al. 2013).

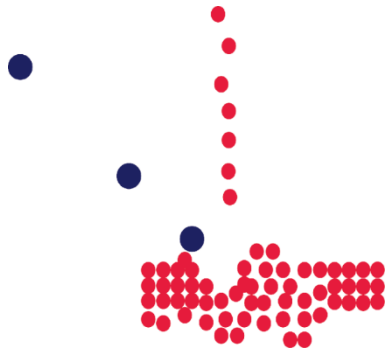

Figure 15. Secondary Ion Mass Spectrometry with C_{60} primary ion beam. Focused C_{60} ion beam is used to raster the sample surface. Less fragmentation and higher sputter yield are obtained with C_{60} primary ion beam compared with atomic primary ion beam.

One example of C_{60} imaging of single cell lipids is demonstrated by Passarelli et al. (Passarelli, Ewing, and Winograd 2013) (Figure 16). Intact ions of vitamin E and

cholesterol were observed. Fragment ion peaks of phosphocholine were used to demonstrate its distribution. The author stated that the parent ions of phosphocholine were not enough to allow imaging. The phosphocholine headgroup (m/z 184) appears to be the most intense peak for phosphocholine; however this species is not specific for a single lipid.

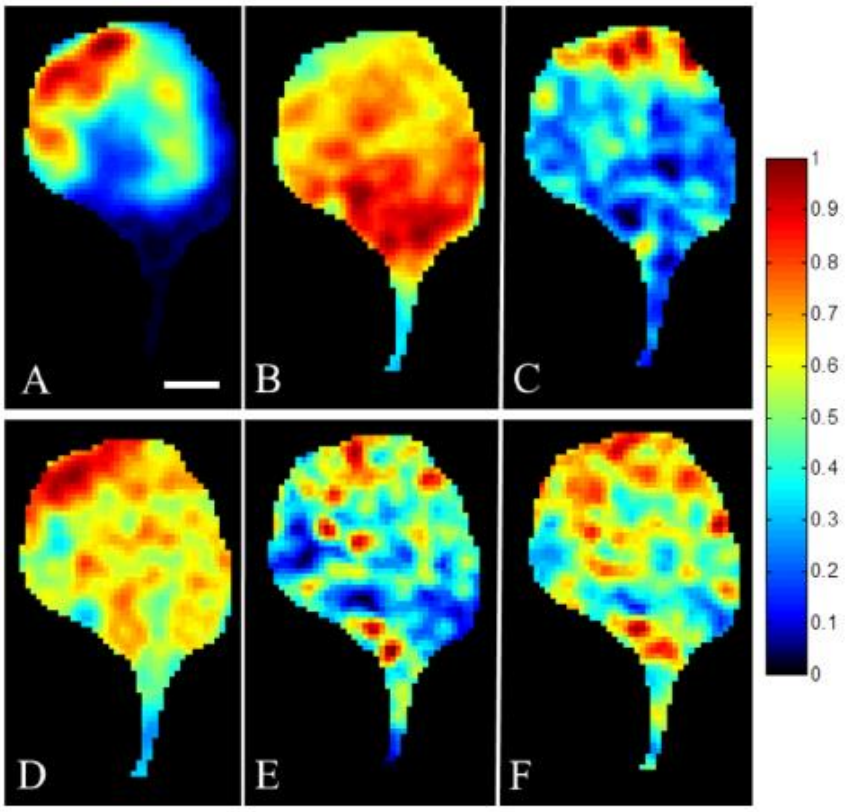

Figure 16. C_{60} TOF-SIMS imaging of a single aplysia neuron. Ion images of (a): vitamin E (m/z 430.3); (b): hydrocarbon (m/z 128.1); (c): cholesterol (m/z 369.3); (d): phosphocholine headgroup (m/z 184); (e): PC (15:0 e/18: 1) fragment (m/z 709.6); (f): sum of PC related fragment peaks. Scale bar is 100 μm. Reprinted with permission from Passarelli, Ewing, and Winograd (2013), Copyright 2013 American Chemical Society.

1.2.5 Microscope Ion Imaging

Based on the way an image is formed, IMS can be divided into microprobe and microscope ion imaging (Luxembourg et al. 2004) (Figure 17). In microprobe imaging, the primary ion beam is focused and scans the sample surface pixel by pixel. The imaging resolution is determined by the size of the focused primary ion beam. In microscope ion imaging, the secondary ions coming out of the sample surface store their relative position information in the transmission process and are projected back to a mass-resolved image of the sample on a position sensitive detector. In this case, the secondary ion optics determine the imaging resolution. The majority of the IMS methods used today belong to the microprobe ion imaging which has achieved high spatial resolution below micrometer which has not demonstrated high spatial resolution for intact molecular species. In addition, the imaging time is long (hours or even days) because the primary ion beam is rastered on the sample surface pixel by pixel.

The spatial resolution of microscope ion imaging is limited by spherical and chromatic aberrations as in the optical microscope. If sufficient intensity is available in a molecular ion signal, a small contrast aperture can limit the spherical aberrations allowing sub-micron spatial resolution. For weaker signals, a larger contrast aperture must be used which results in resolution of a few micrometers or tens of micrometers. Few micrometer resolution is sufficient for sub-cellular imaging of most eukaryotic animal cells. Microscope ion imaging provides an option for primary ion beams which are difficult to focus. The image acquisition time can be decreased significantly because the primary ion beam no longer needs to raster the sample surface.

Microprobe ion imaging has been highly developed. In addition to pulsed lasers, various primary particle beams have been developed including: atomic ion beam (Cs^+, O^-, Ga^+), small cluster ion beam (SF_5^+, C_{60}^+, Bi_3^+, Au_3^+), heavy cluster ion beam (Ar_n^+, $(H_2O)_n^+$), massive cluster ion beam and neutral cluster beam (SO_2, H_2O). The major current methods have already been discussed above.

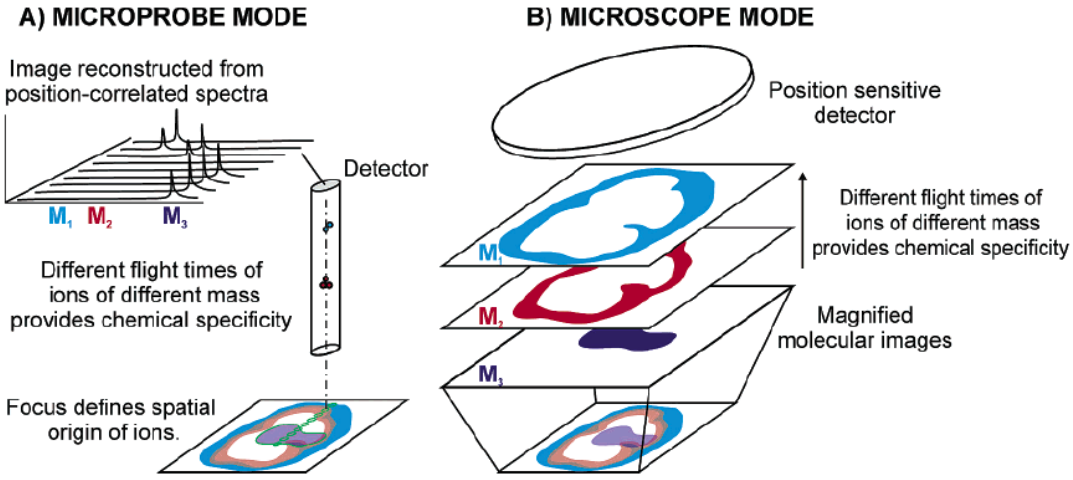

Figure 17. (left): microprobe ion imaging, the primary ion beam scans sample surface pixel by pixel; (right): microscope ion imaging, magnified ion images are projected onto a position sensitive detector. Reprinted with permission from Luxembourg et al. (2004), Copyright 2004American Chemical Society.

Current commercially available microscope ion imaging mass spectrometers include TRIFT from Physical Electronics Inc (USA) and Cameca xf instruments from Cameca Inc (France).

TRIFT instruments have been developed by Physical Electronics Inc (USA). The microscope imaging capability was incorporated into a time of flight mass spectrometer. It can do microscope imaging for heavy m/z ions (>1000 Da, e.g. biomolecular ions). Heeren and colleagues have coupled MALDI and C_{60} primary source with TRIFT II to do microscope ion imaging. In Figure 18, a patterned MALDI sample (a grid on top of a MALDI sample) was used to test the spatial resolution of the microscope ion imaging for the MALDI-TRIFT. The laser spot diameter used is 200 μm. But a spatial resolution of ~4 μm was determined from the test results.

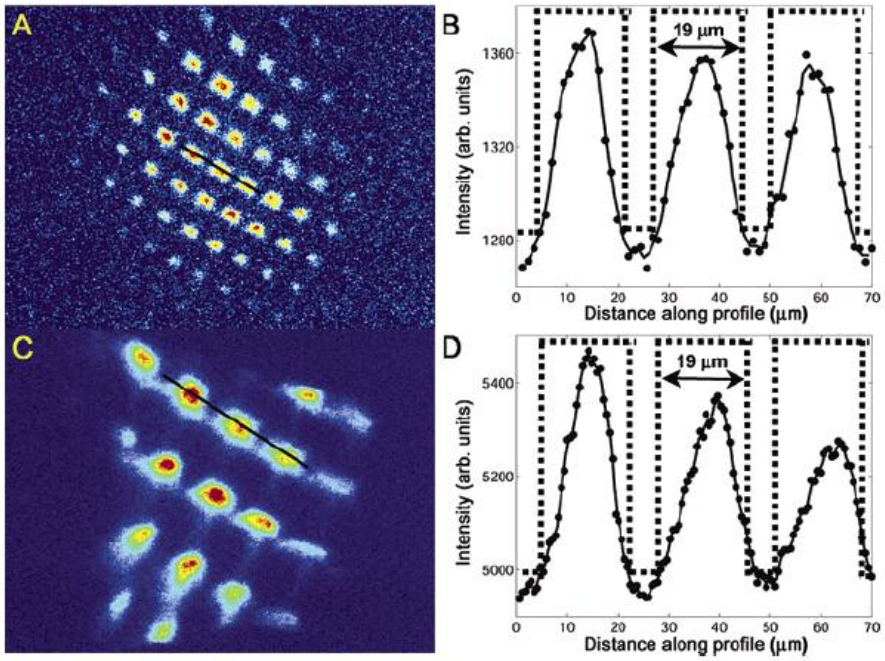

Figure 18. A fine grid was gently pressed onto a MALDI sample (insulin and substance P in DHB matrix). (a): 20 laser shots matrix ion image; (b): plot profile for the line scan in (a); (c): 80 laser shots total ion image with a higher amplification; (d): plot profile for the line scan in the (c). A spatial resolution of ~4 μs was determined. Reprinted with permission from Luxembourg et al. (2004), Copyright 2004American Chemical Society.

A direct comparison between microprobe and microscope ion imaging with MALDI-TRIFT has been performed by the Heeren group (Klerk et al. 2009). A 200 μm laser beam was used to raster over the sample surface for microprobe imaging. An improvement in spatial resolution can be observed for microscope imaging compared with microprobe imaging (Figure 19).

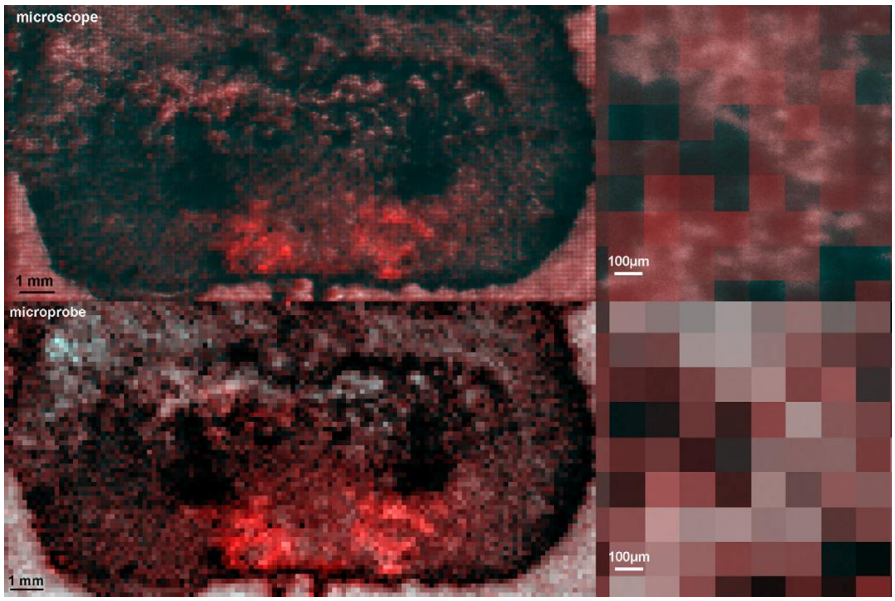

Figure 19. A comparison of microscope and microprobe ion imaging with MALDI-TRIFT on a transverse rat brain section. (Top): microscope total ion image; (Bottom): microprobe total ion image. A full resolution ion image for each was displayed at the right side. The laser diameter was ~200 μm. Microscope ion image has a higher spatial resolution compared with the microprobe ion image. Reprinted with permission from Klerk et al. (2009), Copyright 2009 Elsevier B.V.

Another category of microscope ion imaging is found in Cameca xf instruments (e.g. Cameca 3F IMS). This instrument uses a magnetic sector mass spectrometer. Due to

the limited mass range from the magnetic sector, this instrument is mainly used with elemental analysis.

Chandra el al. have used the Cameca IMS 3F to image the distribution of boron inside tissue samples (Chandra et al. 2013) (Figure 20). In Boron Neutron Capture Therapy, the targeted localization of ^{10}B into the cancer cells is important. 1-amino-3-borono-cyclopentanecarboxylic acid (cis-ABCPC) was fed to the B16 melanoma mouse. A subsequent microscope ion image of ^{11}B revealed uneven distribution inside the tissue sample. It is more concentrated inside the nucleus of some cells.

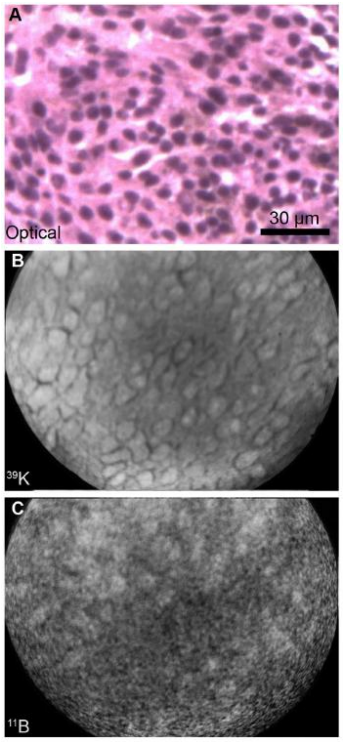

Figure 20. (a): Optical image of the H&E stained B16 mouse melanoma; (b): microscope ion image of ^{39}K revealing the cell morphology; (c): microscope ion image of ^{11}B revealing targeted distribution inside some cells (Chandra et al. 2013).

Another example was to image Gd distribution after using the Gd-based magnetic resonance imaging contrast agents (GBMCA). This agent can be toxic, or even can result in death for patients due to renal failure. It is related with a disease, Nephrogenic Systemic Fibrosis (NSF). Here Abraham et al. used Cameca 3F IMS to do microscope ion imaging of Gadolinium from NSF patient skin samples (Abraham et al. 2008) (Figure 21).

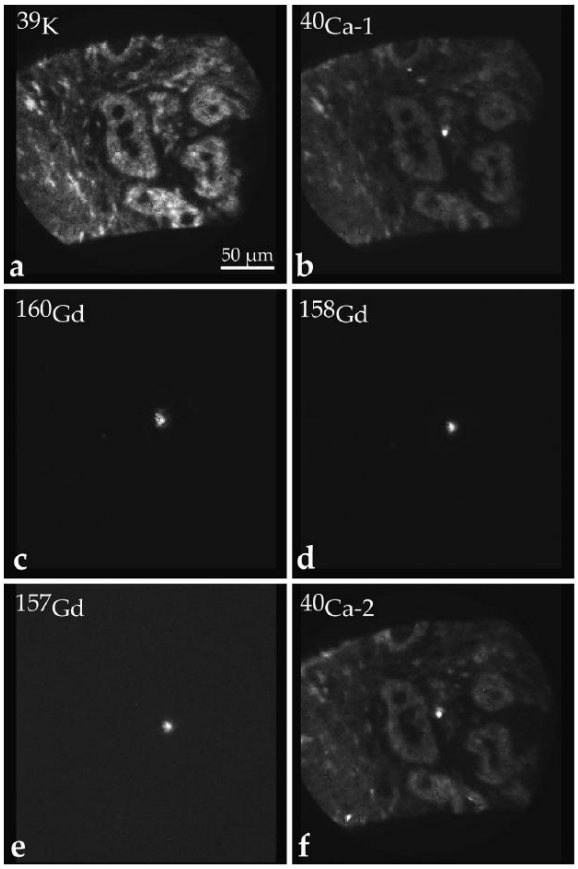

Figure 21. Microscope ion image of ^{39}K, ^{40}Ca, ^{160}Gd, ^{158}Gd and ^{157}Gd in a NSF (Nephrogenic Systemic Fibrosis) patient skin sample. The results revealed a concentrated and co-localized Gadolinium with Calcium. Reprinted with permission from Abraham et al. (2008), Copyright 2008 Elsevier B.V.

1.2.6 Summary of the Current IMS Methods

For the current imaging mass spectrometry methods, each one has its own advantages and disadvantages.

Secondary ion mass spectrometry with atomic ion beam or C_{60} ion beam can achieve high spatial resolution. But they deposit a high energy density into the sample which results in extensive fragmentation. This is not suitable for intact biomolecular ion imaging.

MALDI has a broad intact mass range. In microprobe ion imaging, the spatial resolution is limited by the laser size and ultimately by the matrix smearing. The commonly used laser diameter size is ~100 μm. The laser diameter can be smaller, but the expense is the acquisition time. MALDI can be coupled with a microscope ion imaging mass spectrometer which in principle can achieve few micrometer resolution. However, the matrix smear effect introduces an aberration which limits the spatial resolution to be ~10 μm. Also the matrix application complicates the sample processing and data interpretation.

For DESI, since it is operated in atmosphere, it can only do microprobe ion imaging. The spatial resolution is typically limited to ~ 200 μm. Attempts have been made to shrink the electrospray ion beam in order to improve the resolution to ~10 μm. But the acquisition time will be prolonged in proportion to the square of the beam size.

A summary of the key parameters for different imaging mass spectrometry techniques is presented below (Table 1).

Table 1. Summary of the spatial resolution, intact mass range and matrix requirement for different imaging mass spectrometry techniques.

	Spatial Resolution	Intact Mass Range	Matrix Requirement
SIMS with atomic primary ion beam	~50 nm	Mainly atomic secondary ions	No
SIMS with C_{60} primary ion beam	~250 nm	~a few hundred Da	No
MALDI	~10 μm	~10^6 Da	Yes
DESI	~200 μm	~66 kDa	No

1.3 Dissertation Objective

In Figures 4, 5 and 10, the expression of lipids was shown to be changed between cancer tissues and normal tissues. For early diagnostic use one would like to have lipid images with single cell resolution. Most eukaryotic animal cells are ~10-30 μm in size . SIMS with atomic primary ions or C_{60} can achieve sub-micron resolution but does not have sufficient intact mass range for lipid imaging. The spatial resolution of DESI is not enough for sub-cellular imaging. MALDI barely satisfies the purpose, but it requires to use matrix.

The goal of this dissertation project is to develop a new IMS technique called Massive Cluster Impact. Compared with immunohistochemistry or current imaging mass spectrometry methods, the MCI method presented in this thesis can offer multiple

competitive advantages: (1): tag free; (2): full spectrum acquisition (survey of many species at one time) for biomarker discovery; (3): sub-cellular spatial resolution (~3 μm); (4): intact mass range covering lipids, peptides and small proteins; (5): matrix free; (6): high enough useful ion yield for lipids and peptides to produce useful dynamic range (several hundred intact biomolecular ions per 3×3 μm^2 pixel); (7): fast measurement (typically seconds or minutes).

CHAPTER 2

FUNDAMENTALS AND HISTORY OF MASSIVE CLUSTER IMPACT

The massive cluster ion beam originates from electrospray technology. Electrohydrodynamic ionization of a liquid at a capillary surface produces charged droplets which can be used as primary ions to eject secondary ions for mass spectrometry (Mahoney et al. 1991). The extremely low energy density and large total energy deposited make it an ideal cluster source for desorption and ionization of intact molecules. This process is called as Massive Cluster Impact (MCI).

2.1 Production of Massive Cluster Ions

Electrospray technology typically includes three key elements: a capillary, conductive liquid and an extraction electrode. The capillary is filled with a conductive solution (salt is added to an organic solvent to improve its conductivity). An extraction electrode with a different potential from the capillary applies an electric field on the surface of the liquid at the capillary tip. The capillary tip surface has the strongest electric field due to its curvature. The liquid surface is polarized by the electric field. When the electric field is strong enough, it can overcome the surface tension of the liquid. The liquid surface breaks down and emits charged droplets. The charged droplets are accelerated by the electric field to a velocity of several km/s and impact the sample. The charged droplet emission process can be summarized as liquid accumulation at the capillary surface, Taylor cone formation due to the electric field and ejection of a charged droplet jet (Marginean et al. 2004). Large, highly-charged droplets can be produced and

accelerated by the electric field. This droplet beam is called a massive cluster ion beam since the cluster size is much bigger than other cluster ion beams being used (e.g. C_{60}, argon cluster). Glycerol is used in the present work for an electrospray solvent since it has a low vapor pressure which is compatible with vacuum operation. Its surface tension (64 mN/m at 20 ^{o}C) is high compared with other common organic solvents (formamide, ethylene glycol). Ammonium acetate was dissolved into the glycerol to increase its conductivity. A voltage of -10 kV is applied to the solution in the capillary. Together with the ground potential at the extraction electrode, the electrospray process can be initiated.

There are also groups around the world doing electrospray impact using water or ionic liquids. Hiraoka and colleagues electrospray water in the atmosphere (Ninomiya et al. 2013; Hiraoka et al. 2006; Asakawa and Hiraoka 2011; Asakawa et al. 2007). The water droplets are introduced into vacuum through a nozzle. A quadrupole ion guide is used to select the specific water cluster ions to go to the sample. Intact desorption and ionization was demonstrated for small protein samples(Hiraoka, Mori, and Asakawa 2006). Fujiwara and colleagues have developed an ionic liquid electrospray in vacuum(Fujiwara et al. 2011, 2010).

2.2 Characteristics of Massive Cluster Ions

Stimpson et al showed plots of the cluster ion current decay when a continuous glycerol (with NaI) massive cluster ion beam was abruptly switched off(Stimpson and Evans 1978) (Figure 22).

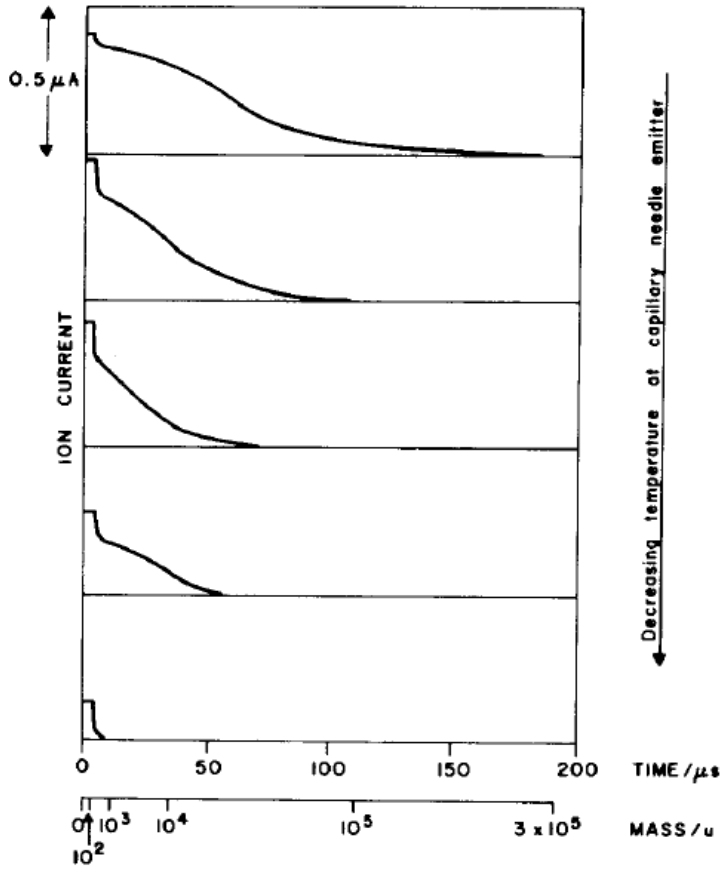

Figure 22. Decay of the cluster ion beam current when a continuous beam was stopped for field free time of flight mass/charge analysis. Higher flight time corresponds to higher mass to charge ratio. The initial signal drop corresponded to the glycerol molecular ion emission. Decay patterns changed from 25 ^{o}C to -30 ^{o}C. Reprinted with permission from Stimpson et al. (1978), Copyright 1978 Elsevier B.V.

The plot of the cluster ion beam current decay at 25 ^{o}C was differentiated to generate another plot below (Figure 23) showing the composition of this glycerol massive cluster ion beam.

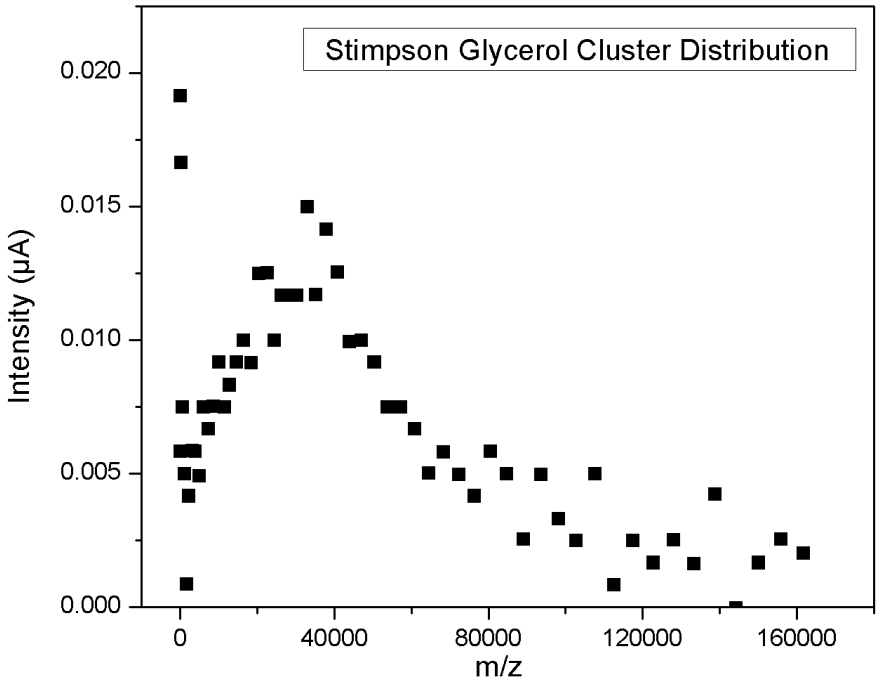

Figure 23: Glycerol cluster ions m/z distribution calculated from Stimpson and Evans (Stimpson and Evans 1978). Initial high intensity component for m/z ~100 corresponded to glycerol molecular ions. Highest cluster ion beam component was found at ~m/z 33,000.

In Figure 23, the initial high intensity ions correspond to glycerol molecular ions. These had ~100 eV/nucleon and a velocity of 150 km/s.

The most abundant heavy cluster ions were located at m/z ~33,000. Based on the Rayleigh limit at which an equilibrium is achieved between the surface tension and the charge repulsion at the droplet surface, the size and charge number can be calculated for this cluster ion (http://phd.marginean.net/rayleigh.html, surface tension: 0.064 N/m, molecular mass 92 au, density: 1261 kg/m^3). It had 5×10^4 glycerol molecules, a mass of

~5 MDa, carried ~140 charges, ~0.3 eV/nucleon energy density, 11 nm radius and impacted the target with a velocity of ~8 km/s.

There was a long tail of heavy cluster ions located above m/z 80,000. Cluster ions with m/z 80,000 had a radius of ~20 nm, 5 km/s velocity and carried ~350 charges with 0.1 eV/nucleon. The intensity of cluster ions over m/z 80,000was relatively small compared with m/z at 33,000.

Cluster ions with different energy density and velocity will have different effects on fragmentation. With the same acceleration voltage, lower m/z ions have higher energy density and can create more surface and in-depth fragmentation in the sample. The light component of the beam in Figure 7 constituted 10% of the beam current. It should be noted that this light component is mainly single charged glycerol molecular ions. The most probable cluster ions carried ~100 charges. This means that ~90% of the total particle flux is low m/z ions. This m/z region is not good for intact sputtering and ionization of molecular ions.

As the temperature was reduced, Stimpson et al. showed that the percentage of low m/z ions increased. At -30 ^{o}C, majority of the ions were the low m/z ions. The way temperature affected the cluster ion beam distribution was through increasing viscosity, which reduced the flow rate. When the flow rate was extremely low, the electrospray process generated mostly molecular ion emission. In the present application of soft sputtering and ionization, the heavier cluster ions are preferred, thus higher temperature and faster flow rate are preferable.

The highest intensity of massive cluster ions in Figure 7 locates ~ m/z 33,000. A comparison of the energy density between the m/z 33000 glycerol massive cluster ion, the oxygen primary atomic ion bean and C60 ion beam is given below in Table 2.

Table 2. Comparison of energy density among oxygen ion beam, C60 ion beam and glycerol ion with m/z 33000 accelerated under the same voltage of -10 kV.

Primary Ion Species	O^-	C60	Glycerol (m/z 33000) Cluster
Energy density (eV/nucleon)	~600	~10	~0.3

The energy density in a glycerol cluster ion (m/z 33,000) is 2000 times smaller compared with the oxygen atomic ion beam. The extremely low energy density facilitates the intact sputtering of ionized sample molecules.

Another advantage of the massive cluster ions produced by the electrospray process is the huge number of charges carried by one droplet. The m/z 33,000 glycerol cluster ion carries ~140 charges. Under the same electric field, it carries a total energy (~1.4 MeV for 10 kV acceleration) 140 times bigger than a single charged primary ion. The bigger total energy deposited improves the sputter yield and produces shock wave heating at the sample.

It should be noted that the glycerol cluster ion distribution in our system might be different than Simpson's since a different diameter capillary (100 μm instead of 200 μm) and different solute (ammonium acetate instead of NaI) were used. But the general phenomenon should be similar: a light ion component composed of singly-charged glycerol molecule and a broad distribution of massive cluster ions.

2.3 Impact of Massive Cluster Ions

When the impact velocity of glycerol cluster ions is greater than the sound velocity in the matrix, the deposited energy cannot dissipate fast enough. The volume of the cluster ions and a similar volume of the sample material are compressed giving rise to shock heating. A temperature of ~ 1000 K and a pressure of ~30 GPa can be achieved in the shock wave heating for 6 km/s impact velocity(Mahoney et al. 1992). The immediate heating of the sample materials results in a micro-explosion that ejects ionized sample molecules out of the sample surface. The explosion process results in an expanding plume that may have a cooling effect preventing sample molecules from fragmentation.

Dr. Leonid Zhigilei at University of Virginia did a simulation of a water cluster ion impacting a rigid target (Zhigilei 2001). A water droplet with 3×10^5 water molecules impacted the target at 2 km/s. Snapshots from the simulation process are shown below in Figure 24. The water droplet exploded after the impact.

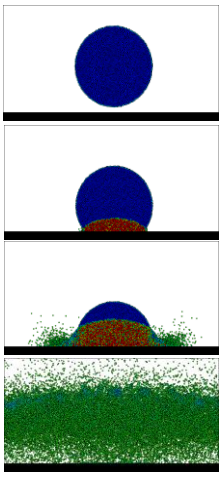

Figure 24: Snapshots from MD simulations of water cluster impact. Impact velocity was 2 km/s. The red color represents water molecules at higher temperature due to shock heating. After the impact, all the water molecules were vaporized.

When the sample is not a rigid target, not only the cluster ion is compressed and explodes, a similar volume to the cluster ion of the sample materials underneath also undergoes the compression and explosion process. A cartoon picture is shown below (Figure 25) about this process.

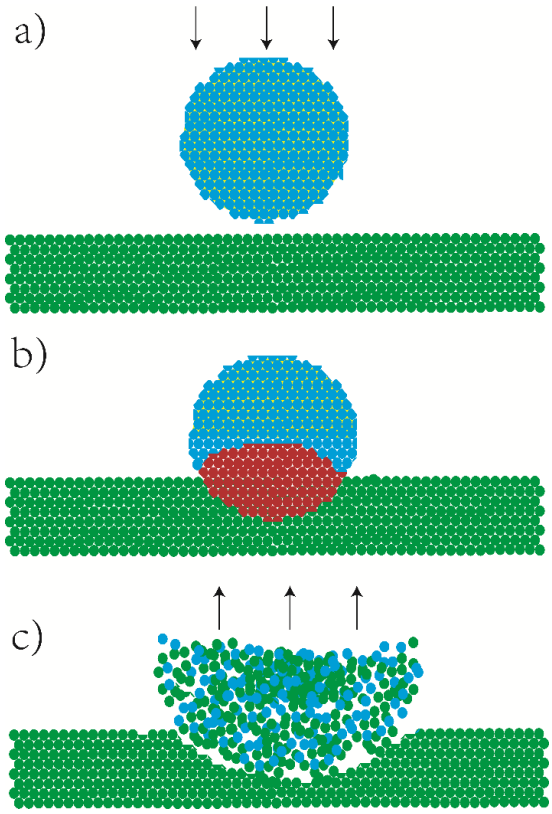

Figure 25. Cartoon images of a glycerol cluster ion impacting on a soft sample. The blue color represents the glycerol cluster ion. The green color represents the sample molecules. The red color represents the molecules at high temperature in the shock wave heating process. The glycerol droplet together with a similar volume of sample material is sputtered into the gas phase.

2.4 History of Massive Cluster Impact

The idea of MCI was first brought forward by Dr. Williams and John Mahoney in a 1983 NSF proposal. Intact desorption and ionization was first demonstrated by Mahoney et al. (1991) from a sample dissolved in glycerol. Fabris et al. (1995) showed intact multiple charged peaks of bovine carbonic anhydrase II (29kDa) in thioglycerol solution. The first matrix-free detection of insulin and cytochrome c was reported by Cornett et al. (1994) (Figure 26). The ability of MCI to generate intact biomolecular ions from neat samples suggested that MCI might be a useful alternative to MALDI for imaging at length scales smaller than the MALDI matrix limit of ~10-20 μm and so inspired the work described in this thesis.

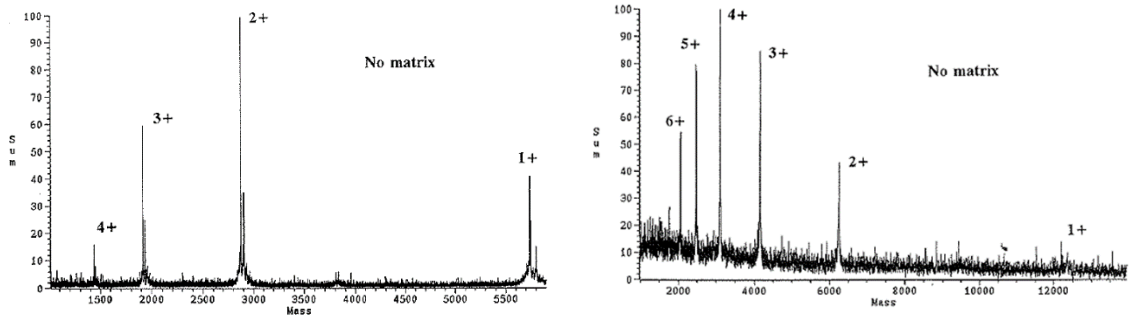

Figure 26: Single charged and multiple charged insulin peaks (left) and cytochrome c peaks (right) without matrix was first reported by Cornett et al.(Cornett, Lee, and Mahoney 1994) with glycerol cluster ions impact. Reprinted with permission from Cornett et al. (1994), Copyright 1994 John Wiley & Sons, Ltd.

CHAPTER 3

INSTRUMENTATION OF MCI-TRIFT

Massive cluster impact produced from the electrospray process gives us a new way of sputtering and ionizing sample molecules with extremely low energy density. The question remaining is what kind of mass spectrometer to use and how to do imaging. The massive cluster ion beam is a diverging beam due to the curved electric field at the capillary surface. It also has a broad m/z distribution and therefore a broad velocity distribution. These two problems make the beam difficult to focus or pulse. So microprobe ion imaging with a pulsed beam is not a feasible approach here. The option left is microscope ion imaging. In the work described here, an ion microscope imaging mass spectrometer, Triple Focusing Time of Flight Mass Spectrometer (TRIFT-I) from Physical Electronics Inc, is used. Because the cluster beam could not be pulsed with good time resolution, the secondary ion beam was pulsed for time-of-flight operation.

3.1 MCI Source Setup

As discussed in Chapter 2, in order to start the electrospray process, a conductive liquid, a capillary and an electric field strong enough to start the electrospray are needed. The MCI source was built on a Delrin flange (Figure 27) installed on the TRIFT mass spectrometer at an angle of 45^{o} with respect to the sample surface. This position originally was designed for a Cesium ion source. A Delrin flange was used to insulate the capillary from ground. When the source is not running, the glycerol solution can flow along the capillary to the flange possibly making a short circuit if the flange was made of

metal. A Delrin reservoir was filled with a conductive liquid which is the 1.5 M ammonium acetate in glycerol solution. The schematic of the Delrin reservoir design is attached in Appendix A (Figure A.1.). A voltage of -10 kV was fed into the solution in the reservoir. A vacuum/pressure pump (Thermo Scientific, Model No.420-1901) was used to adjust the flow rate. Normally atmospheric pressure was sufficient to drive the glycerol flow; occasionally it might be necessary to pressurize the reservoir for several seconds to start the flow. A 22 cm length of PEEK tubing (part number 1546, Upchurch Scientific, USA) was used to conduct liquid from the reservoir to a valve. The valve (part number P-732, Upchurch Scientific, USA) was used to manually turn on or turn off the solution flow in the capillary. The voltage of the source must be turned off before operating the valve. The other side of the valve was connected with a fused silica capillary (100 μm ID and 360 μm OD) (part number 1932, Upchurch Scientific, USA). The length of this fused silica capillary was 6 cm. The capillary length inside the vacuum was 8 mm. The capillary was cut using a carbide tubing cutter. The surface was polished with sand paper (1000 grit) (Figure 27c). The capillary was inserted through a tiny hole on to the Delrin flange. The connection of the capillary to the flange was done by using an Adapt Assy F-200 ×¼-28 male (part number: P-640, Upchurch Scientific, USA). The sealing of the connector to the flange was done by screwing the connector tightly on the Delrin flange (press the end tightly onto the surface of the Delrin). The flange schematic is in Appendix A (Figure A.2.). An extraction electrode (4 mm thickness, 22 mm OD, 6 mm ID) at ground potential was placed 20 mm away from the capillary surface. The schematic of the extraction electrode is in Appendix A (Figure A.3.). Optical images of

the MCI setup are shown in Figure 28. The reservoir, the pump, the tubing and the valve were sheltered by a plastic box (LEXAN Sheet, poly, clear) and a Delrin substrate.

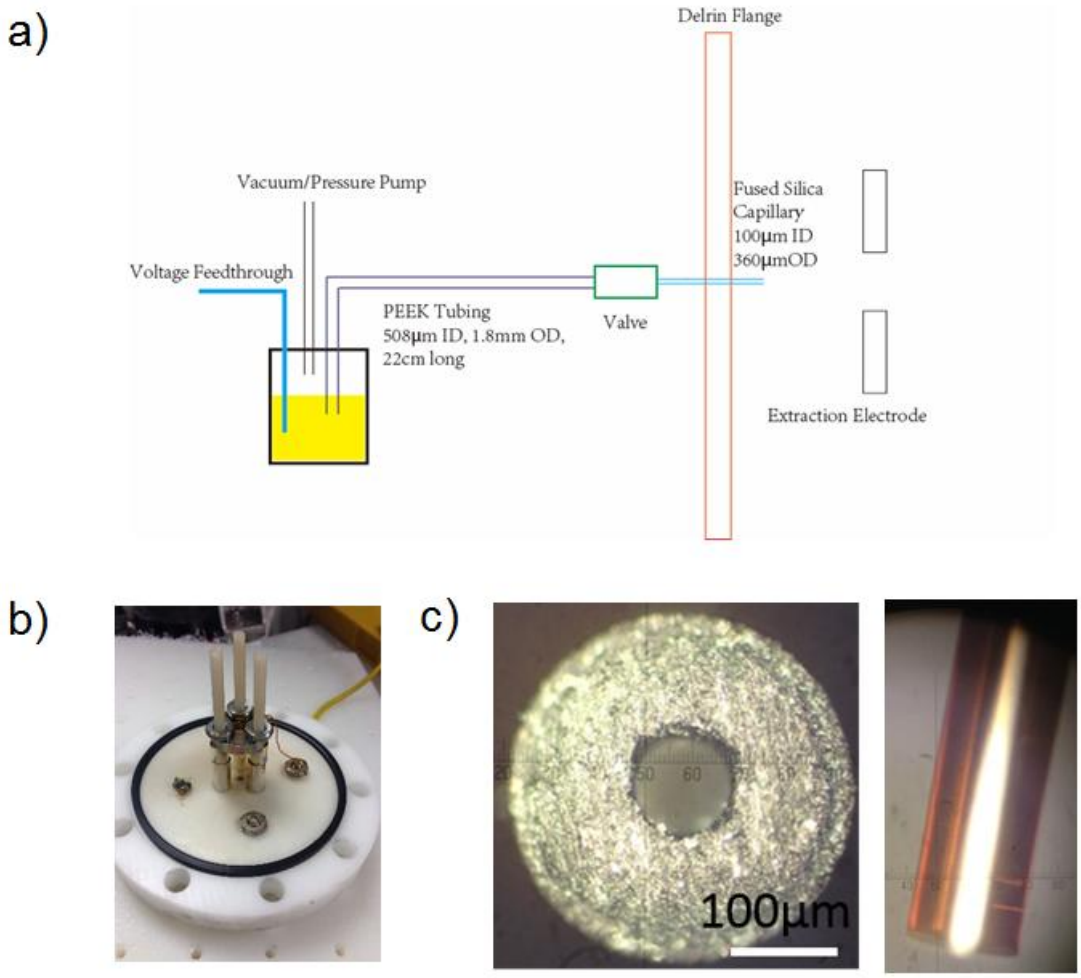

Figure 27. a): MCI source design: the voltage of -10 kV was applied to the solution in the reservoir, a vacuum/pressure pump was used to adjust the flow rate, a valve was used to turn on/off the source, the distance of capillary inside the vacuum was 8 mm. b): Images for the assembly of the MCI source setup. c): Optical images for the front view (left) and side view (right) of fused silica capillary used in the MCI source. The capillary had a 100 µm ID and 360 µm OD.

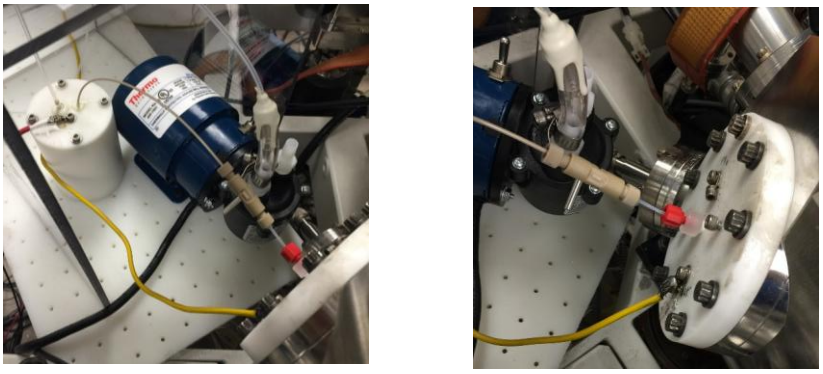

Figure 28. Images of the MCI source setup. The Delrin reservoir was filled with 1.5 M ammonium acetate in glycerol solution. A valve was used to turn on and turn off the solution flow inside the capillary.

The voltage difference between the capillary and the extraction electrode generates an electric field to start the electrospray process. The emitted charged glycerol droplets were accelerated by the electric field through the aperture of the extraction electrode. The charged droplets flew through a 3 mm×1 mm entrance slit to the sample. The sample was held at +3055 V. The potential difference between the capillary and the sample was 13 kV. A SIMION simulation is shown here (Figure 29) for the MCI source.

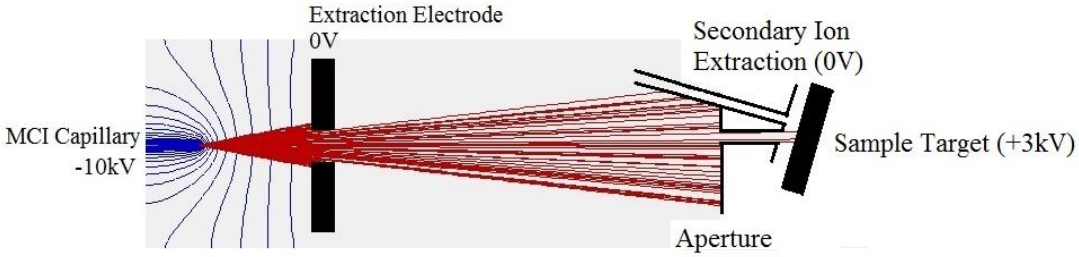

Figure 29: SIMION (an ion optics simulation program) simulation of electrospray process. The charged droplets are accelerated and fly through the aperture of extraction electrode and the entrance aperture to the sample.

The curved electric field at the capillary surface makes a diverging cluster ion beam. Together with the broad distribution of m/z ions, it is difficult to pulse or focus this primary cluster ion beam. Here we use an ion microscope imaging mass spectrometer called TRIFT to solve this problem.

3.2 MCI-TRIFT Instrumentation

The Triple Focusing Time of Flight mass spectrometer (TRIFT-I) was invented by Bruno W. Schueler in the early 1990s (Schueler 1990; Schueler 1992). It is a time of flight ion microscope imaging mass spectrometer. The bombardment by the primary ion beam ejects secondary ions out of the sample surface that are extracted and accelerated by the extraction electric field (3055 V) into a field-free region. Different m/z ions have different velocities, thus different flight times arriving at the detector. The m/z can be calculated through the flight time. Stigmatic ion optics ensured that ions leaving the sample surface stored their relative position information in the transmission process and were projected onto an image at a position sensitive detector (dual microchannel plates). Two Einzel lenses (lenses I and II) in the secondary column together with the stigmatic imaging properties of the three ESAs (spherical electrostatic sectors), produced a 60× magnified image of a sample area about ~350 μm in diameter at the dual microchannel plates and a phosphor screen.

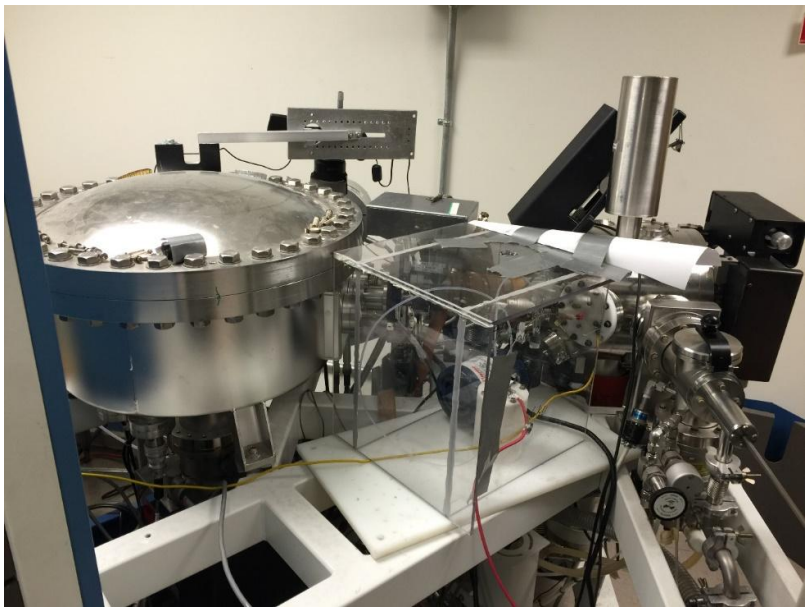

Figure 30. The MCI source was installed on to the TRIFT instrument and fixed on a Delrin plate. The whole source was protected inside a plastic box.

The reservoir in the MCI source was under atmospheric pressure. Negative potential on the capillary helped avoiding arcing between the capillary and the extraction electrode. Electron bombardment with a positively charged capillary was found to degrade the capillary tip within several hours of operation. Also the negative potential together with the positive potential at the sample gave increased impact energy. It was discovered by Williams and Aksyonov (Aksyonov and Williams 2001) and later confirmed by Hiraoka et al. (Asakawa and Hiraoka 2011) that the polarity of the impacting massive cluster ions does not influence ion formation efficiency.

Because it is difficult to pulse the heterogeneous cluster ion beam, the primary ion beam was run continuously and the secondary ion beam was pulsed for time-of-flight mass analysis (Figure 31). For this, blanker plates were used. Two parallel metal plates,

with one plate at ground potential and the other plate at 200 V, can deflect the secondary ion beam off the central axis. The voltage on the blanker plate can be turned on and off with a pulse generator and a blanker box. The continuous secondary ion beam extracted from the bombarded sample surface was chopped by dropping the voltage across the blanker plates (blanker I), normally held at 200 V, to zero. The pulse width, and hence mass resolution, is adjustable, with a minimum nominal pulse width of 200 ns, but must be chosen to be larger than the transmission time of the secondary ions of interest through the blanker I region (length ~5 cm) (Zhang, Franzreb, and Williams 2014). Effective pulse width is the applied pulse width minus the ion transmission time and so varies for different m/z values in a mass spectrum. Typical pulse widths applied at blanker I ranged from several μs to tens of μs. The resulting secondary ion pulse traveled through a series of three spherical electrostatic sectors (ESA) which functioned as stigmatic imaging lenses while also providing time-focusing for ions of different initial energies. The time focus plane was exactly coincident with the image focal plane at the first microchannel plate of the detector array.

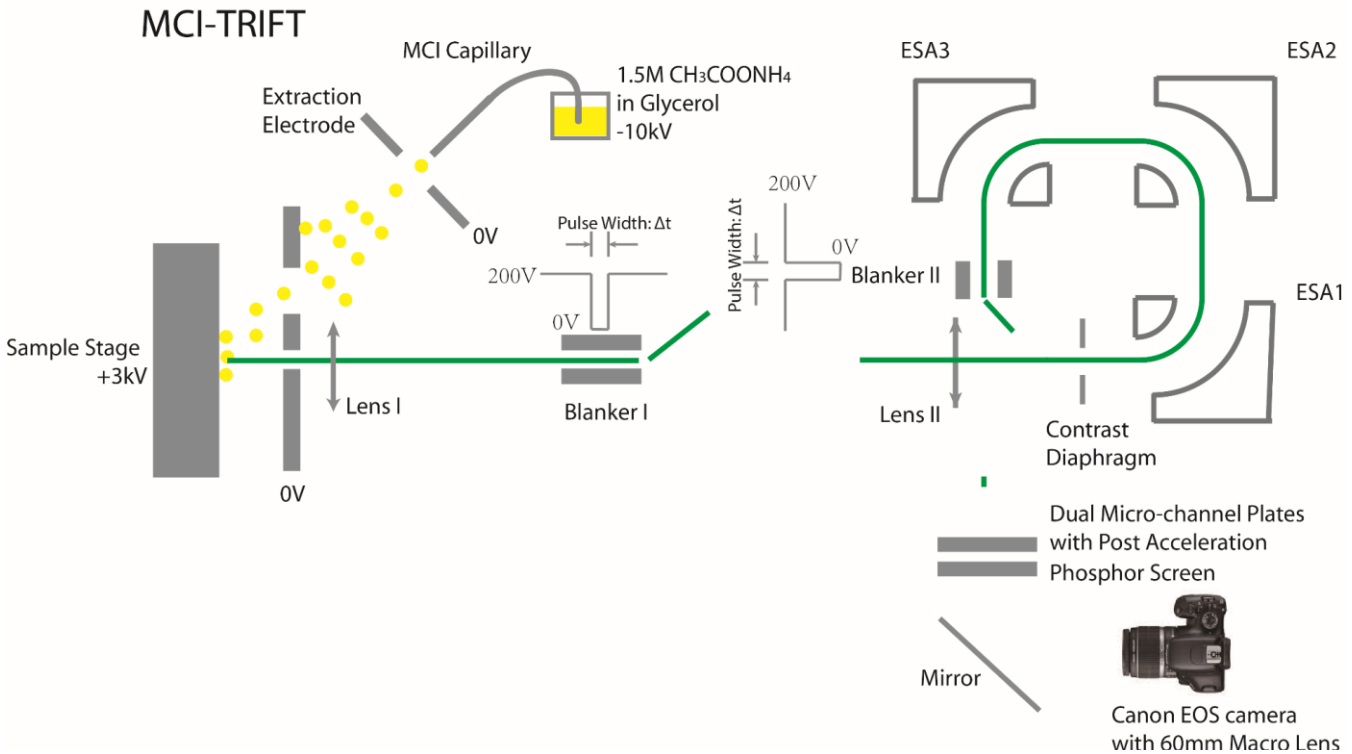

Figure 31. Scheme of the experimental setup (MCI-TRIFT). A reservoir filled with 1.5M CH_3COONH_4 solution. -10 kV applied to the reservoir. A fused silica capillary with 100µm ID and 360µm OD conducted the solution from reservoir to vacuum. Sample voltage +3055 V, post-acceleration -9 kV. The vacuum in the sample chamber was about 5 x 10^{-6} torr with the MCI source in operation. Blanker I and II were used for secondary ion pulsing and selection for imaging respectively. A Canon EOS camera with 60 mm macro lens was used to image the back of the phosphor screen. Reprinted with permission from Zhang et al. (2014), Copyright 2014 John Wiley & Sons, Ltd

Mass selection of the secondary ion species to be imaged was made using a second pulse at deflector plates at the exit of the electrostatic sectors (blanker II) with an appropriate time delay. Blanker II was usually operated with the same deflection voltage of 200 V and the same pulse width as for blanker I, except for useful ion yield measurements, for which the pulse width for blanker II was chosen to be longer than for blanker I to allow evaluation and subtraction of the ion background underneath the peak of the imaged ion species.

In order to improve detection sensitivity for heavy species, the detector was operated with a post-acceleration voltage of -9 kV which reduced the magnification somewhat. The ion image on the phosphor was recorded by a DSLR camera (Canon EOS) with a 60 mm macro lens (Figure 32). Imaging times were typically a few minutes.

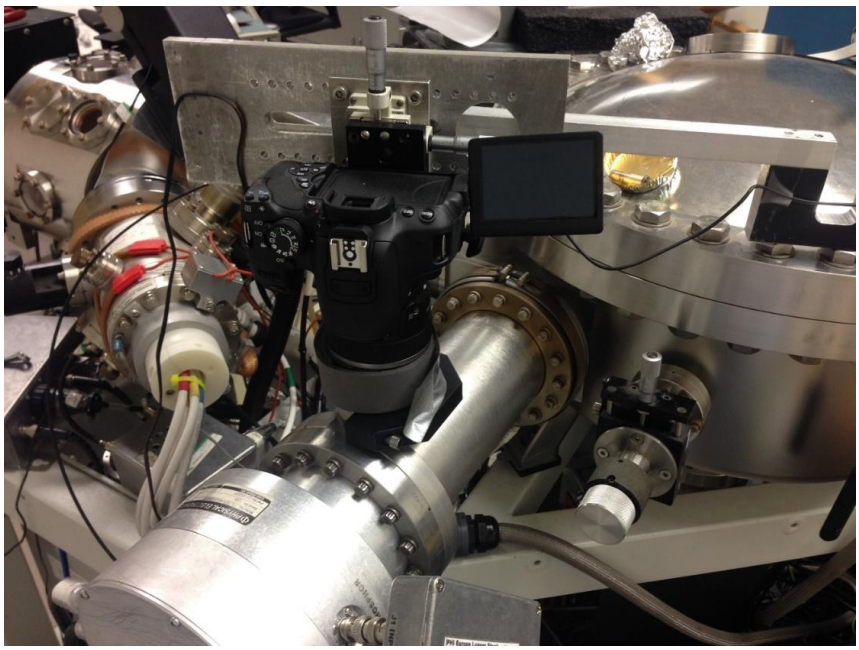

Figure 32. A Canon EOScamera with 60 mm macro lens was installed to look at the back of the phosphor screen. Bulb imaging mode with manually determined exposure time.

Lens I was close to the sample where vacuum quality is poor and for low aberrations was operated as an acceleration-deceleration Einzel lens at a rather high negative voltage (~ -8 kV for positive secondary ions). The poor vacuum during glycerol spraying led to some overloading of the instrument power supply for this lens. A Spellman power supply which can drive high current was used to stabilize the -8kV at Lens I. An effort to achieve microscope-mode ion imaging with lens I instead in deceleration-acceleration mode at a smaller positive voltage was not successful.

A small aperture or contrast diaphragm (CD) was located at a crossover of the secondary ion trajectories in front of the first electrostatic analyzer (ESA1) and was used to limit the angular divergence of ions entering the ESA flight section and so to limit spherical aberration in the ion image. Five different aperture sizes were available on a moveable aperture strip. Smaller apertures improve the image resolution, but at the expense of lower ion transmission. Useful ion yield measurements have been made using the 0.2 mm diameter CD that has been demonstrated to give ~ 3 μm image resolution; in addition measurements have been made using the biggest CD, 2 mm in diameter. The latter measurements reflect UY values that could be achieved if it were possible to focus the massive cluster beam for rastered beam imaging so that the mass spectrometer could be operated at maximum transmission.

For detection of negative secondary ions (sample voltage -3055 V), the MCI emitter voltage was increased to -14 kV. The post acceleration voltage was +6 kV to avoid arcing at the positively biased phosphor screen.

The duty cycle of the time-of-flight measurement is defined as the ratio of the effective pulse width at blanker I (i.e. corrected for the transmission time of the selected ion species through the 5 cm long blanker I) to the chosen maximum flight time (i.e. inverse Blanker I pulse repetition rate). The duty cycle is mass-dependent because transmission times through Blanker I differ with mass, and scales inversely with the mass resolution of the ion species of interest; a typical value of the duty cycle used in these measurements ranged from 0.5% to 4 %. For continuous sputtering, the sampling efficiency is the same as the duty cycle – this is the fraction of the sputtered material that is available for sampling in the experiment.

3.3 Modifications of TRIFT

The major purpose of the modifications was to improve the vacuum inside the mass spectrometer. The MCI source electrosprays glycerol solution into vacuum. It makes the vacuum of the TRIFT poor that it cannot have a stable operation (arcing between the capillary and the extraction electrode, arcing at Lens 1 and high background noise at the detector). Other modifications have been done to provide stronger power supply for stable voltage during measurement, selected ion imaging and detection for heavy secondary ions.

Details of the modifications are summarized:

(1) A liquid nitrogen cold finger was added through a window to the sample chamber. It was close to the MCI source. It can improve the vacuum by ~10 times from 10^{-5} torr to 10^{-6} torr range.

(2) Additional plastic insulation was added to the Lens 1 -8 kV feed-through cable. This reduced the arcing for the feed-through cable to ground.

(3) A Spellman power supply (0-10 kV, 0-20 mA) was used to replace the original instrument power supply to stabilize the -8 kV lens voltage. Small fluctuations of Lens 1 voltage can degrade the image resolution.

(4) Slits were cut into the flight tube near lens I for more efficient differential pumping with the 230 L/s turbo molecular pump attached to the sample chamber.

(5) A small aperture (7 mm in diameter) was inserted before lens II to improve differential pumping in the flight chamber and detector region.

(6) Post acceleration was installed on the front microchannel plate to improve the detection efficiency for the heavy secondary ions. The typical post acceleration voltage used was 9 kV.

(7) A Canon EOS camera with 60 mm macro lens was used in "Bulb" mode to record ion images with a manually controlled exposure time.

With these modifications, stable operations at a pressure ~ 5 x 10^{-6} torr in the sample chamber were achieved with the massive cluster ion source in operation.

3.4 Timing Scheme

Because it is difficult to pulse the primary cluster ion beam with good time resolution, the secondary ion beam has to be pulsed for time of flight mass analysis. A flow chart of the timing scheme for the time of flight mass analyzer and ion selection for imaging is shown in Figure 33.

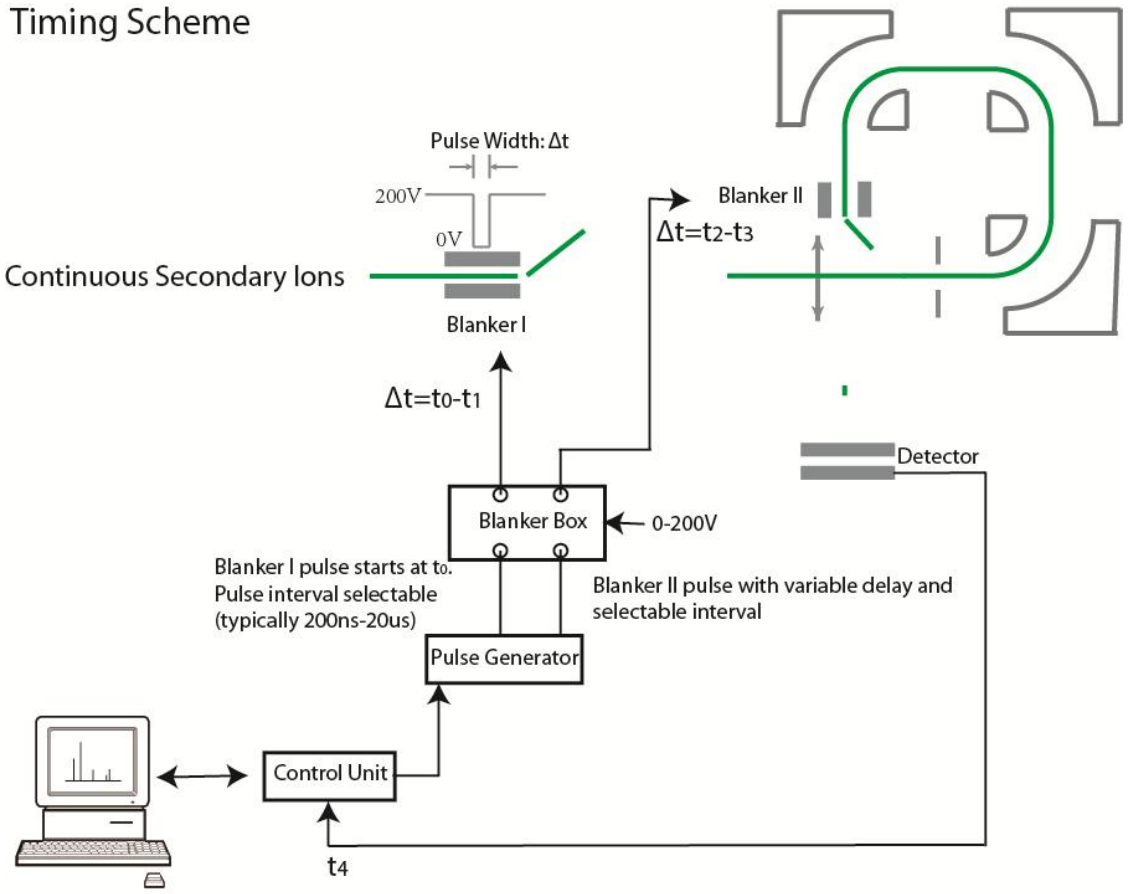

Figure 33. A flow chart showing the signal input and output for secondary ions pulsing for the time of flight mass analysis and selection for imaging. A computer, control unit, pulse generator and blanker box were used to supply a pulsed voltage of 200 V to the blanker I and blanker II. The signal output from the phosphor screen comes back to the computer to produce a spectrum.

The timing system was composed of several elements: a computer, a control unit, a pulse generator (Stanford Research Systems Inc.), a blanker box and the detector. The computer together with the control unit sent a triggering signal to the pulse generator.

The pulse generator can generate two independent pulses with adjustable delay and interval. These two pulses controlled the blanker box to generate two square wave pulses of 200 V to 0 V with selected time windows. The first voltage pulse went to Blanker I to produce the secondary ion pulse. The second voltage pulse went to Blanker II to select the ion window going to the detector with an appropriate delay from Blanker I. When the ions impacted on the detector, a current output from the phosphor screen went back to the control unit and the computer. The detector was operated in a multi-stop mode, i.e. a single ion pulse at the detector produced a one-bit signal in the computer at the corresponding time point. The dead time for one stop is ~100 ps which is enough for our application. With the flight time recorded by the computer, a mass spectrum can be produced. The mass spectrum was calibrated using a high resolution mass spectrum (a small blanker I pulse width was used, e.g. 500 ns) (H^+, Na^+, K^+ peaks were used). The Canon EOS camera was manually determined for exposure time. The ion image from the back of the phosphor screen was recorded.

3.5 Mass Resolving Power (MRP)

Mass resolving power is an important parameter for a mass spectrometer. In a typical time of flight mass analyzer mass spectrometer, the MRP is determined by the total flight time and the effective pulse width of a given m/z ion (Figure 34).

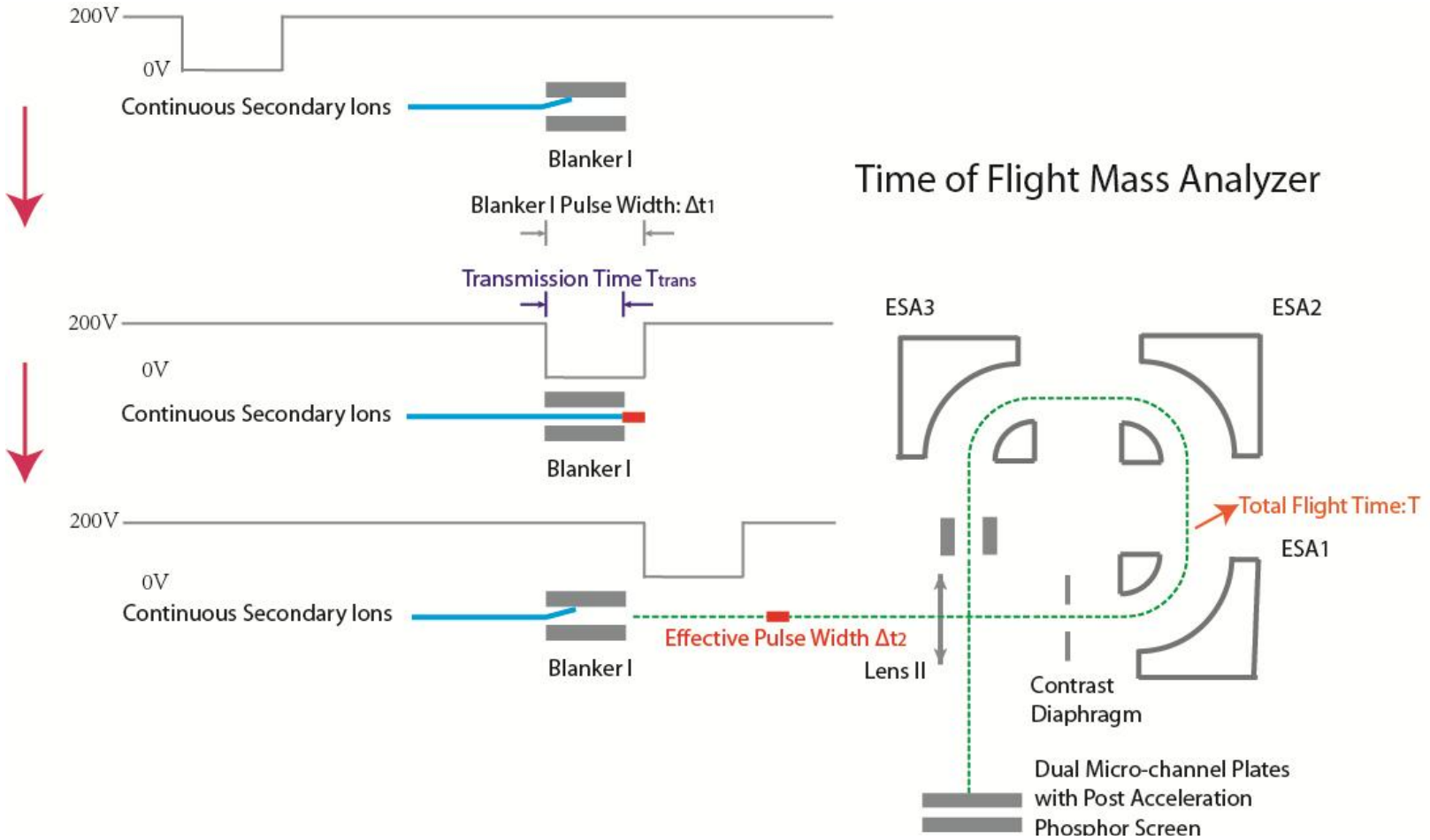

Figure 34. Illustration of the blanker I pulse width (Δt_1), effective pulse width (Δt_2) and total flight time (T, green dash line) of the time of flight mass spectrometer. Effective pulse is equal to the blanker I pulse width minus the transmission time (T_{trans}). The mass resolving power is determined by the effective pulse width and the total flight time.

The flight time for a given m/z ion to fly through a distance can be calculated with Equation 1. It is dependent on the acceleration electric field (V) and the distance (L). The effective pulse width (Δt_2) is equal to the blanker I pulse width (Δt_1) minus the transmission time (t_{trans}) for a specific m/z ion to fly through the blanker I. Mass resolving power is equal to the mass divided by the FWHM (full width at half maximum). It is also equal to the total flight time (T) divided by 2 times the effective pulse width (Δt_2).

Transmission time through Blanker I

$$\mathrm{T_{trans}} = 72.0 \times \mathrm{L\ (m)} \times \sqrt{\frac{\mathrm{m/z}}{\mathrm{V}}} \qquad (1)$$

V: sample potential (+3055 V).

L: length for blanker I (5 cm).

Effective pulse width Δt_2

$$\Delta \mathrm{T_2} = \Delta \mathrm{T_1} - \Delta \mathrm{T_{trans}} \qquad (2)$$

Δt_2: effective pulse width

Δt_1: blanker I pulse width

t_{trans}: flight time through blanker I

Mass resolving power (MRP)

$$\mathrm{MRP} = \frac{\mathrm{m}}{\Delta \mathrm{m}} = \frac{\mathrm{T}}{2\Delta \mathrm{t_2}} \qquad (3)$$

T: total flight time

In reality, the experimental effective pulse width was found to be larger than the theoretical value. Ions near the end of Blanker I when Blanker I was turned to 200 V

could still go through the secondary column and impact the detector. Details will be discussed below in reference to the sphingomyelin spectra in Figs. 35-38.

Several conclusions can be obtained from the above equations: 1) Mass resolution of a given m/z is dependent on a): total flight time; b): blanker I pulse width; c): transmission time; 2) With the same blanker I pulse width, smaller m/z ions have shorter transmission time, longer effective pulse width, higher integrated intensity, broader peak width, lower mass resolution; 3) A given m/z ion cannot pass through blanker I when its transmission time is longer than the blanker I pulse width; 4) With the same m/z ion, a longer blanker I pulse width lets more ions go through resulting in more ion counts but lower mass resolution. There is a conflict between the mass resolution and the duty cycle of the sample molecular ions (defined as the number of molecular ions detected divided by the number of ions generated at the sample surface).

Mass resolving power for this mass spectrometer can be almost infinitely increased, but the transmission of the secondary ions is decreased correspondingly. When the duty cycle drops below a certain range, a useful mass spectrum or ion image cannot be obtained.

An example to show the relationship between the mass resolution and blanker I pulse width is shown here for sphingomyelin (m/z: 731). The sphingomyelin molecular ion (m/z 731) has a transmission time of 1.8 μs through blanker I and a total flight time of ~60 μs to the detector. 5mg of sphingomyelin powder was dissolved in 50% formamide/methanol to make a solution of 2×10^{-3} mol/L. A few nL of this solution was deposited on a silicon wafer and vacuum dried.

With blanker I pulse width at 4.0 μs, a spectrum of sphingomyelin is shown in Figure 35. The sphingomyelin monomer, dimer, trimer and tetramer peaks, all singly charged, were observed. The mass resolution of the singly charged peak was ~13. This spectrum also demonstrates that how soft the massive cluster ion beam was since the tetramer single charged peak was observed. The massive cluster impact broke neither the chemical bonds inside the molecules, nor the intermolecular forces.

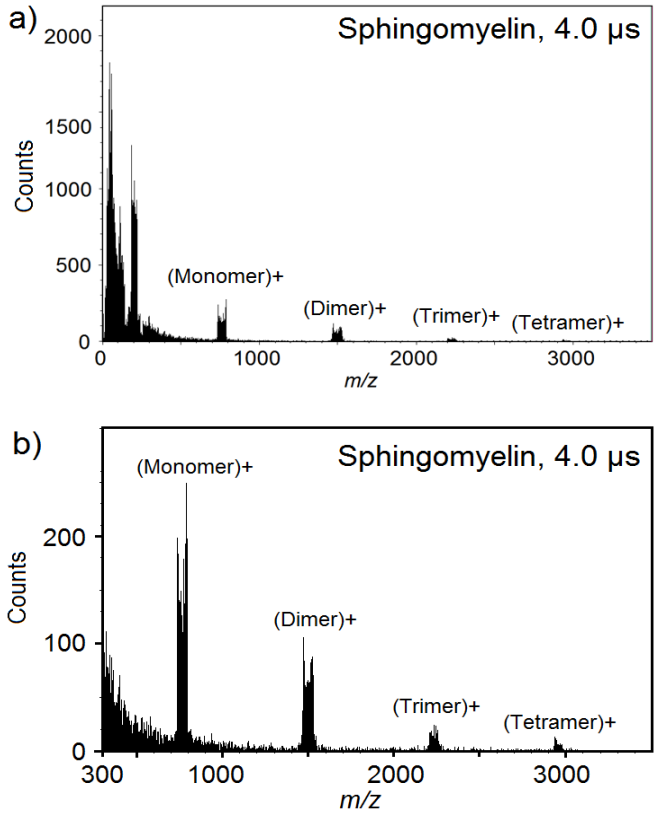

Figure 35. Full mass spectrum (a) and partial mass spectrum (b) of sphingomyelin (m/z 731) with blanker I pulse width at 4.0 μs. Sphingomyelin single charged, dimer single charged, trimer single charged and tetramer single charged peaks were observed. The mass resolution of the monomer peak was ~13. The effective pulse width and the transmission time through Blanker I for the monomer peak were2.3 μs and 1.6 μs.

With blanker I pulse width at 3.0 μs, a spectrum of sphingomyelin is shown in Figure 36. The tetramer singly charged peak has disappeared compared with Figure 21 because its transmission time (~3.5 μs) was longer than the blanker I pulse width. The mass resolution of the single charged peak was increased to ~22.

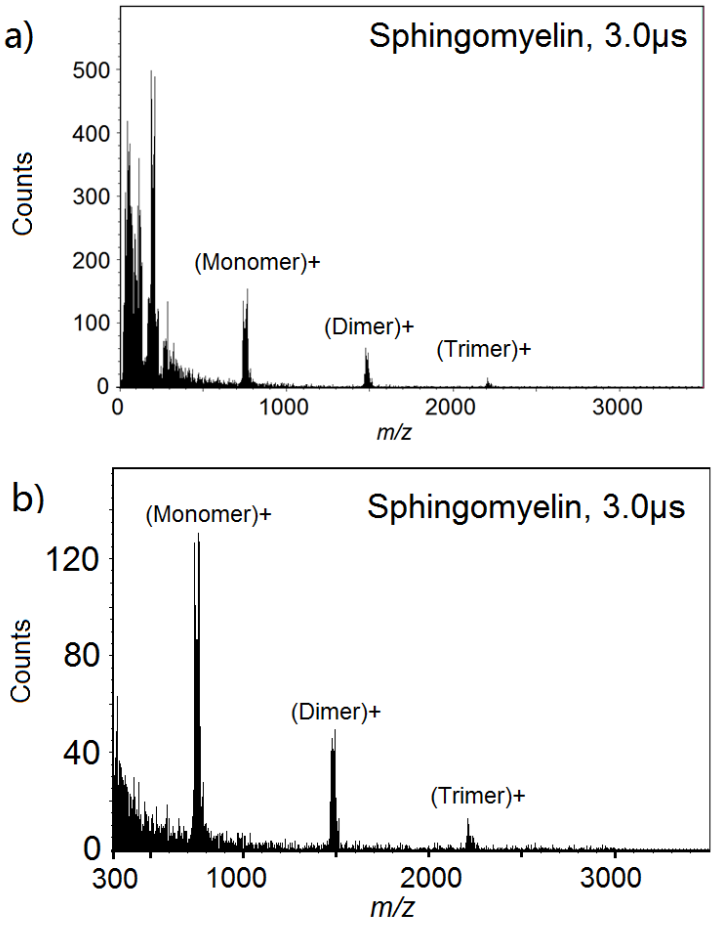

Figure 36.Full mass spectrum (a) and partial mass spectrum (b) of sphingomyelin (m/z 731) with blanker I pulse width at 3.0 μs. The sphingomyelin tetramer peak disappeared compared with Figure 35. The mass resolution of the monomer peak was increased to ~22 compared with 4 μs blanker I pulse width. The effective pulse width and the transmission time through Blanker I for the monomer peak were 1.4 μs and 1.6 μs.

With blanker I pulse width at 2.5 s, a spectrum of sphingomyelin is shown in Figure 37. Now the trimer singly charged peak has also disappeared because its transmission time (3.0 μs) was longer than the blanker I pulse width. The mass resolution of the single charged peak was increased to ~32. Note that the dimer signal is still seen even though the calculated transmission time is 2.5 μs.

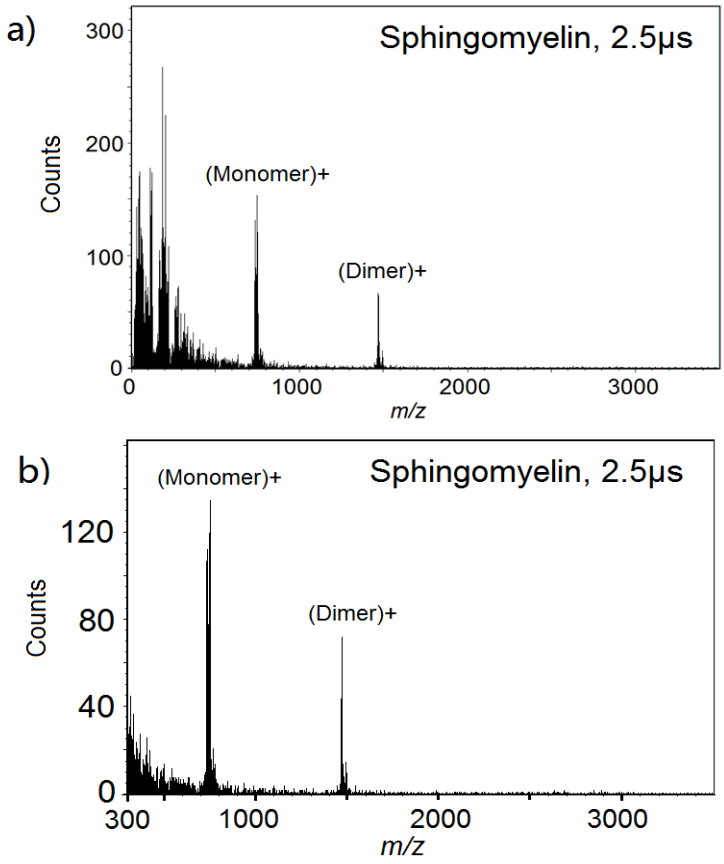

Figure 37.Full mass spectrum (a) and partial mass spectrum (b) of sphingomyelin (m/z 731) with blanker I pulse width at 2.5 μs. The sphingomyelin trimer peak disappeared compared with Figure 36. The mass resolution of the monomer peak was increased to ~32 compared to 3 μs blanker I pulse width. The effective pulse width and the transmission time through Blanker I for the monomer peak were 0.9 μs and 1.6 μs.

With blanker I pulse width at 2.0 s, a spectrum of sphingomyelin is shown in Figure 38. Now the dimer singly charged peak is not seen because its transmission time (2.5 μs) was longer than the blanker I pulse width. The mass resolution of the single charged peak was increased to ~78.

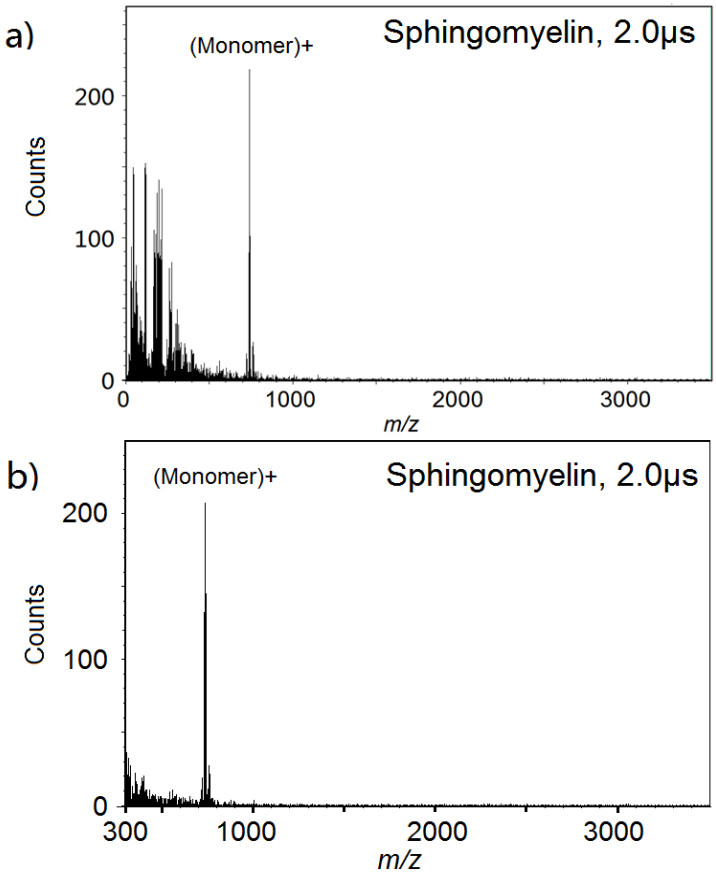

Figure 38. Full mass spectrum (a) and partial mass spectrum (b) of sphingomyelin (m/z 731) with blanker I pulse width at 2.0 μs. The sphingomyelin dimer peak disappeared compared with Figure 37. The mass resolution of the monomer peak was increased to ~78 compared with 2.5 μs blanker I pulse width. The effective pulse width and the transmission time through Blanker I for the monomer peak were 0.4 μs and 1.6 μs.

From the above sphingomyelin spectrum changes from 4.0 μs to 2.0 μs blanker I pulse width, the mass resolution was improved from 13 to 78, but the duty cycle of the secondary ions was decreased. When the blanker I pulse width was smaller than the transmission time for a given species through blanker I, the corresponding peak disappeared. A balance needs to be kept between the mass resolution and the peak intensity.

The experimental transmission time is smaller than the theoretical transmission time. Here the monomer transmission time was calculated based on equation 2 and 3. First the mass resolving power was calculated based on the mass and the FWHM. The total flight time was known. So the experimental effective pulse width could be calculated. The transmission time is equal to the blanker I pulse width subtracted by the effective pulse width. The experimental transmission time for sphingomyelin monomer was calculated from the above spectra to be ~1.6 μs. It is smaller than the theoretical transmission time 1.8 μs. This is because of ions near the end of Blanker I when the 200 V was turned on were only deflected partially that they could still arrive at the detector.

When the mass resolution was improved from 4 μs blanker I pulse width to 2.0 μs, the relative intensity of low m/z ions to the monomer peaks were decreased and the signal to background ratio of the monomer was improved. This implied to us that a high mass resolution was preferable to minimize signal/background. But in this TRIFT instrument, the mass resolution scales inversely with the duty cycle. In order to solve this problem, either the primary ion beam needs to be pulsed or a DC secondary ion microscope imaging mass spectrometer is required.

CHAPTER 4

MASS SPECTRA OF ORGANICS, LIPIDS, PEPTIDES AND PROTEINS

Intact desorption and ionization of biomolecules is important for imaging mass spectrometry to be useful in discovering the distribution of intact biomolecules. Here mass spectra of various organic molecules, lipids, peptides, proteins and oligonucleotides were obtained to demonstrate the intact mass range for MCI technology. Mass spectra were typically obtained using the third contrast diaphragm (CD3, 0.21 mm diameter) which is the same for imaging test at next chapter.

Mass spectra of the compounds discussed below which have been obtained before with other mass spectrometry methods (SIMS, MALDI, EDI and so on) are cited and reprinted (with permission) here for comparison. EDI (Electrospray Droplet Impact) is developed by Kenzo Hiraoka and his colleagues. It uses water cluster impact to desorb and ionize molecules. MCI has been demonstrated to have similar performance for molecular peak detection compared with MALDI, EDI, or better performance than the SIMS with small cluster ion beam.

4.1 Organic Molecules

α-NPD (N,N'-Di(1-naphthyl)-N,N'-diphenylbenzidine) (588 Da) was donated by Dr. Jiro Matsuo (Kyoto University). It was deposited as a homogeneous layer on silicon wafer with a thickness of 112.9 nm. α-NPD is a material used in OLED devices. Molecular peak of α-NPD was obtained before using Laser Desorption/Ionization TOF

(LDI-TOF) by Takaya Satoh (MS Business Unit, JEOL Ltd.). Here MCI-TRIFT was used to get a similar molecular peak with 1.4 μs blanker I pulse (Figure 39).

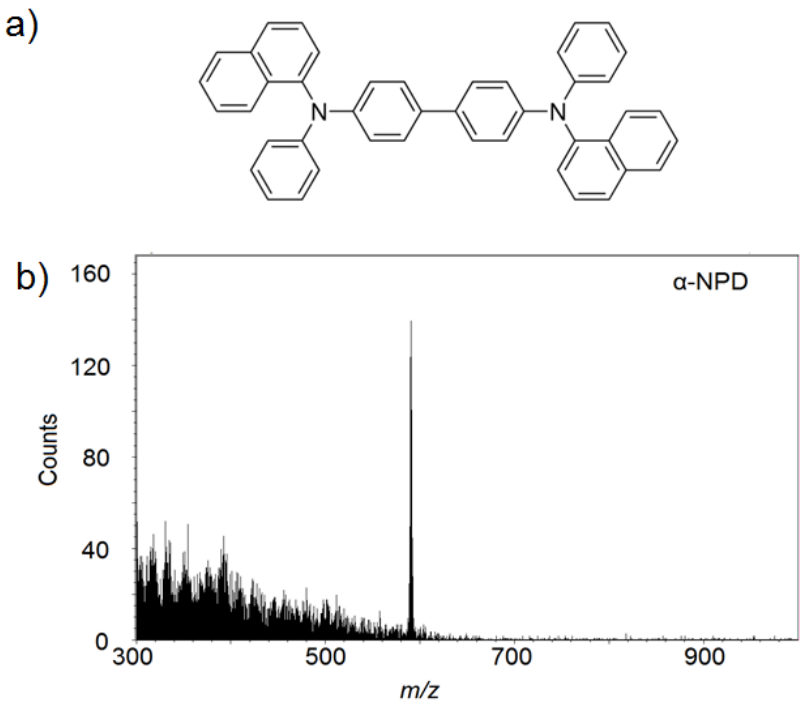

Figure 39. (a): structure of α-NPD, this is a material used in OLED devices; (b) spectrum of α-NPD, 1.4 μs blanker I pulse width, the 1+ peak was clearly observed.

2-TNATA (4,4',4"-Tris[2-naphthyl(phenyl)amino]triphenylamine) (896 Da) was also donated by Dr. Jiro Matsuo. A thickness of 106 nm of 2-TNATA was deposited on silicon wafer. 2-TNATA is a material used in OLED devices. The blanker I pulse width was 2.0 μs. The 1+ peak was clearly observed (Figure 40).

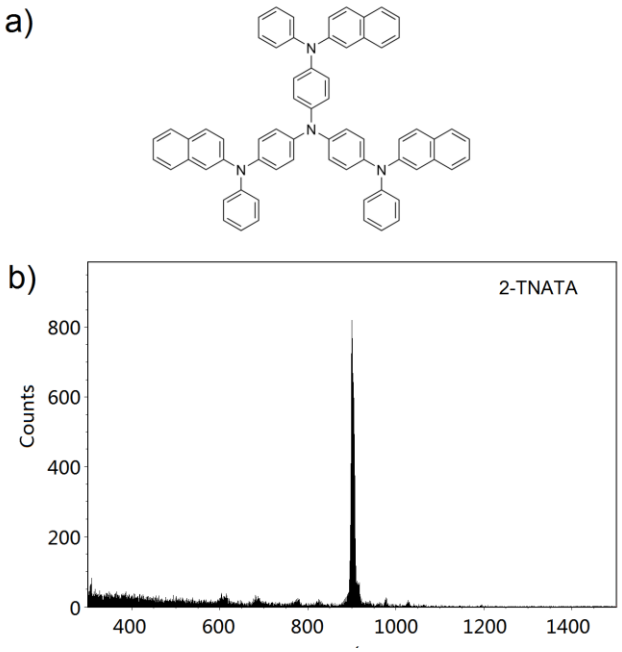

Figure 40. (a): structure of 2-TNATA. This is a material used in OLED devices; (b): mass spectrum of 2-TNATA, 2.0 μs blanker I pulse width, the 1+ peak was clearly observed.

Irganox 1010 (1178 Da): this detergent multilayer sample was donated by Ian Gilmore (National Physical Laboratory, UK) and used without further processing. It contained three 95 nm and two 47.5 nm thick layers of irganox 1010 interspersed with 2.5 nm layers of irganox 314. Structure of irganox 1010 was shown in Figure 41a. A negative ion spectrum of irganox 1010 was obtained before by Lee et al. (Lee et al. 2010) using Ar_{700}^{+} (no characteristic peaks were shown in positive spectrum) (Figure 41b). The molecular peak was not observed in this spectrum. Fragment peaks were used to monitor the irganox 1010 parent molecules.

However, in the spectrum obtained with MCI, an intense molecular peak was observed (Figure 41c). Blanker I pulse width was 2.2 μs.

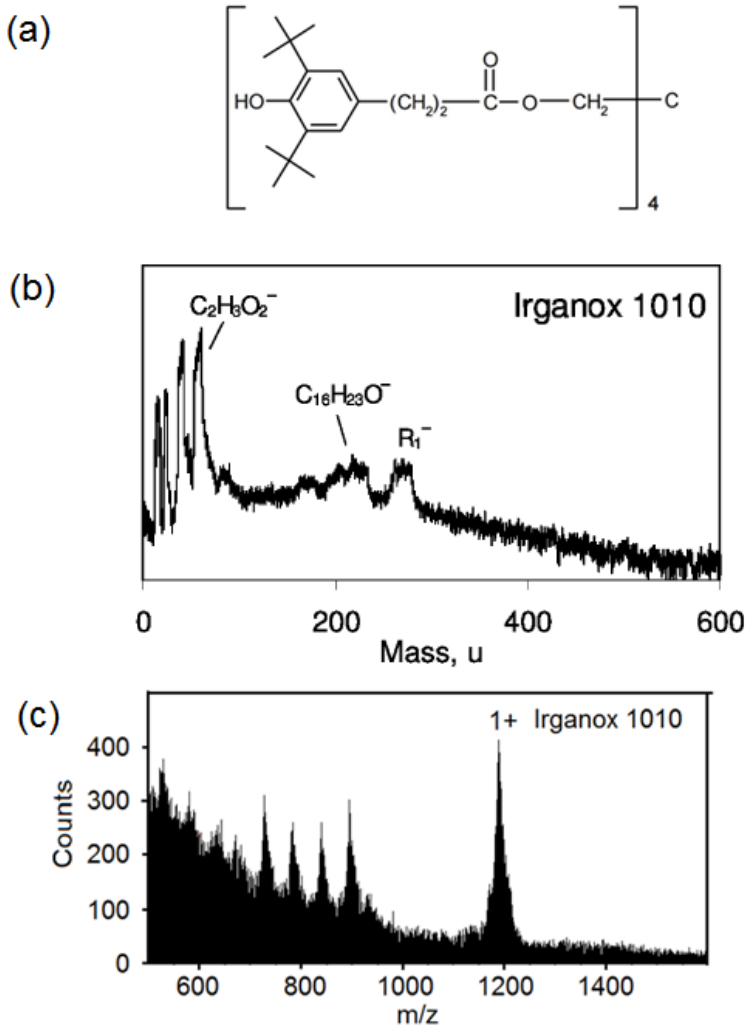

Figure 41.(a): structure of Irganox 1010, it is an additive into polyolefin; (b): negative ion spectrum of irganox 1010 obtained using Ar_{700}^{+}, molecular peak was not observed, fragment peaks were used to monitor the irganox 1010 parent molecule, reprinted with permission from Lee et al. (2010), Copyright 2010 American Chemical Society; (c): mass spectrum of Irganox 1010 obtained with MCI-TRIFT, 2.2 μs blanker I pulse width. The 1+ peak was clearly observed. The four fragment peaks in a series were due to the loss of a single side chain, R, then subsequent additional losses of t-butyl groups from the remaining side chains.

Rhodamine B chloride (mass without Cl^-, 443 Da): the structure of this molecule is shown in Figure 42a. Figure 42b shows a spectrum of rhodamine B obtained by EDI (Hiraoka, Asakawa, and Takaishi 2013). The molecular peak without Cl^- was observed.

The sample in the MCI-TRIFT test was purchased from Sigma Aldrich (St. Louis, MO) and dissolved in deionized water to make a 1.0×10^{-4} mol/L solution. The solution was deposited on a silicon wafer and air dried. Blanker I pulse width was 2 μs. The single charged peak (Figure 42c) represented the rhodamine B without the Cl^- ion.

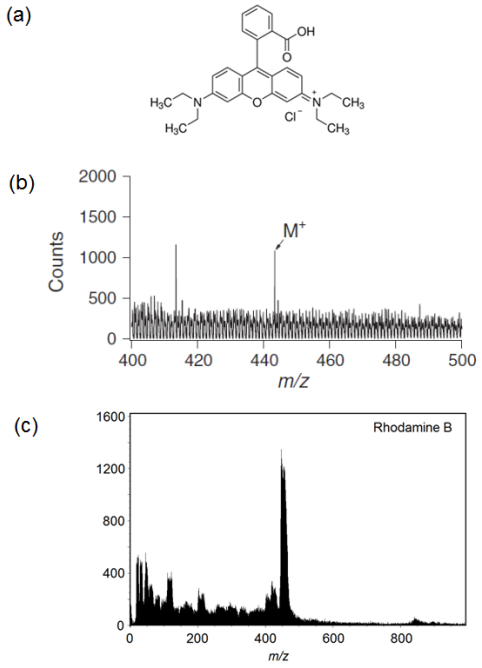

Figure 42.(a): structure of rhodamine B molecules, it is a fluorescent dye and a diethylammonium chloride;(b): mass spectrum of rhodamine B acquired by EDI, the molecular peak was observed, reprinted from Hiraoka, Asakawa, and Takaishi (2013), Copyright 2013 John Wiley & Sons, Ltd.; (c): mass spectrum of rhodamine B obtained by MCI-TRIFT, the 1+ peak without the Cl^- ion was clearly observed. 2 μs blanker I pulse width.

4.2 Lipids

The phosphocholine has two side chains (R, R') (Figure 43a). Figure 43b shows a mass spectrum obtained by EDI for 1-palmitoyl-2-stearoyl-sn-glycero-3-phosphocholine (PC16:0/18:0) (Asakawa et al. 2010). The $(M+H)^+$ and $(M+Na)^+$ peaks were observed. Two fragment peaks at m/z 479 and m/z 507 corresponded to the loss of palmitoyl or stearoyl (283Da) side chain.

In the MCI-TRIFT test, L-α-phosphatidylcholine (from egg yolk, a major component in eukaryotic cell membrane) was purchased from Sigma Aldrich (St. Louis, MO) and dissolved in formamide to make a 1.8×10^{-4} mol/L solution. The solution was deposited on a silicon wafer and air dried. This was a natural sample and contained a mix of different side chains (e.g. 33% palmitic, 31% oleic, 13% stearic, 15% linoleic and other minor fatty acids). A fairly high resolution mass spectrum was obtained using 2 μs blanker I pulse width (Figure 43c). Peak A was identified as the phosphocholine carrying a palmityl (C_{16}) and oleyl (C_{18}) (281Da) side chains. Peak B could be an overlap of two oleyl side chains or $(A+Na)^+$. Peak C and D corresponded to loss of the palmityl or oleyl side chain of peak A. Loss of an oleyl side chain of peak B might also contribute to peak C. The identity of the peak at m/z 850 is unknown. The L-α-phosphatidylcholine monomer, dimer and trimer, all singly charged peaks, were observed using a blanker I pulse width of 6 μs, the mixture led to somewhat broadened (unresolved) peaks (Figure 43d).

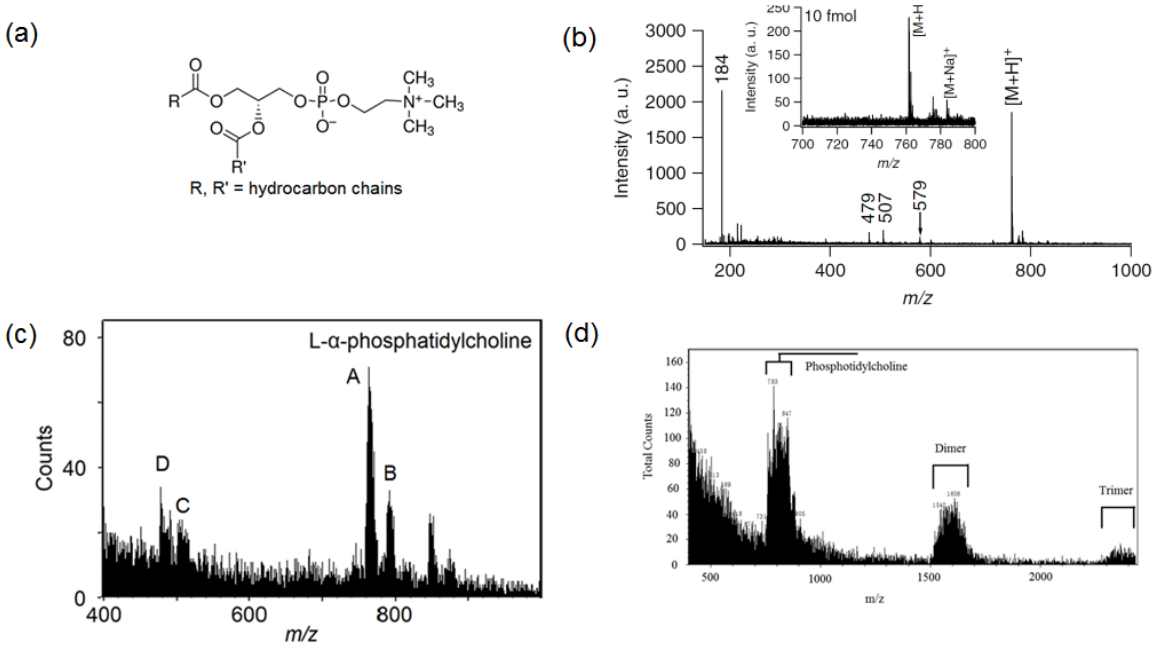

Figure 43.(a): structure of phosphocholine with R and R' side chains; (b): mass spectrum of 1-palmitoyl-2-stearoyl-sn-glycero-3-phosphocholine (PC16:0/18:0) obtained by EDI, $[M+H]^+$, $[M+Na]^+$ and two fragments peaks (m/z 479 and 507, loss of palmitoyl or stearoyl correspondingly) were observed, reprinted with permission from Asakawa et al. (2010), Copyright 2010 John Wiley & Sons, Ltd.; (c): the mass spectrum of egg yolk L-α-phosphatidylcholine with 2 μs blanker I pulse width, peak A had a C_{16} and C_{18} side chains, peak B was attributed to two C_{18} side chains or $[A+Na]^+$, peak C and D corresponded to loss of a single C_{16} or C_{18} side chain from peak A; (d): the mass spectrum of egg yolk L-α-phosphatidylcholine with 1+, dimer 1+ and trimer 1+ peaks (a large blanker I pulse width, 6 μs, was used to view the trimer peak).

Sphingomyelin (731Da): sphingomyelin was purchased from Avanti Polar Lipids Inc. (Alabaster, AL) and dissolved into 50% formamide/water solution. It was further diluted by formamide to 2×10^{-4} mol/L. The solution was deposited on silicon wafer and vacuum dried. In order to get the peaks for polymer peaks, blanker I pulse width was set at a large value, 6 μs. Singly charged, dimer, trimer, tetramer, pentamer and hexamer peaks were observed (Figure 44). A higher resolution mass spectrum was shown in.

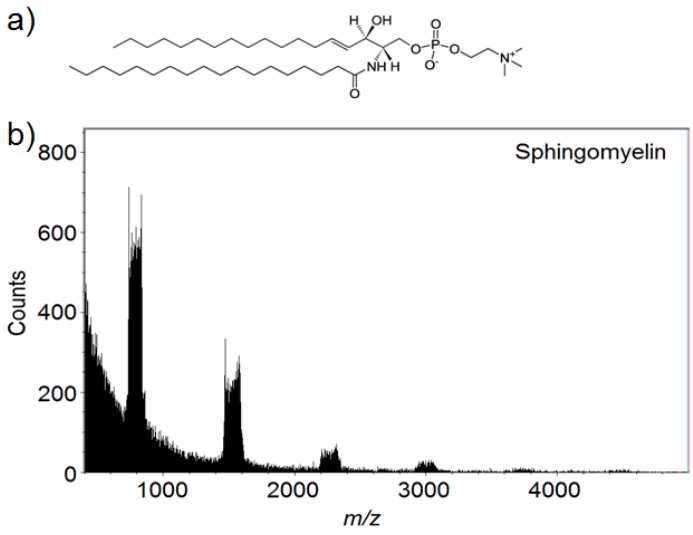

Figure 44. (a):structure of sphingomyelin;(b): mass spectrum of sphingomyelin, 6 μs blanker I pulse width. The 1+, dimer 1+, trimer 1+, tetramer 1+, pentamer 1+ and hexamer 1+ peaks were observed.

1,2-Dioleoyl-sn-glycero-3-phosphocholine (786Da): it was purchased from Sigma-Aldrich (St. Louis, MO) and dissolved in $CHCl_3$ to make a 0.25 mol/L solution. The solution was deposited on a silicon wafer and air dried. Blanker I pulse width was 2 μs (Figure 45).

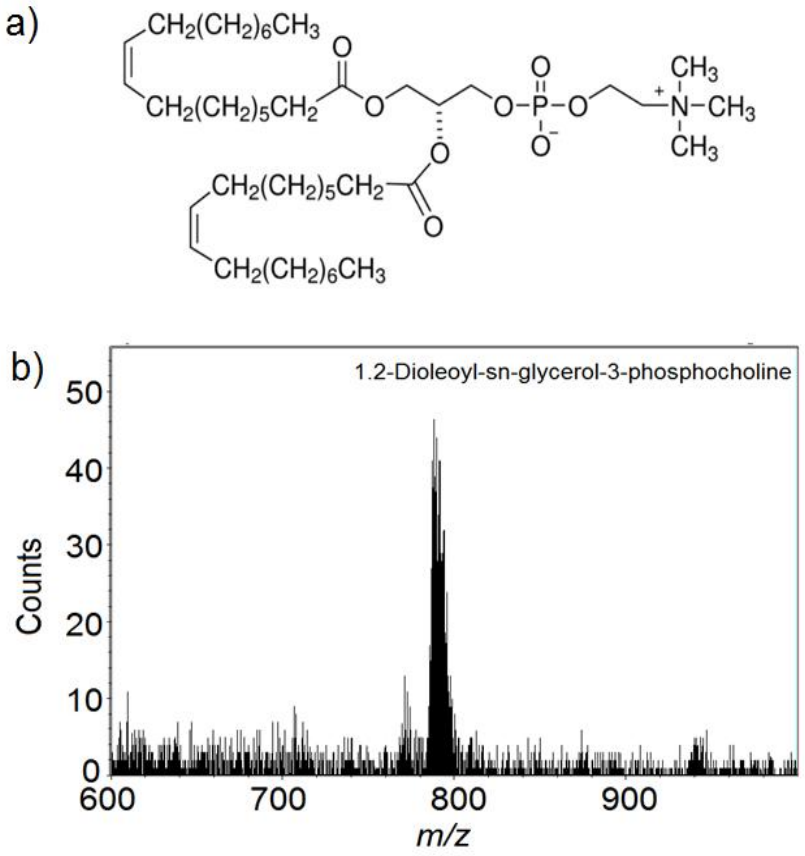

Figure 45.(a): structure of 1,2-Dioleoyl-sn-glycero-3-phosphocholine;(b): mass spectrum of 1,2-Dioleoyl-sn-glycero-3-phosphocholine, 2 μs blanker I pulse width. The 1+ peak was clearly observed.

Cholesterol (386Da): it was dissolved in $CHCl_3$ to make a 0.5 mol/L solution. 30 μL of this solution was deposited on a silicon wafer and air dried. Blanker I pulse width was 5 μs.

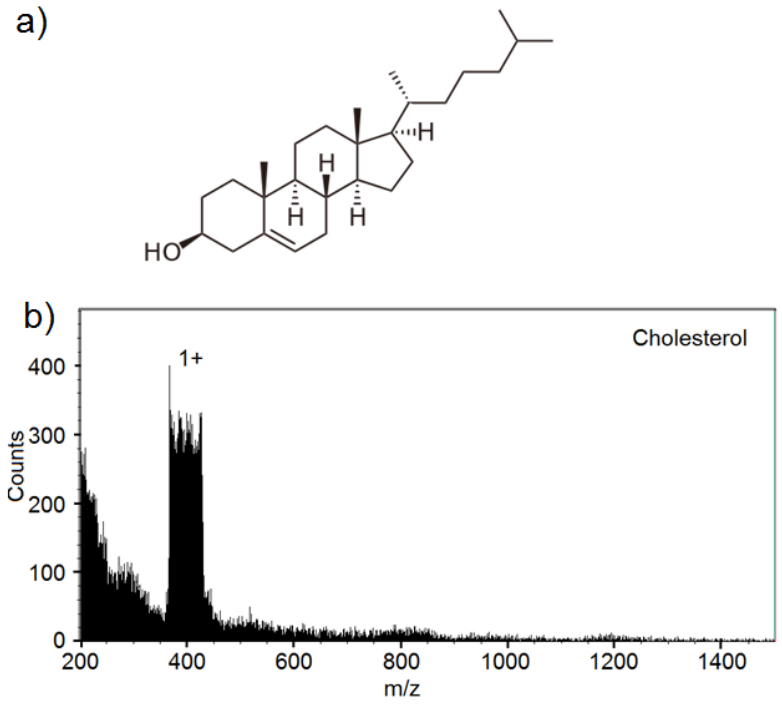

Figure 46. (a): structure of cholesterol; (b): mass spectrum of cholesterol, 5 μs blanker I pulse width. The singly charged peak was clearly observed.

4.3 Peptides

Bradykinin (1060Da): amino acid sequence is Arg-Pro-Pro-Gly-Phe-Ser-Pro-Phe-Arg. Figure 47a shows a spectrum obtained by EDI (Asakawa et al. 2007). Singly charged molecular peak was observed.

The sample in the MCI-TRIFT test was purchased from American Peptides (Sunnyvale, CA) and dissolved in deionized water to make a 0.005 M solution. The blanker I pulse width was 2 μs. The $(M+H)^+$ peak and the $(M+Na)^+$ peak were clearly observed (Figure 47b).

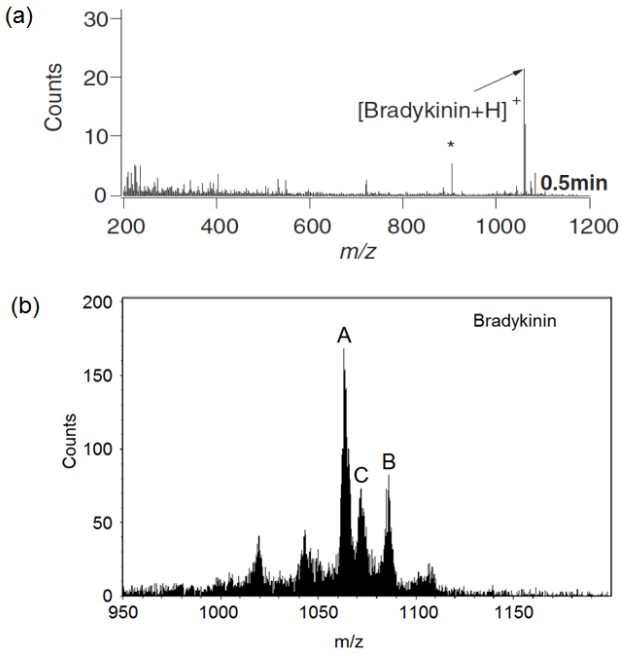

Figure 47. (a), mass spectrum of bradykinin obtained by EDI, $[M+H]^+$ was observed, reprinted with permission from Asakawa et al. (2007), Copyright 2007 John Wiley & Sons, Ltd.; (b) mass spectrum of bradykinin (1060 Da) obtained by MCI-TRIFT. 2 μs blanker I pulse width. From the 22 Da mass difference between peaks A and B, A was assigned to$(M+H)^+$ and B was assigned to $(M+Na)^+$.The mass difference between B and C was 14 Da so C might be $(M+Na-NH_2)^+$.

Angiotensin II (1046 Da): the amino acid sequence is Asp-Arg-Val-Tyr-Ile-His-Pro-Phe. Figure 48a shows a mass spectrum acquired by EDI (Asakawa and Hiraoka 2011). The $[M+H]^+$ was observed.

In the MCI-TRIFT test, the sample was purchased from Sigma-Aldrich (St. Louis, MO) and dissolved in deionized water to make a 5×10^{-4} mol/L solution. Blanker I pulse width was 2 μs. The $(M+H)^+$ and $(M+Na)^+$ peak were clearly observed (Figure 48b).

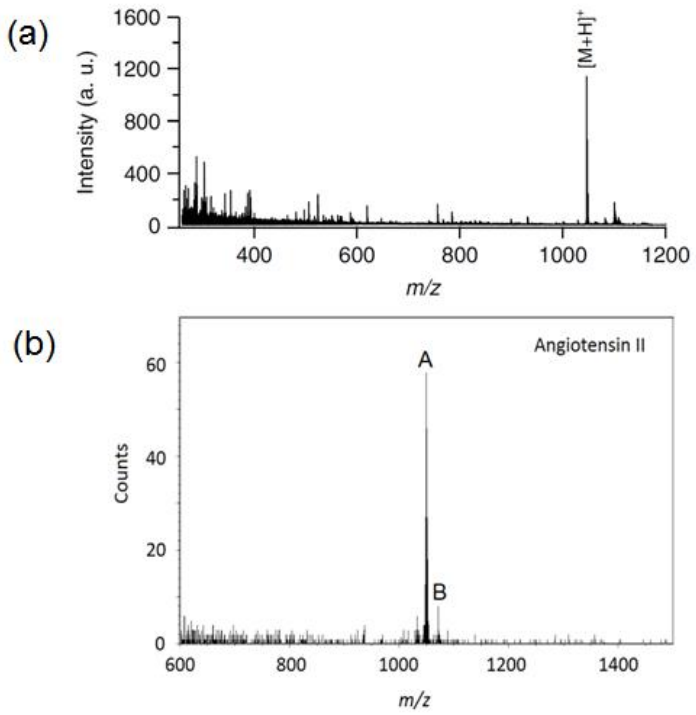

Figure 48. (a): mass spectrum of angiotensin II obtained by EDI (Asakawa and Hiraoka 2011), $[M+H]^+$ was observed, reprinted with permission from Asakawa and Hiraoka (2011), Copyright 2011 John Wiley & Sons, Ltd.; (b): mass spectrum of angiotensin II obtained by MCI-TRIFT. 2 μs blanker I pulse width. The mass difference between peaks A and B was 22 Da and so peak A was assigned to $(M+H)^+$ and peak B was assigned to $(M+Na)^+$ peaks.

Peptide Mixture: a peptide mixture containing angiotensin II(1046Da), angiotensin I (1296 Da), substance P(1347 Da), bombesin (1619Da), ACTH clip 1-17 (2093 Da), ACTH clip 18-39 (2465 Da) and somatostatin 28 (3147 Da) was bought from Bruker Company. A MALDI spectrum of this peptide mixture (refer to the peptide

calibration standard product manual, Bruker Company, USA) was shown in Figure 49a. Peaks for all the peptides in the mixture were observed.

In the MCI-TRIFT test, the sample was dissolved in deionized water to make a 25 μmol/L solution. The solution was deposited on silicon wafer and vacuum dried. Peaks corresponding to different peptides were obtained. Blanker I pulse width was 8 μs. The peaks of angiotensin I and substance P overlapped with each other due to a big blanker I pulse width (Figure 49).

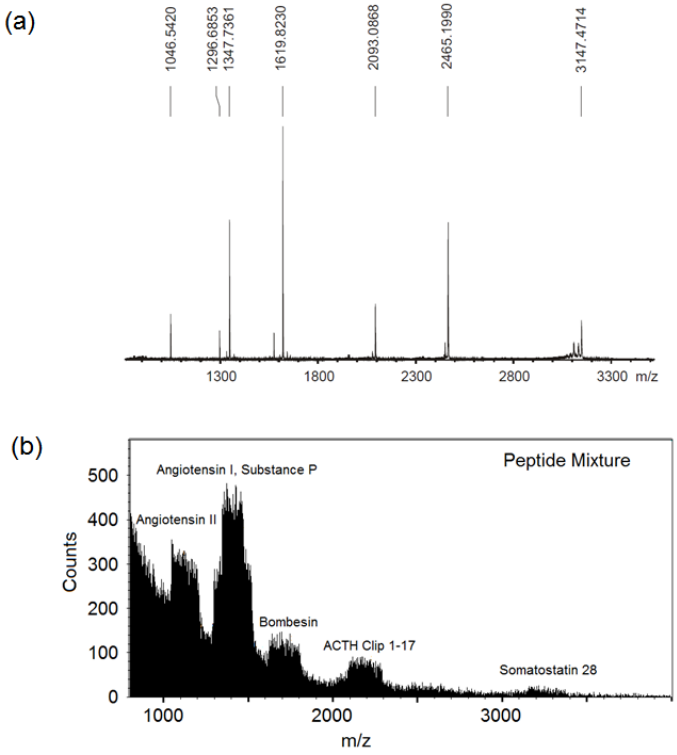

Figure 49. (a): MALDI spectrum of peptide calibration standard, reprinted from the product manual (Bruker Company, USA); (b): Mass spectrum of a peptide mixture acquired with MCI-TRIFT. 8 μs blanker I pulse width. Peaks for different peptides were observed.

4.4 Proteins

Insulin (5808 Da): Asakawa et al. (Asakawa et al. 2007) obtained an insulin positive ion spectrum using water cluster impact. The singly and doubly charged peaks were observed (Figure 50a).

In the MCI-TRIFT test, insulin (Sigma Aldrich, St. Louis, MO) was dissolved in formamide to make a 5×10^{-5} M solution. Blanker I pulse width was 5 μs. The singly charged and doubly charged peaks were observed (Figure 50b). The insulin chain A and B peaks were also observed.

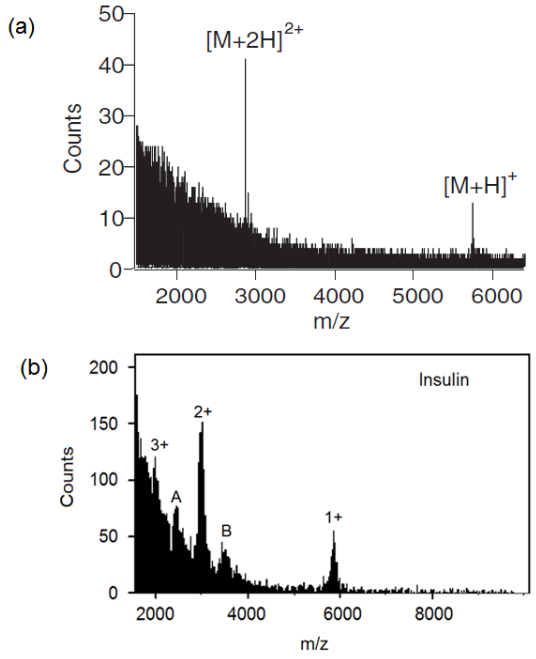

Figure 50. (a): mass spectrum of insulin obtained with water cluster impact by Asakawa et al. (Asakawa et al. 2007), singly and doubly charged peaks were observed, reprinted with permission from Asakawa et al. (2007), Copyright 2007 John Wiley & Sons, Ltd.; (b) mass spectrum of insulin obtained with MCI-TRIFT. 5 μs blanker I pulse width. The insulin 1+, 2+, 3+ peaks, chain A and B were also observed.

Lysozyme (14.3 kDa): a spectrum of lysozyme was acquired by Hiraoka, Mori, and Asakawa (Hiraoka, Mori, and Asakawa 2006) with water cluster impact. Singly (barely seen) and multiply charged peaks were observed (Figure 51a).

In MCI-TRIFT, the lysozyme sample was dissolved in a 0.01 M HCl solution to make a concentration of 0.001 mol/L. Blanker I pulse width was 12 μs. The singly charged peak was barely seen. The doubly charged and triply charged peaks were observed (Figure 51b).

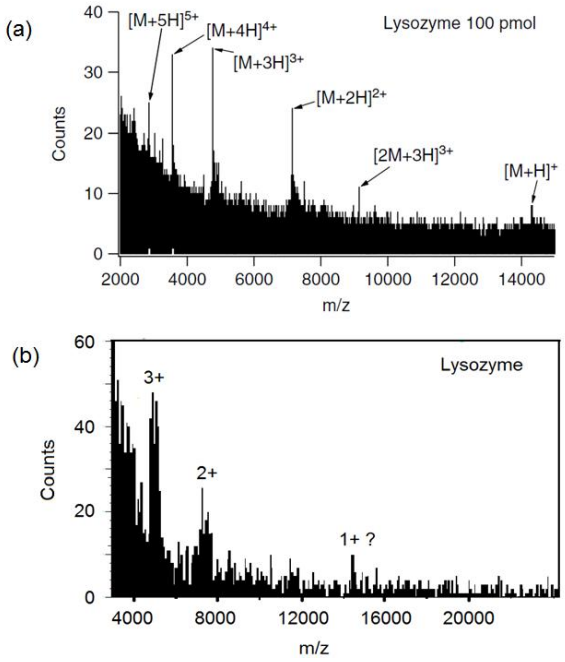

Figure 51. (a): mass spectrum of lysozyme obtained by EDI, singly and multiply charged peaks were observed, singly charged peak was barely seen, reprinted with permission from Hiraoka, Mori, and Asakawa (2006), Copyright 2006 John Wiley & Sons, Ltd.; (b): mass spectrum of lysozyme obtained by MCI-TRIFT. The 1+ peak was barely observed which might be due to the detector sensitivity. The 2+ and 3+ peaks were clearly observed.

4.5 Oligonucleotides

Typically, MALDI is used to detect oligonucleotides in the 10-50 base range, ESI is usually used for oligonucleotides with large number of bases detection. SIMS with atomic ion beam or cluster ion beam have not been proven to be effective in the detection of oligonucleotides. Here tests on oligonucleotides were done to demonstrate the capability of MCI.

Oligo(dT)6mer (1763 Da): 10 μg of Oligo(dT)6mer was dissolved in 20 μL deionized water. The solution was deposited on silicon wafer and vacuum dried. Negative mode was used with sample voltage -3055 V. Source voltage was at -15 kV. Post acceleration was at +6 kV. Blanker I pulse width was 5 μs. A spectrum with positive mode was also obtained with lower S/N.

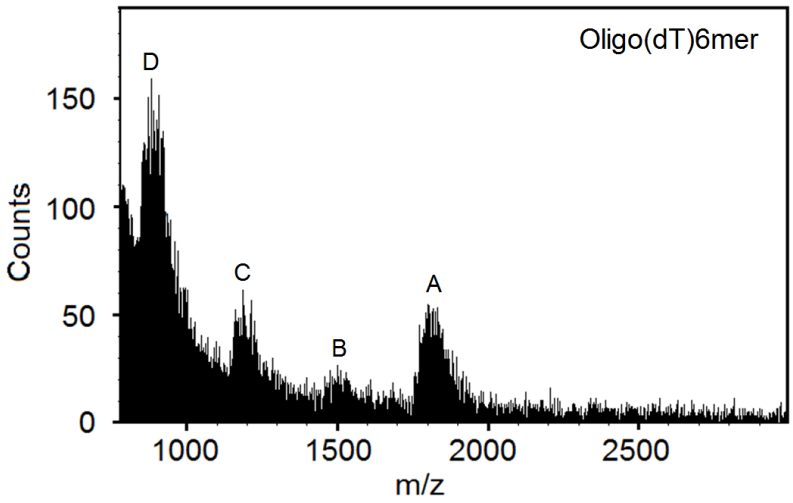

Figure 52.Negative mass spectrum of Oligo(dT)6mer. 5 μs blanker I pulse width. A was the negatively charged molecular peak. B and C may be the fragments of (dT)6mer or the impurities of (dT)5mer and (dT)4mer. D may be negatively double charged molecular peak, or a fragment peak of (dT)6mer, or an impurity of (dT)3mer in the sample.

Oligo(dT)15mer (4501Da): 10 µg of oligo(dT)15mer was dissolved in 20 µL deionized water. The solution was deposited on silicon wafer and vacuum dried. Negative mode was used with sample voltage -3055 V. Source voltage was at -15 kV. Post acceleration was at +6 kV. Blanker I pulse width was 8 µs. The absence of fragment peaks and the high intensity of the 2- peak suggests that peak B and C in Figure 38 were probably the impurities and that peak D was the 2- species.

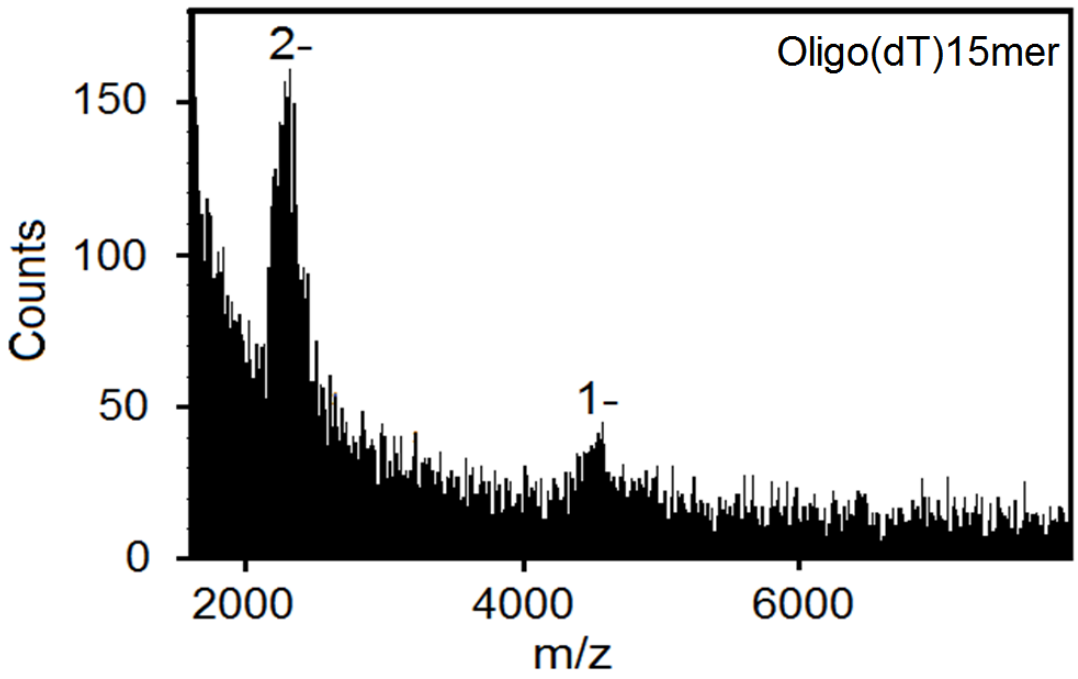

Figure 53. Negative mass spectrum of Oligo(dT)15mer. 8 µs blanker I pulse width. The 1- and 2- peaks were clearly observed.

4.6 Raw Salmon and Shrimp

In order to test the capability of MCI-TRIFT to acquire a lipid spectrum from tissue sample, salmon and shrimp in a freshly prepared sushi purchased at a local grocery store was used. The edge of a glass slide was used to scrape small amounts of material off the sample surfaces and smear them onto silicon wafers. The samples were immediately placed in the instrument with no further sample processing. The whole process took only ten minutes.

The mass range from m/z 700 to 1050 is displayed. The lipid contents in the cells are mainly located in this mass range. The peak pattern of the salmon lipids acquired by MCI-TRIFT (Figure 54a) was very similar to that observed by Porcari et al. and had been assigned to triacylglycerols (TAGs) (Porcari et al. 2012) (Figure 54b). The peak pattern of the shrimp lipids (Figure 54c) obtained by MCI-TRFIT might be due to the assignments provided by Mika et al (Mika et al. 2013) (Figure 54d) acquired by MALDI-TOF for *Crangon crangon*.

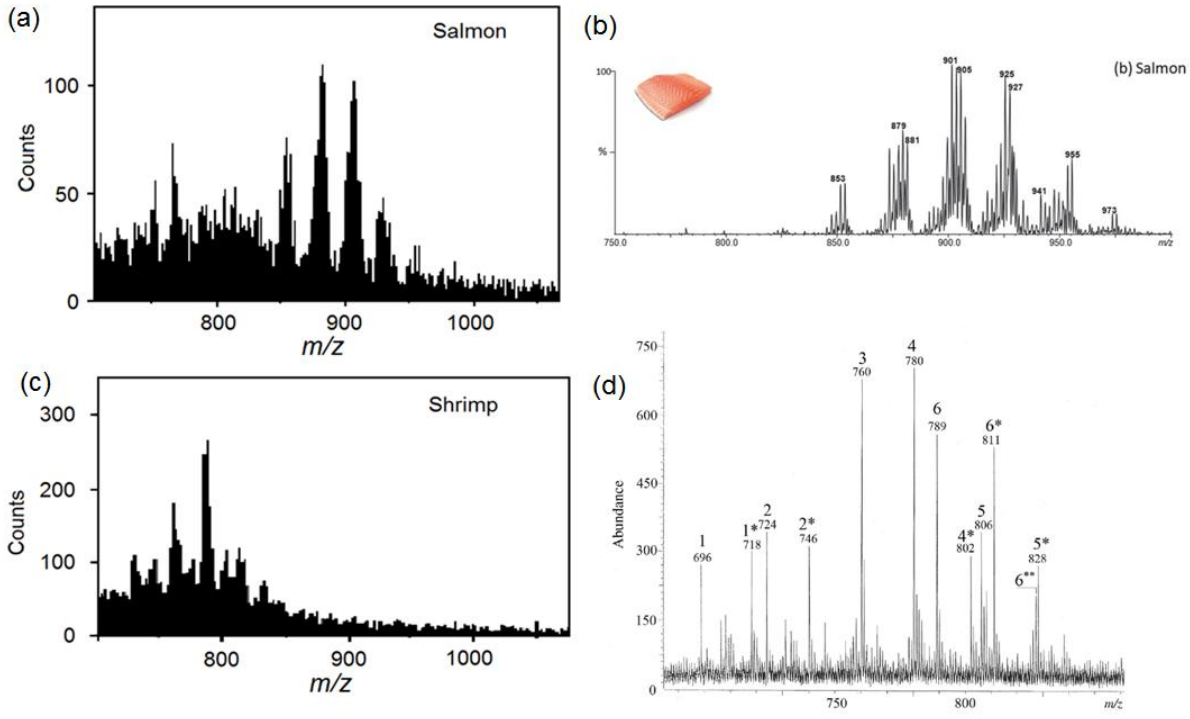

Figure 54. (a): mass spectrum of raw salmon obtained by MCI-TRIFT (1.04 m/z per bin, 2 μs blanker I pulse width), majority of the lipid peaks locate at m/z 850-950; (b): mass spectrum of salmon obtained with easy ambient sonic-spray ionization mass spectrometry (EASI-MS) by Porcari et al. (Porcari et al. 2012), a similar lipid peaks range was observed, reprinted with permission from Porcari et al. (2012), Copyright 2012 The Royal Society of Chemistry; (c): mass spectrum of shrimp (1.23 m/z per bin, 2 μs blanker I pulse width) obtained by MCI-TRIFT, majority of the lipid peaks locate at m/z 700-850; (d): MALDI-TOF spectrum of *Crangon crangon* obtained by Mika et al. (Mika et al. 2013) shows similar lipid peaks range.

CHAPTER 5

ION IMAGING AND LATERAL RESOLUTION

Besides the intact mass range, imaging resolution is another important parameter for an imaging technology to be useful. Imaging resolution determines the size of biological features which can be resolved (e.g. sub-cellular imaging of single cancer cell in patient tissues). In the MCI-TRIFT, since it is an ion microscope imaging mass spectrometer, the imaging resolution is determined by the secondary ion optics.

A 60× magnification of the sample ion image (~350 μm) was projected onto a position sensitive detector (micro-channel plates with phosphor screen). A Canon EOS camera was used with bulb mode to record the ion image on the back of the phosphor screen.

Here various patterned peptide, lipid and protein samples were used to demonstrate the imaging resolution achievable with the MCI-TRIFT system.

5.1 Bradykinin Imaging

In order to test the imaging resolution, patterned samples with physical boundary were used here.

5.1.1 Gold grid on Dry Bradykinin Layer

The gold grid has a physical bar and hole (Figure 55). This is a common way used to generate a known pattern.

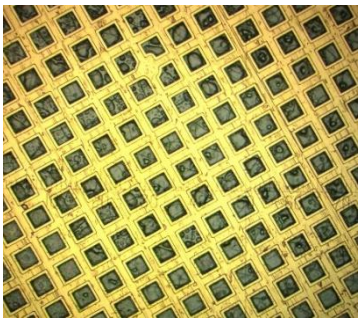

Figure 55. Optical image of the gold grid, 37 μm hole width, 25 μm bar width, 6 μm thickness (height).

Sample preparation: bradykinin (American Peptide, Sunnyvale, CA) was dissolved in deionized water to make a 0.16 mol/L solution. 20 μL of the solution was deposited on indium foil and vacuum dried. A clean gold grid (hole width 37 μm, bar width 25 μm thickness (height) 6 μm) was then placed on top of the dried bradykinin layer and attached at the edges with carbon paint. The indium substrate with the dried bradykinin layer was rough (5~20 μm), and the gold grid appeared to be somewhat loose presumably with gaps, so that the topography (height difference between the sample surface and the gold grid surface) of this ion-imaging sample was worse than the grid height of 6 μm.

In the imaging process, the blanker I pulse width was set to 8 μs. The blanker II pulse width was set to choose only the bradykinin peak. An ion image showed bright features in the holes where bradykinin was exposed to the primary cluster ion beam (Figure 56b). A gold peak was not observed. In order to generate a contrast pattern of the gold grid bar, the blanker II was chosen to select the low mass m/z ions from 0-250 Da. Both the gold grid bar and gold grid hole area were bright (Figure 56c). A line scan

across several bradykinin blocks in Figure 42b was done. The plot profile was obtained from ImageJ software. A 5 μm distance bar has been put on the plot profile to show the sharp trailing edge of each bradykinin block.

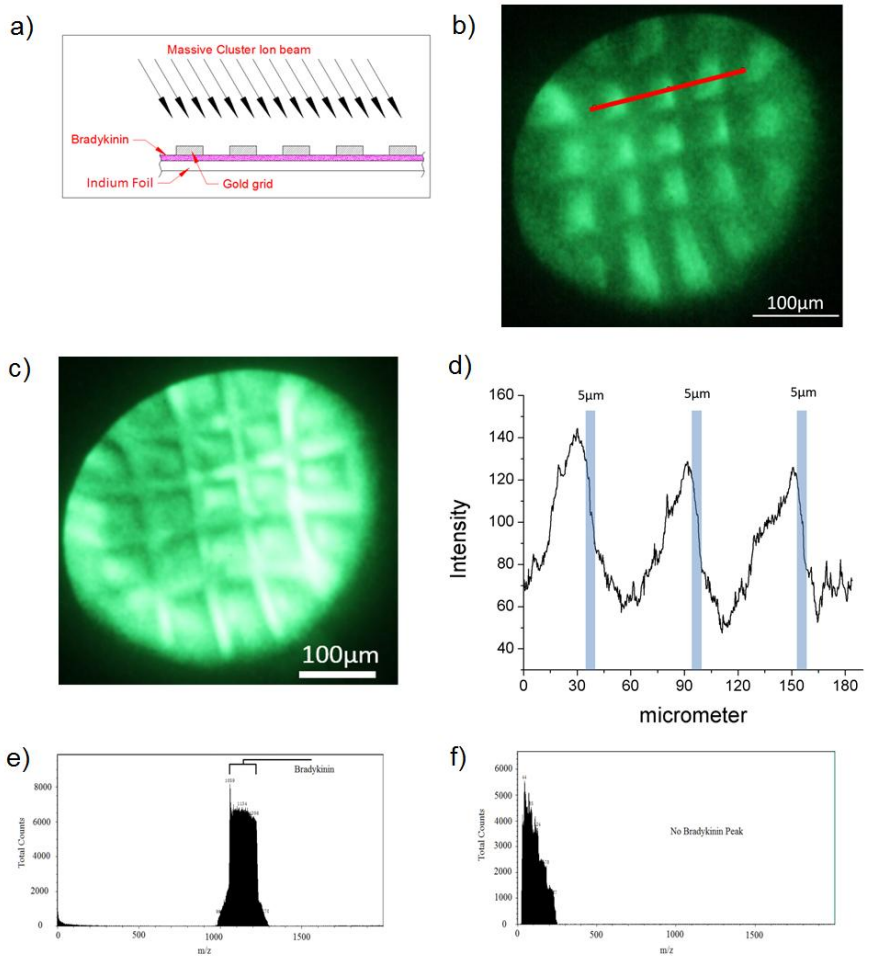

Figure 56.(a): sample preparation scheme;(b): ion image of bradykinin (20 μL of 0.16 mol/L on indium foil under a clean gold grid) (1.89 m/z per bin, 8 μs blanker I pulse width); (c): ion image of the contrast gold grid (m/z 0-250); (d):plot profile of the line scan at Figure 56b, 5 μm distance bar was placed on the plot; (e) and (f) are mass spectra for the corresponding ion image (Figure 56b, Figure 56c). The acquisition time of the mass spectrum in Figure 56e and of the bradykinin ion image in Figure 56b was 1.7 min.

From Fig 56b, we can see there was a shadowing (~10 μm) from the gold grid on the bradykinin hole area. The boundary of the bradykinin ion image was blurred by different extraction efficiency due to the topography difference.

5.1.2 Gold grid on Wet Bradykinin Solution

In order to decrease the topography difference, a gold grid was put on top of a wet bradykinin solution. The capillary action helped to minimize the gap between the gold grid and sample surface. 10mg of bradykinin was dissolved in 50 μL deionized water to make a 0.19 mol/L solution. ~0.3 μL of solution was deposited on silicon wafer. Clean gold grid was gently applied on top of the liquid. The gold grid was attached to the deposit by capillary action. The sample was air dried.

In Figure 57, there was less shadowing (~2 μm) on the bradykinin block compared with the dry sample deposits. A line scan across the bright bradykinin block showed an imaging resolution of ~3 μm which is better than the imaging resolution obtained in the dry sample.

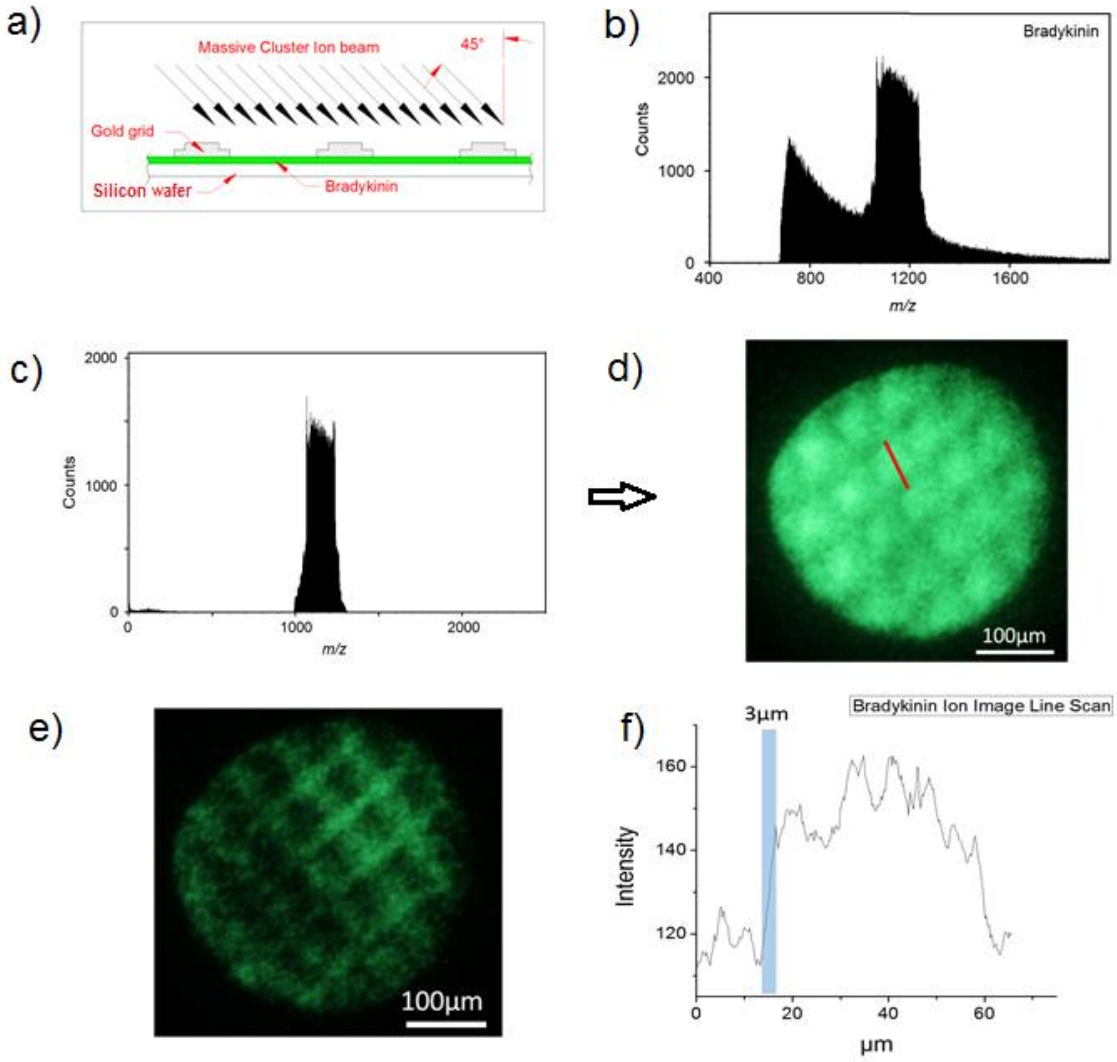

Figure 57.(a): a clean gold grid was put on top of a bradykinin solution;(b): bradykinin spectrum showing the signal to noise ratio;(c): spectrum obtained when the bradykinin ion window was selected by blanker II; (d): ion image corresponding to spectrum in Figure 57c, the gold grid hole area was brighter than the gold grid bar area;(e): the contrast gold grid ion image was obtained with the blanker II selecting low mass ion window; (f): a line scan across a bradykinin block demonstrated a resolution of ~3 µm.

5.1.3 Bradykinin Stripe Imaging

In order to further minimize the topography issue (the gold grid has an intrinsic height of 6 μm), a patterned dry deposit on a silicon wafer without any gold grid on top was used. A microchannel was fabricated in PDMS [polydimethylsiloxane] on a silicon wafer using soft lithography (Figure 58a). The width of the microchannel was 94 μm. The channel was filled with 0.005 M bradykinin solution (in deionized water) and the solution was allowed to air dry. Removal of the PDMS left a 94 μm wide stripe of solid bradykinin on the silicon surface. The microchannel here was used to put a physical boundary for the bradykinin deposit. In this way, a pattern was built up.

The spectrum in Figure 58b shows the signal selected by blanker II, 47 - 72 μs after the 8 μs blanker I pulse; the bradykinin singly-charged peak was superimposed on a quasi-continuous background in a mass interval ~ 750 - 1550 Da. This mass window was selected to allow evaluation of the background for ion yield determination. Figure 58c shows the CCD camera image for an acquisition time of 1 minute. An ion image of the bradykinin stripe shape was clearly seen. A plot profile from a line scan over the edge of the channel (Figure 58d) was obtained from ImageJ software. It demonstrates a lateral resolution of about ~3 μm (Zhang, Franzreb, and Williams 2014). Using different lens settings it should be possible to improve spatial resolution to ~ 1 μm at the expense of transmission (Schueler 1992; Schueler 1990).

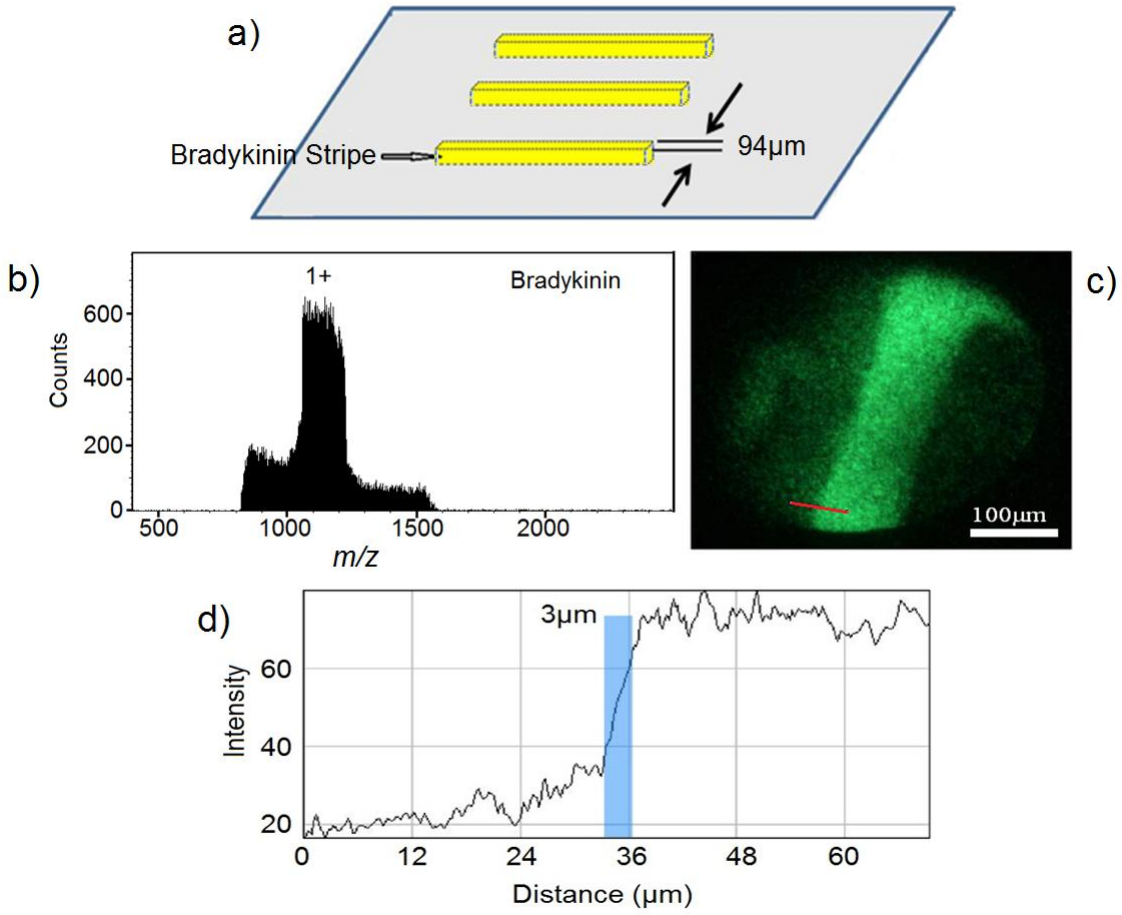

Figure 58. (a): Bradykinin stripes (yellow) formed inside 94 µm width microchannel on silicon; (b): Mass spectrum from bradykinin stripe within blanker II ion window 47 µs - 72 µs after the start of 8 µs blanker I pulse. 1.89 m/z per bin; (c): Ion image of micro-channel for the selected ion window. Line scan position indicated; (d): Line scan across the micro-channel edge, a 3 µm bar was used to estimate the imaging resolution.

5.2 Peptide Mixture Imaging

The peptide mixture sample discussed at Chapter 4 was used to do an imaging test. 25 μmol/L solution was deposited on silicon wafer and vacuum dried. The gold grid was placed on top of the dry peptide deposit and attached at the edges with carbon paint. Blanker I pulse width was 8 μs. Blanker II was used to select the overlapped angiotensin I and substance P ion window. The pattern shown at Figure 59b matched with the gold grid pattern shown at Figure 59c. Please refer to Figure 61 for the detailed explanation of the bright circular feature in Figure 59b.

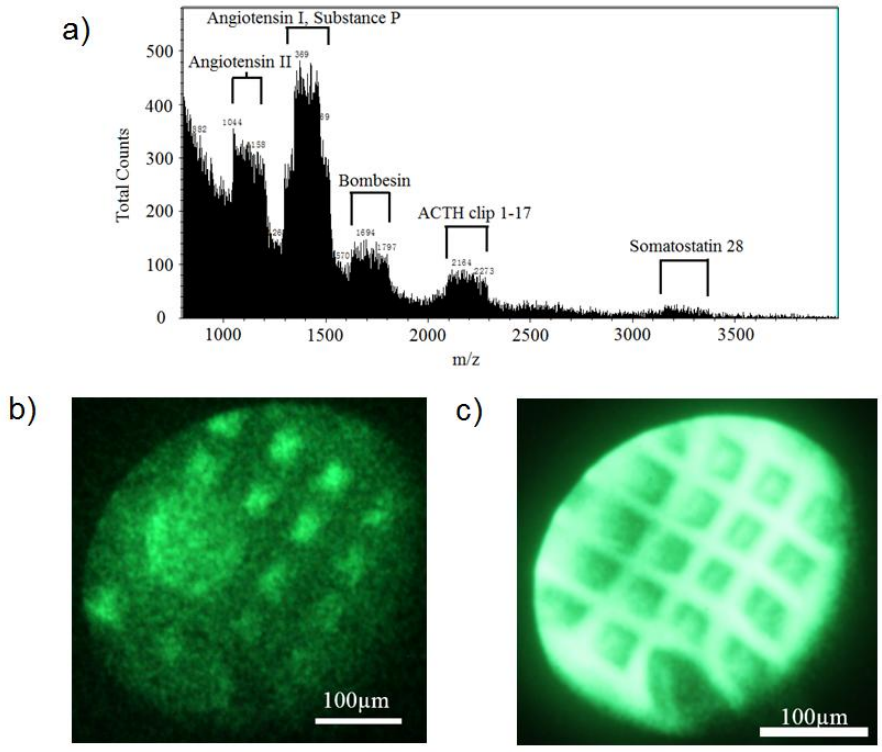

Figure 59.(a):spectrum of peptide mixture (8 μs blanker I pulse width); (b): when the ion window of angiotensin I and substance P was selected, an ion image was obtained; (c):a contrast gold grid ion image was shown with low mass ion window selected.

5.3 Lipid Imaging

A lipid ion image was obtained with L-α-phosphatidylcholine. A clean gold grid was dipped into the L-α-phosphatidylcholine solution. The gold grid was taken out and air dried. A bradykinin layer was deposited on the silicon wafer. The gold grid with L-α-phosphatidylcholine was put on top of the bradykinin layer (Figure 60a). In the imaging process, when the blanker II was used to choose the L-α-phosphatidylcholine peak ion window, the gold grid was bright (Figure 60b). When the blanker II was used to choose the bradykinin ion window (Figure 60c), the tiny spots within the gold grid hole area were bright. Please refer to Figure 61 for the detailed explanation of the bright circular feature in Figure 60b and Figure 60c.

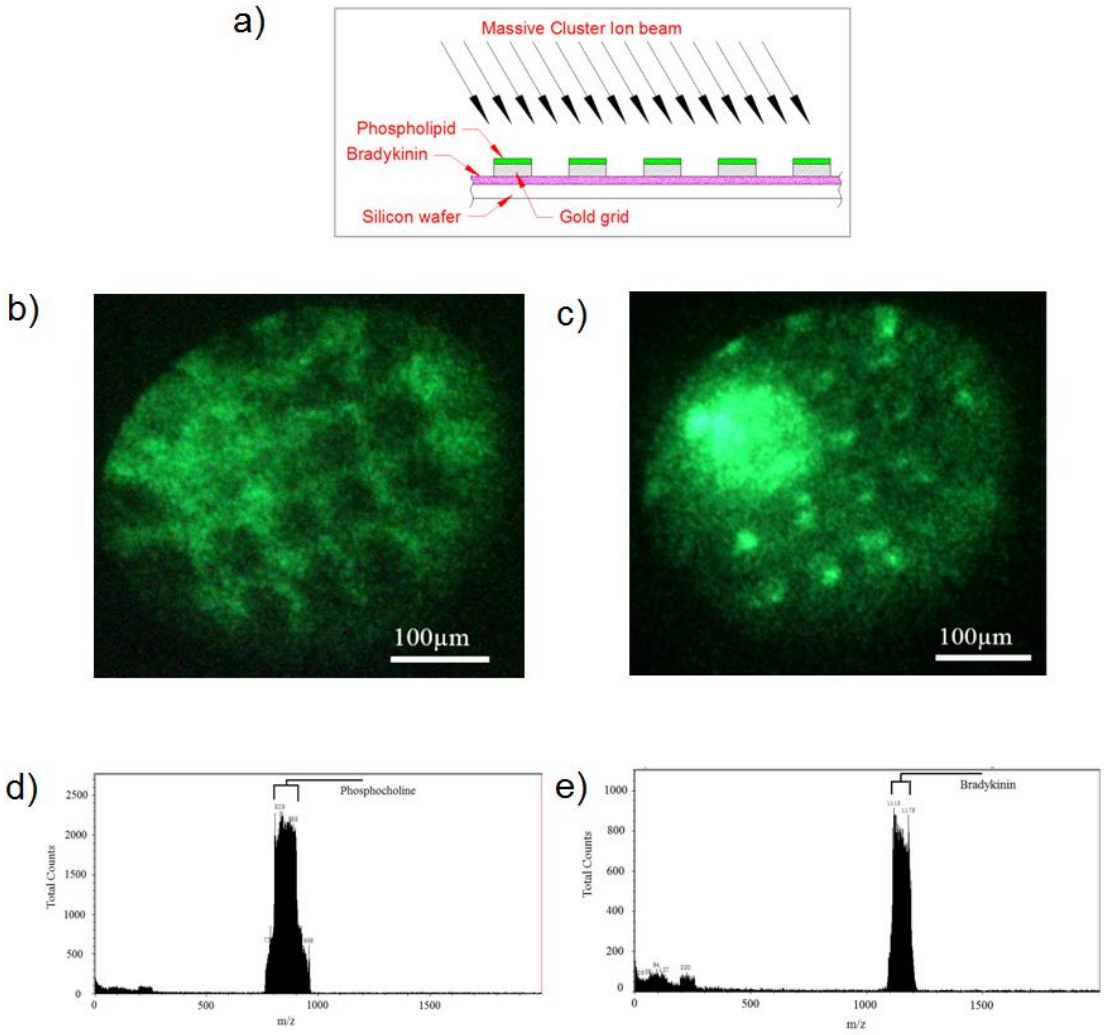

Figure 60. (a):sample preparation for L-α-phosphatidylcholine on grid and bradykinin underneath; (b):ion image when L-α-phosphatidylcholine single charged peak was selected; (c): ion image when bradykinin single charged peak was selected; (d): mass spectrum of L-α-phosphatidylcholine corresponding to ion image in Figure 46b; (e): mass spectrum of bradykinin corresponding to ion image in Figure 60c.

5.4 Protein Imaging

1 μL of 0.03 mol/L insulin solution (in formamide) was deposited on a piece of a flat silicon wafer. A clean gold grid was gently put on top of the wet insulin solution. The capillary action helped in attaching the gold grid closely to the insulin solution. The sample was air dried. Figure 47a shows a mass spectrum of insulin 1+ and 2+ peaks with 15 μs blanker I pulse width. Figure 47b shows a mass spectrum when blanker II was activated (141 μs- 158 μs delay with respect to the start of the blanker I pulse) to select the insulin single charged peak. A significant intensity of low m/z ions were observed even though blanker II was set to select only the insulin singly charged peak. An ion image of insulin (Figure 61c) was obtained corresponding to the mass spectrum in Figure 61b.The image acquisition time was 1 min. A line scan across an insulin bright block demonstrated an imaging resolution of ~3 μm (Figure 61e).

The insulin image has a pronounced bright feature that has also been seen in some other images (Figs. 59, 60). This feature may be associated with the intense flux of low-mass ions that appears to be able to leak through blanker II even though the voltage is 200 V. Figure 61d shows a high resolution mass spectrum with 400 ns blanker I pulse width and with blanker II selected at the same time window as Figure 61b (i.e. to pass insulin 1+). Resolved low m/z ion peaks (H_3O^+, Na^+, K^+) were observed. These were the regular low m/z ions produced at the sample. Based on this, the bright circular artifact in Figure 61c may originate from these low m/z ions leaking through the closed blanker II, perhaps by scattering off the blanker plate.

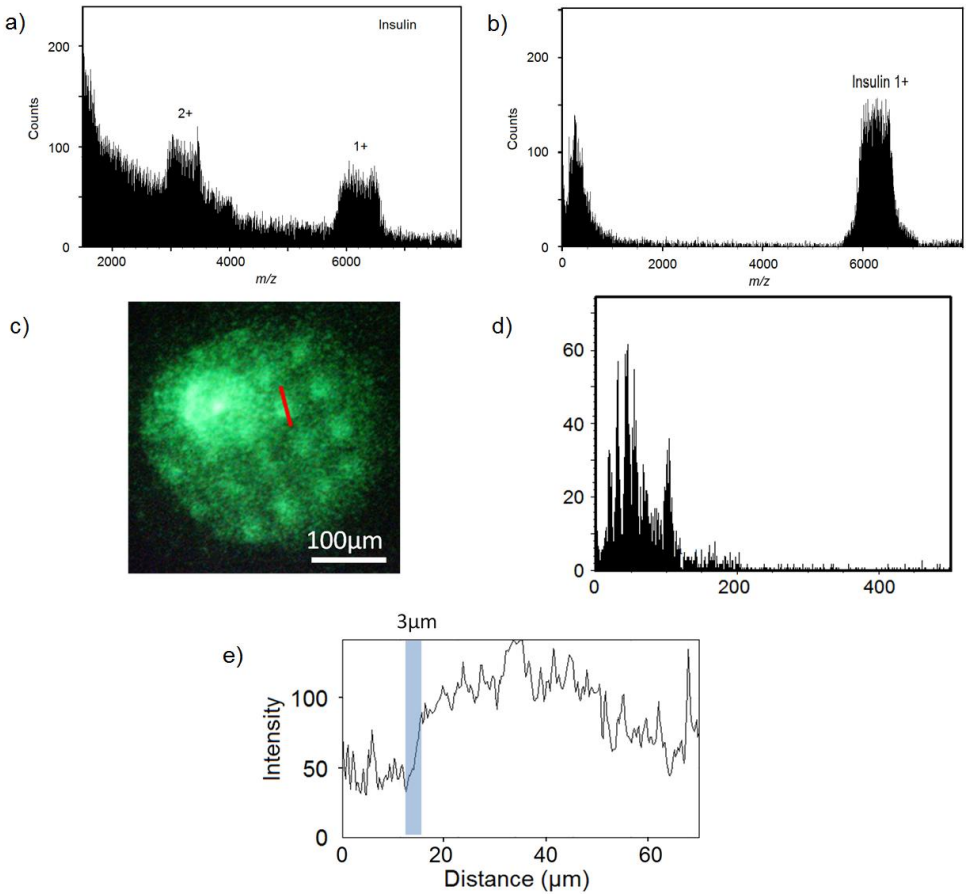

Figure 61. (a): insulin mass spectrum showing 1+ and 2+ peaks (15 µs blanker I pulse width, 6.14 m/z per bin); (b): mass spectrum when only the insulin 1+ peak was selected (blanker II at 141 µs- 158 µs delay with respect to the start of the blanker I pulse, 9.45 m/z per bin), but intense low m/z ions were observed; (c): ion image corresponding to the mass spectrum in Figure 61b, the bright circular artifact may originate from the low m/z ions leaking through blanker II; (d): 400 ns blanker I pulse width high resolution mass spectrum with the same blanker II window selected in Figure 61b showing the resolved peaks (H_2O^+, Na^+, K^+) for the leaking through light ions; (e): plot profile of a line scan (S/N is ~2) through an 70 µm insulin block in Figure 61c demonstrated a spatial resolution of ~3 µm.

CHAPTER 6

USEFUL ION YIELD MEASUREMENTS

In the 4th and 5th chapters, an intact mass range of several kDa and an imaging resolution of ~3 μm have been demonstrated. Another question that remains unknown is whether enough ion counts from a pixel (3×3 μm^2) can be obtained in order to make a meaningful ion image. The concentration of biomolecules in the tissue or cell sample is limited. Useful ion yield (UY) is defined as the ion counts detected divided by the total number of molecules sputtered from the sample. This number determines the number of ion counts which can be obtained with a limited number of sample molecules. This number is important for us to know whether this MCI technology can deal with biomolecules in tissue samples.

One problem with MCI-TRIFT that has been addressed in the previous chapters is the duty cycle. The secondary ions need to be pulsed for time of flight mass analysis. Only a small percentage of secondary ions can enter the secondary column. Most of them are blocked by the blanker I. Duty cycle (also called sampling efficiency) refers to the percentage of secondary ions going through the blanker I.

The duty cycle problem can be eliminated if either the primary cluster ion beam can be pulsed, or the MCI source is coupled with a Cameca xf instrument which can operate with DC primary ion beam and DC secondary ion beam (a future plan). Since we are mostly interested on the optimal performance of the massive cluster ion beam, the useful ion yield numbers measured below were corrected for the duty cycle. These numbers give an idea of how many ion counts can be produced with the massive cluster

impact from a known quantity of sample molecules, regardless of the details of the mass spectrometer.

Experiments have been designed to measure this UY number for a variety of species. The idea is to spot a known amount of sample molecules inside the field of view (FOV). Through counting the molecular ions at the detector, the useful ion yield number can be calculated. The field of view is ~350 μm. A spot size smaller than this must be generated.

6.1 Useful Ion Yield Sample Preparation and Measurements

Bradykinin was dissolved in water to make 0.005 mol/L and 0.0005 mol/L solutions. A fused silica capillary with 150 μm ID and 360 μm was used to make a small spot size. The polyimide layer of the fused silica capillary was burned off to reduce the outer diameter to ~300 μm. The capillary was inserted into a plastic pipette tip and sealed with an alcohol burner. The capillary was first rinsed with the sample solution. The surface tension of water droplets on silicon wafer helped to constrain the spot size. The volume of liquid was calculated through the meniscus change in the capillary (Figure 62a). A spot size of ~175 μm was determined in Figure 62b. Multiple spots were deposited. A spectrum of bradykinin is shown (Figure 62b). At the end of the measurement, all the bradykinin deposit was removed by the MCI beam and no bradykinin peak was visible in the mass spectrum (Figure 62c).

Individual drop sizes (~ 7-9 nL, ~ 0.5 mm length change) could not make a meniscus change that could be accurately measured. Multiple spots were used. The total

deposited volume was obtained from the total length change of the liquid meniscus in the capillary. The total counts obtained from multiple deposits were divided by the total number of molecules deposited to get the useful ion yield. Uncertainty in the total deposited volume measurement is estimated to be ~ 10-15 %.

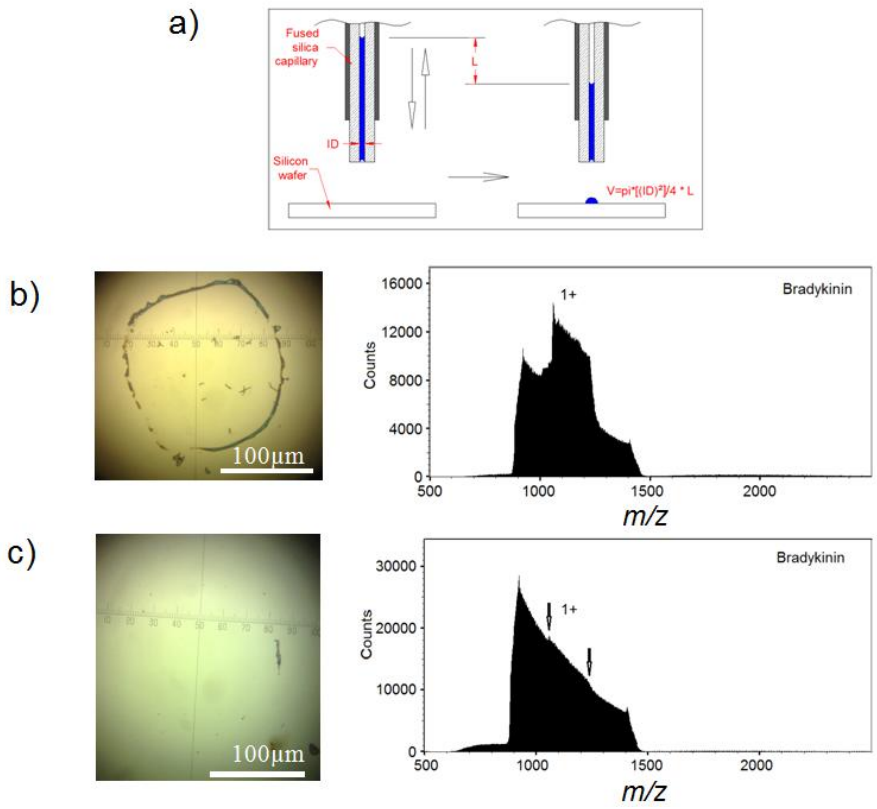

Figure 62.(a): sample preparation of tiny spots on silicon wafer;(b):optical images and mass spectra of bradykinin (~7 nL of 0.0005 mol/L, ~175 µm diameter) spotted on a silicon wafer (1.89 *m/z* per bin, 8 µs blanker I pulse width, CD #1). The mass spectrum was acquired during the first 30 s after switching on the massive cluster beam; (c):the mass spectrum was acquired in the 6 min - 7 min interval after switching on the beam. The optical image was taken after the measurement showing all the bradykinin deposit had been sputtered away.

Six other substances (rhodamine B, bradykinin, angiotensin II, sphingomyelin, L-α-phosphatidylcholine and Insulin) were tested for their useful ion yield with contrast diaphragm #3 (the contrast diaphragm that gave ~3 μm spatial resolution in Chapter 5) and #1.

Sample preparation: Rhodamine B (Sigma Aldrich, St. Louis, MO) was dissolved in deionized water to make a 1.0×10^{-4} M solution. Angiotensin II (Sigma Aldrich, St. Louis, MO) was dissolved in deionized water to make a 5×10^{-4} mol/L solution. L-α-phosphatidylcholine (from egg yolk) (Sigma Aldrich, St. Louis, MO) was dissolved in formamide to make a 1.8×10^{-4} M solution. Sphingomyelin (Avanti Polar Lipids Inc., Alabaster, AL) was first dissolved in 50% methanol/ in formamide solution, and then diluted by formamide to 2.0×10^{-4} M. Bradykinin was dissolved in deionized water to make 0.005 M and 0.0005 M solutions. Insulin (Sigma Aldrich, St. Louis, MO) was dissolved in formamide to make a 5×10^{-5} M solution.

Table 3 lists all the measurement parameters (blanker I pulse width, cycle period length, Blanker I transmission time, effective pulse width and duty cycle) for these compounds. Typical duty cycle ranged from 0.66%~4.8%. Since the compounds used in useful ion yield measurements were pure compounds, it was not necessary to have a high mass resolution. Blanker I pulse widths listed in Table 3 typically are 2-4 times bigger than the transmission time. A bigger blanker I pulse width lets more secondary ions go into the detector.

Table 3: Summary of experimental parameters (blanker I pulse width, cycle length, transmission time, effective pulse width and duty cycle) for rhodamine B, Irganox 1010, angiotensin II, bradykinin, sphingomyelin, L-α-phosphatidylcholine and Insulin. Duty cycle was calculated as the effective pulse width divided by the cycle length.

Substance	Molecular Weight	Blanker I pulse width(μs)	One cycle length (μs)	Blanker I Transmission Time (μs)	Effective Pulse Width (μs)	Duty Cycle (%)
Rhodamine B (without Cl-)	443.5 Da	2	97	1.36	0.63	0.66
Irganox 1010	1178 Da	6	138	2.1	3.9	2.8
Angiotensin II	1046 Da	8	138	2.1	5.9	4.3
Bradykinin	1060 Da	8	138	2.2	5.8	4.2
Sphingomyelin	731 Da	4	138	1.76	2.24	1.6
Sphingomyelin Dimer 1+		4	138	2.49	1.51	1.1
L-α-phosphatidylcholine	758 Da	4	138	1.79	2.21	1.6
Insulin (1+)	5808 Da	15	242	4.9	10.1	4.2
Insulin (2+)		15	242	3.5	11.5	4.8

Table 4: Summary of useful ion yield for rhodamine B, angiotensin II, bradykinin, sphingomyelin, L-α-phosphatidylcholine, Insulin 1^+ and 2^+ for two different contrast diaphragm sizes (CD1 and CD3). Numbers marked as * represent the useful ion yield obtained when the capillary was near the end of its lifetime.

Substance	Nominal Mass	Useful Ion Yield ($\times 10^{-5}$) with sampling efficiency corrected	
		Contrast Diaphragm #1 (Diameter: 2.1 mm)	Contrast Diaphragm #3 (Diameter: 0.21 mm)
Rhodamine B (without Cl-)	443.5 Da	20; 16	9.8
Irganox 1010	1178 Da	2.7	N/A
Angiotensin II	1046 Da	N/A	1.8
Bradykinin	1060 Da	2.8; 2.5; 3.9	2.3; 1.9
Sphingomyelin	731 Da	2.9	1.3
Sphingomyelin dimer 1+		0.32	0.33
L-α-phosphatidylcholine	758 Da	2.7; 2.2; 1.3*	1.4; 1.2*
Insulin (1+)	5808 Da	1.1; 1.1; 0.70	0.14
Insulin (2+)		0.91; 0.80; 0.35	0.010

Table 4 summarizes the useful ion yields of rhodamine B, irganox 1010, angiotensin II, bradykinin, sphingomyelin, sphingomyelin dimer 1+, L-α-phosphatidylcholine, insulin1+ and insulin 2+.

The useful ion yield numbers in table 4 have been corrected for the duty cycle. They do not reflect the useful ion yield that can be obtained in this MCI-TRIFT instrument (continuous primary ion beam and pulsed secondary ion beam). They do represent the useful ion yield that could be achieved when either the primary ion beam is pulsed or the secondary ion beam is continuous in imaging.

The useful ion yield of rhodamine B was larger compared with other compounds because rhodamine B (without Cl^-) is a pre-formed ion with a quaternary ammonium center. The useful ion yield of insulin is at 10^{-6} range. With higher molecular weight, it has smaller detection efficiency and maybe more vulnerable to fragmentation.

The useful ion yields for other compounds (peptides, lipids, organic molecules) are in the $1\text{-}3\times10^{-5}$ range. What do these useful ion yield numbers mean? For example, the $3\times3\ \mu m^2$ cell membrane area of a lipid bilayer has 2.6×10^7 lipid molecules (Nagle and Tristram-Nagle 2000). Phosphatidylcholine (PC), phosphatidylethanolamine (PE) and sphingomyelin (Sph) constitute ~40%, ~20% and ~10% in eukaryotic plasma membrane lipids (OPM database, University of Michigan). A useful ion yield of 1×10^{-5} and 10% lipid component can give ~26 counts/pixel. The statistical S/N is ~5 which is enough to make a useful ion image. If we have unit mass resolution for imaging, for lipids at 700-800 Da, the ^{12}Cpeak is only 60% of the total. But still we can get ~16 counts/pixel under the same assumption, the statistical S/N is ~4 which still can produce a useful ion image.

Typically, a capillary can only be used for 2-3 weeks before replacement. In a dead capillary, the capillary inner space has been blocked by crystals from solution. Different stages of the capillary had different flow rate. According to the experiment done by Stimpson and Evans (1978), smaller flow rates resulted in more low mass/charge ions, thus heavier damage to the sample materials. A comparison between a fresh new capillary and a capillary being used for two weeks was done for the L-α-phosphatidylcholine. The number marked as * refers to the useful ion yield when the capillary was near the end of its lifetime. The difference of UY was within a factor of 2.

There are several contrast diaphragm (CD) sizes available in the TRIFT. The purpose of the CD is to limit the initial angular and energy distribution of the secondary ions coming out of the sample surface. The influence of the CD size on the useful ion yield has been investigated between CD1 (2.1 mm diameter) and CD3 (0.21 mm). The area of the CD aperture decreases 100 times from CD1 to CD3. But the factor of useful ion yield drops is much smaller, about a factor of ~2 for lipids and peptides and ~7 for insulin. This indicates that the beam crossover is not much bigger than the CD3 diameter.

Useful ion yield is an important parameter determining whether an imaging resolution is meaningful. But up to now, there is not much research on the useful ion yield for MALDI or DESI.

Vickerman and colleagues et al. have estimated useful ion yield for 10keV Ar_{1000}^{+} and $H_2O_{1000}^{+}$ ion beams on angiotensin II deposits. From 1 $\mu m^2 \times 10$ nm volume, they estimated that 1 ion count and 6 ion counts could be obtained for 10keV Ar_{1000}^{+} and $H_2O_{1000}^{+}$ ion beam. The authors used a sputter yield number from C_{60} sputtering on a sugar

sample (Cheng, Wucher, and Winograd 2006). Taking their assumption that a 1 μm^2 ×10 nm volume of angiotensin II has 10^7 molecules, in our case, the total counts of angiotensin II molecular ions (with duty cycle corrected) would be ~180 counts. There is a significant improvement on the useful ion yield for massive cluster ions compared with Ar_{1000}^+ and $H_2O_{1000}^+$ ions.

Gebhardt et al. used a neutral SO_2 clusters beam generated from supersonic expansion to desorb and ionize sample molecules (Gebhardt et al. 2009). An ionization probability test was done (Lee et al. 2013). Since the primary beam is a neutral beam, the sample stage current can be used to monitor the secondary ions leaving the sample surface. The author assumed that all the charge desorbed was attributed to the biomolecules (angiotensin II). In this way they got a useful ion yield of 10^{-2}~10^{-3}. If we assume a 10% overall transmission and detection efficiency in our case, their useful ion yield number is about 1-2 orders of magnitude greater than ours. It would be good if they can measure the useful ion yield from the ion counts of a mass resolved peak in the future.

6.2 Sputter Rate Measurement.

A sputter rate measurement was done to estimate how fast the MCI beam can sputter the sample. An organic delta layer sample (Irganox 1010, Irganox 3114) was donated by Dr. Ian Gilmore at NPL. This sample was constituted by two 47.5 nm and three 95 nm thickness irganox 1010 layers interspersed with four 2.5 nm layers of irganox 3114 (Figure 63). By measuring the time needed to sputter through this 390 nm thick delta layer sample, the sputter rate can be calculated.

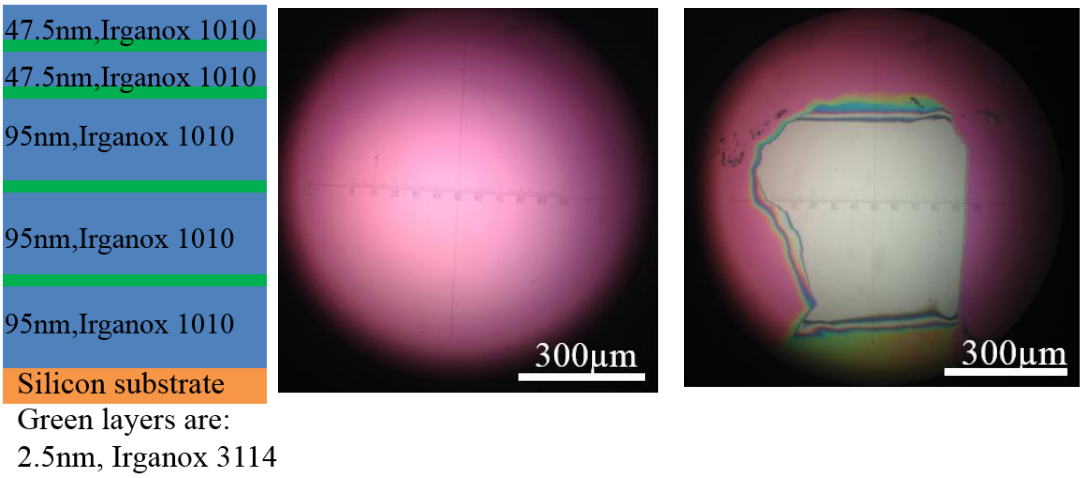

Figure 63: Structure of the irganox delta layer sample (left). Optical image of the sample before the measurement showing the interference color (middle). An aluminum foil with a hole was put on the sample to limit the area being sputtered. Optical image of the sample after the measurement (right) showing that the open irganox area had been completely sputtered away by the massive cluster ion beam. The color transitions at three edges of the cleaned area indicated an angle of the primary ion beam sputtering the sample surface.

When the source voltage was at -10 kV, the whole process took 40 min corresponding to a sputter rate of ~10 nm/min. When the source voltage was improved to -12 kV, the whole process took 18 min corresponding to ~20 nm/min. The reason for the sputter rate increase probably was due to the increasing primary cluster ion beam current, or the cluster distribution change. Since the sample stage current cannot be monitored, it was not clear which factor contributed to the sputter rate change.

In microprobe ion imaging mode, the primary current is limited by the resolution required. Higher current will defocus the primary ion beam making the resolution poorer.

But this problem does not exist in microscope ion imaging mode since the imaging resolution is determined by the secondary ion optics. Thus significantly higher sputter rates can be used in the MCI-TRIFT. A fast measurement can be crucial in some applications, e.g. clinical application.

6.3 Preliminary Tests on Cell Lipids with MCI-TRIFT

Three types of breast cell lines were used: (1), MCF 10A, a breast non-cancer cell line; (2), MDA-MD-468, a breast cancer cell line; (3), MDA-MB-231, another type of breast cancer cell line. The sample preparation was the same for these three types of cells. Here are the detailed steps (provided by Seron Eaton, Biodesign Institute, Arizona State University): (1). Cells were grown through log phase to ~80% confluency for experimental collection; (2). Cells were washed 2 times with PBS; (3). Trypsin was added to strip cells from the dish wall and cells were incubated at 37^{o}C for 10-20 minutes; (4). Growth media was added to neutralize trypsin; (5). Cells number were counted; (6). Necessary amount of cells were aliquoted for the experiment. A density of 13.3×10^{6} cells/ml (for 40,000 cells in 3 µl) was needed. A solution of 60 µl of cells for spotting was made. 8×10^{5} cells were pipetted into a 1.5 ml Eppendorf tube; (7). The cell solution was centrifuged at 550 g for 5 minutes to pellet cells; (8). Supernatant was aspirated and 0.5 ml of PBS was added to wash the cells; (9). The cells were centrifuged again and supernatant was aspirated; (10). Cell pellet was resuspended in 60 µl of PBS; (11). Cells were spotted onto prepared slides with 3 µl spots with 40,000 cells/spot; (12). Spots were allowed to dry and ready for analysis.

Multiple spectra of each cell sample were taken. A typical spectrum of each sample was chosen for comparison (Figure 64).

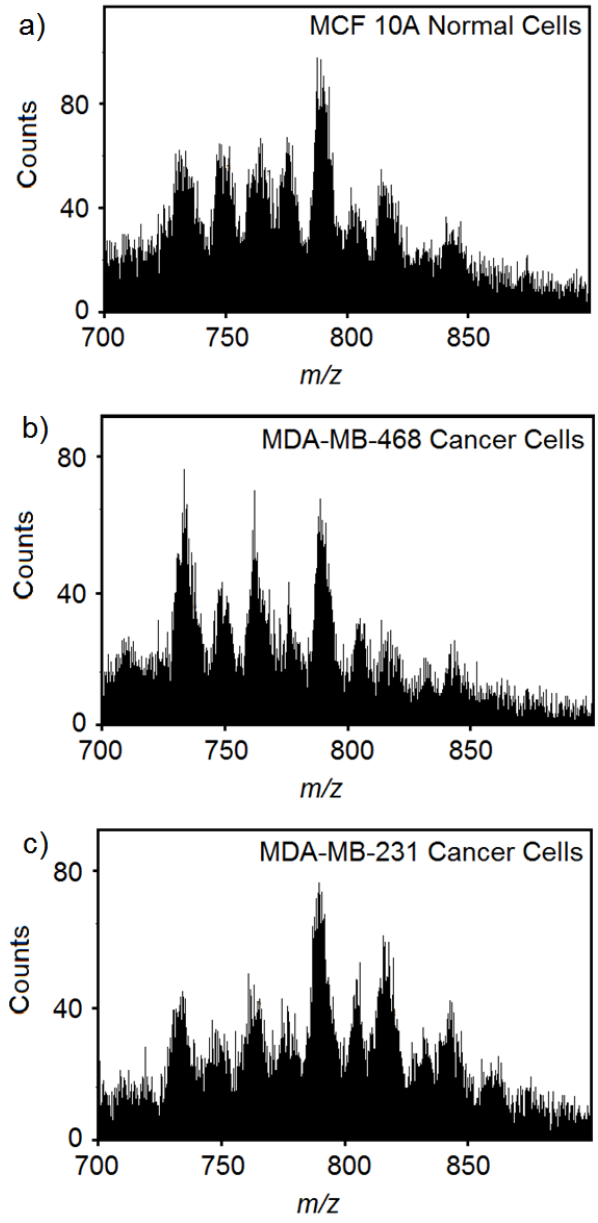

Figure 64. Lipid patterns of (a) MCF 10A (a normal breast cell line), (b) MDA-MB-468 (a breast cancer cell line), (c) MDA-MB-231 (another type of breast cancer cell line). 2 μs blanker I pulse width.

All the mass spectra for each sample were put together in Figure 65 to show the reproducibility of the patterns.

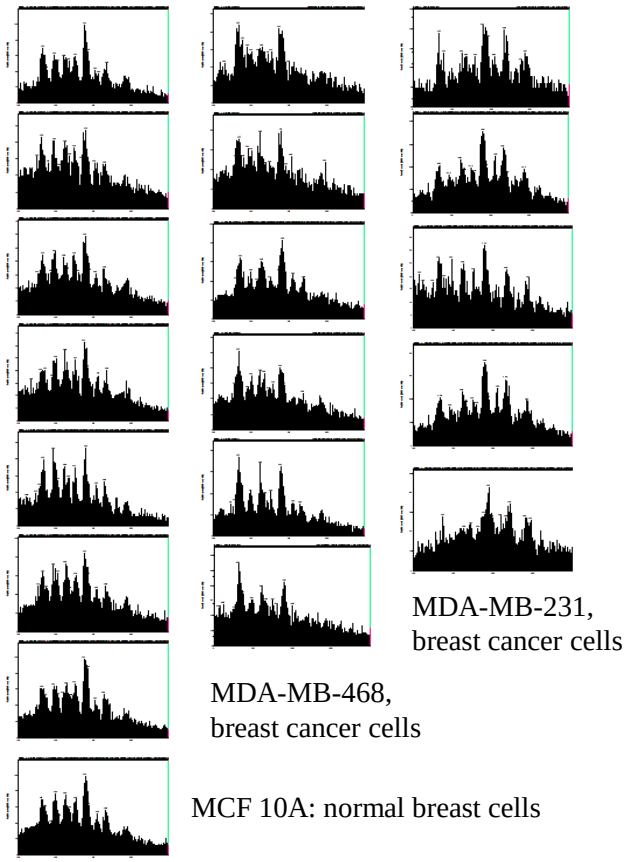

Figure 65. All the mass spectra obtained for three different types of cells. The mass range displayed in all the spectra was the same, 700-900 Da. 2 μs Blanker I pulse width. The relative peak intensity patterns were different between these three cell lines.

In Figure 65, the differences in the peak patterns between the normal cell line and the cancer cell lines can be observed. Furthermore, the ion counts number for different lipid domains (m/z 728, 744, 759, 772, 786, 801, 812, 838) were recorded to do quantitative calculation. Each domain could contain multiple lipid peaks. Since the mass resolving power is not enough in this MCI-TRIFT, each lipid domain was treated as a

lipid peak for imaging. The identity of each lipid peak cannot be identified currently. The peak assignments for MDA-MB-231 can refer to table 1 reported by Chughtai et al. (Chughtai et al. 2013). Future improvement on the instrument is required in order to resolve single lipid peaks. For each spectrum, the ion counts number for m/z 786 was set as 100%, the relative intensity of other lipid domains were referred to this m/z. The relative intensity for each lipid domain was plotted at Figure 66. The error bar is the standard deviation of the mean multiplied by student factor at 95% confidence. Different expression intensity was observed between the cancer cells and normal cells at lipid domains at m/z 728 and 812.

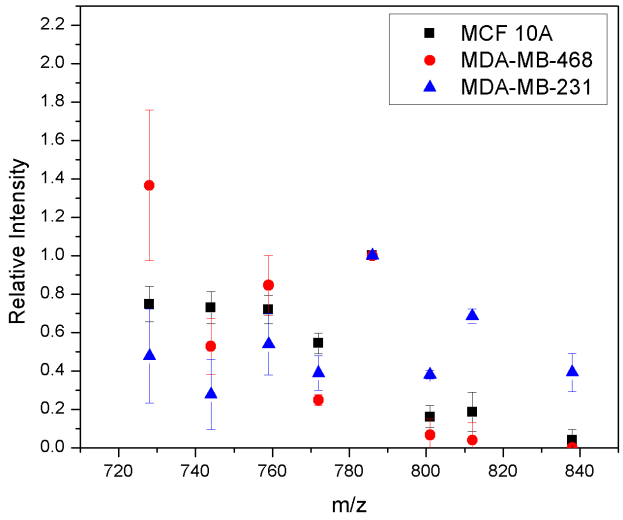

Figure 66: The relative intensity for the normal breast cells and two types of breast cancer cells for eight different lipid domains (m/z 728, 744, 759, 772, 786, 801, 812, 838). The ion counts number for m/z 786 was set as 100%, the relative intensity of other lipid domains were normalized to this m/z. The error bar is the standard deviation of the mean multiplied by student factor at 95% confidence. Different expressions have been observed between the cancer cells and normal cells at lipid domains of m/z 728 and 812.

6.4 MCI-Cameca xf

The useful ion yield numbers reported above have been corrected by the duty cycle. The duty cycle is ~0.1% for lipid samples in Figure 54, 55. With the current MCI-TRIFT instrument, only 0.3 count/pixel can be obtained from a cell assuming the cell membrane is constituted by a single 100% lipid content. This cannot generate a usable ion image. How can we eliminate the duty cycle issue? One straightforward method is to pulse the primary cluster ion beam. This is feasible, but it will reduce the primary cluster ion beam current at the target. This will prolong the measurement time which may not be acceptable in clinical application. Another idea is to couple the MCI source to a Cameca xf instrument (Figure 67). It also has ion microscope imaging capability. The mass analyzer is the magnetic sector. It can do ion microscope imaging with a few μm resolution. A DC primary cluster ion beam and a DC secondary ion beam can be used. The mass range for the current instrument is ~300 Da. With the sample stage voltage decreased from 10 kV to 3 kV (similar to TRIFT's sample voltage), the mass range can go up to 1 kDa which is sufficient for lipid imaging. Better mass resolution is achievable ~1000 (Peaks with more than 1Da difference can be resolved). This may be an ideal mass spectrometer for imaging with the glycerol massive cluster ion source.

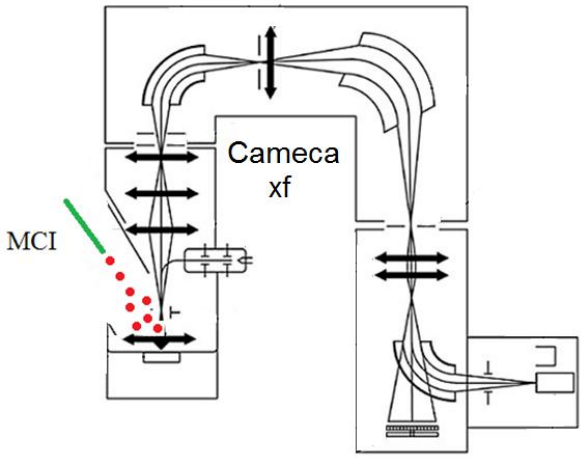

Figure 67. The MCI source is coupled to Cameca xf instrument. Magnetic sector is used as mass analyzer. DC primary ion beam and DC secondary ion beam can be achieved without the duty cycle issue. Ion microscope imaging with a few μm and higher mass resolving power (lipid peaks with more than 1 Da mass difference can be resolved) are available.

6.5 Optimization of MCI Useful Ion Yield

In Figure 23, Stimpson et al. demonstrated a huge initial glycerol molecular ions emission (90% of the particle flux is low m/z ions). This light component damages the sample molecules at the surface and underneath. Lower temperature and flow rate can increase the percentage of this molecular ion emission. In order to improve the useful ion yield, we need to improve the percentage of heavier cluster ions (by improving the temperature at the capillary) and filter the low mass/charge ions. It should be noted that the glycerol cluster ion distribution might be different in our system compared to Stimpson's. Ammonium acetate was used instead of the NaI. The capillary diameter is

also different. But Fujiwara has seen a similar low mass component with electrosprayed ionic liquid (Fujiwara et al. 2011).

There are multiple ways to filter the low m/z ions. First idea is to use two blankers in series. The first blanker can pulse the cluster ion beam to let a tiny pulse width through. At an appropriate distance away, the second blanker can choose the mass/charge window we want to go to the sample surface.

A selective cluster ion gun was designed and made. The scheme and optical image are shown below (Figure. 68, 69). There is an immersion lens in front of the capillary. It is used to focus the diverging cluster ion beam to improve the current at the sample stage. A steerer plate was designed after the immersion lens to deflect an off-axis beam back to the central axis. The first blanker (blanker III) is located after the steerer plate. The second blanker plate (blanker IV) is 18cm away from the first blanker. Both of these two blankers are operated with a 200V pulse. The time delay between the two blankers determines the mass/charge ion window going through.

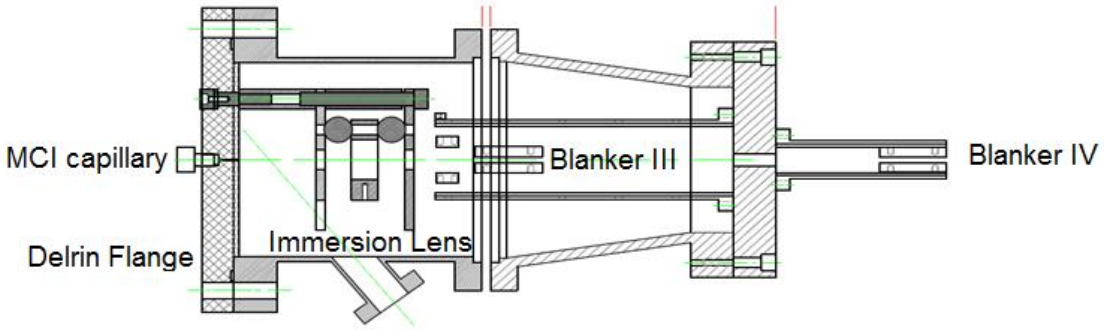

Figure 68: Scheme of a selective cluster ion gun. Two blankers (blanker III, IV) together can pulse the primary ion beam and select a mass/charge ion window going through.

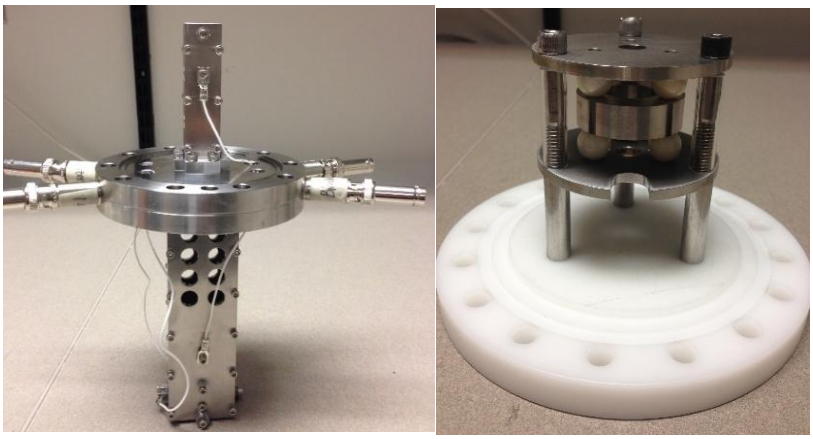

Figure 69. Images of the selective cluster ion gun. The whole assembly (left) with first blanker at the bottom, second blanker at the top and four BNC cables to supply voltages to steerer plates and two blankers. MCI source and immersion lens (right). The middle electrode in immersion lens is applied with a negative 6~7 kV.

Another idea is to use magnetic deflection. Different mass/charge ions have different trajectories in a magnetic field. With an aperture at the exit of the magnetic field, certain m/z ions window can be selected or low m/z species can be rejected.

CHAPTER 7

CONCLUSIONS

In this thesis, a new imaging mass spectrometry technique was introduced. A massive cluster primary ion source was coupled to a time of flight ion microscope imaging mass spectrometer (TRIFT). The ion microscope imaging capability of the TRIFT does not require the primary MCI ion source to be focused which is difficult to do. The key parameters for an imaging mass spectrometry technology have been studied, e.g. intact mass range, imaging resolution and useful ion yield.

A spatial resolution of ~3 μm, which is sufficient for sub-cellular imaging, has been demonstrated. Intact mass range of sputtering and ionizing molecules can go up to several kDa (up to lysozyme so far). This intact mass range can cover lipids, peptides and small proteins. The useful ion yields of lipids, peptides are within ~1-2 $\times 10^{-5}$. A 3×3 μm^2 pure lipid bilayer can produce 260 counts/pixel with a 1×10^{-5} useful ion yield. This count number is enough to produce a useful ion image. Sputter rate was 20 nm/min when the source voltage was at -12kV. There is more space to improve the sputter rate without degrading the spatial resolution. Fast measurement, typical spectrum/image acquisition time ranges from a few seconds to minutes. This may be crucial in clinical application where fast measurements are required. The MCI source is cheap and easy to build.

REFERENCES

Abraham, Jerrold L., Subhash Chandra, Charu Thakral, and Joshua M. Abraham. 2008. 'SIMS imaging of gadolinium isotopes in tissue from Nephrogenic Systemic Fibrosis patients: Release of free Gd from magnetic resonance imaging (MRI) contrast agents', *Applied Surface Science*, 255: 1181-84.

Aksyonov, S. A., and P. Williams. 2001. 'Impact desolvation of electrosprayed microdroplets - a new ionization method for mass spectrometry of large biomolecules', *Rapid Communications in Mass Spectrometry*, 15: 2001-06.

Asakawa, Daiki, Susumu Fujimaki, Yutaka Hashimoto, Kunihiko Mori, and Kenzo Hiraoka. 2007. 'Study on ion formation in electrospray droplet impact secondary ion mass spectrometry', *Rapid Communications in Mass Spectrometry*, 21: 1579-86.

Asakawa, Daiki, Kentaro Yoshimura, Sen Takeda, and Kenzo Hiraoka. 2010. 'Direct analysis of lipids in mouse brain using electrospray droplet impact/SIMS', *Journal of Mass Spectrometry*, 45: 437-43.

Asakawa, Daiki, and Kenzo Hiraoka. 2011. 'Detection of peptides in high concentration of salts by electrospray droplet impact/secondary ion mass spectrometry', *Surface and Interface Analysis*, 43: 1341-45.

Asakawa, Daiki, and Kenzo Hiraoka. 2011. 'Study of the desorption/ionization mechanism in electrospray droplet impact secondary ion mass spectrometry', *Rapid Communications in Mass Spectrometry*, 25: 655-60.

Badro, James, Frederick J. Ryerson, Peter K. Weber, Angele Ricolleau, Stewart J. Fallon, and Ian D. Hutcheon. 2007. 'Chemical imaging with NanoSIMS: A window into deep-Earth geochemistry', *Earth and Planetary Science Letters*, 262: 543-51.

Caprioli, Richard M. 2015. 'Imaging Mass Spectrometry: Enabling a New Age of Discovery in Biology and Medicine Through Molecular Microscopy', *Journal of the American Society for Mass Spectrometry*, 26: 850-52.

Castaing, R., and G. Slodzian. 1961. 'Microanalysis by secondary ionic emission', *A. L. Houwink, and B. J. Spit, Editors. The Proceedings of the European Regional Conference on Electron Microscopy*: 169-72.

Chandra, Subhash, Rolf F. Barth, Syed A. Haider, Weilian Yang, Tianyao Huo, Aarif L. Shaikh, and George W. Kabalka. 2013. 'Biodistribution and Subcellular Localization of an Unnatural Boron-Containing Amino Acid (Cis-ABCPC) by Imaging Secondary Ion Mass Spectrometry for Neutron Capture Therapy of Melanomas and Gliomas', *Plos One*, 8.

Chaurand, Pierre, Joey C. Latham, Kirk B. Lane, James A. Mobley, Vasiliy V. Polosukhin, Pamela S. Wirth, Lillian B. Nanney, and Richard M. Caprioli. 2008. 'Imaging mass spectrometry of intact proteins from alcohol-preserved tissue specimens: Bypassing formalin fixation', *Journal of Proteome Research*, 7: 3543-55.

Chaurand, P., S. A. Schwartz, and R. M. Caprioli. 2004. 'Profiling and imaging proteins in tissue sections by MS', *Anal Chem*, 76: 86A-93A.

Cheng, J., A. Wucher, and N. Winograd. 2006. 'Molecular depth profiling with cluster ion beams', *Journal of Physical Chemistry B*, 110: 8329-36.

Chou, Chau-Wen, Randall W. Nelson, and Peter Williams. 2009. 'Dependence of the ejection velocities of laser-ablated ions on the Laser wavelength and fluence', *European Journal of Mass Spectrometry*, 15: 305-14.

Chughtai, Kamila, Lu Jiang, Tiffany R. Greenwood, Kristine Glunde, and Ron M. A. Heeren. 2013. 'Mass spectrometry images acylcarnitines, phosphatidylcholines, and sphingomyelin in MDA-MB-231 breast tumor models', *Journal of Lipid Research*, 54: 333-44.

Cillero-Pastor, Berta, Gert B. Eijkel, Andras Kiss, Francisco J. Blanco, and Ron M. A. Heeren. 2013. 'Matrix-assisted laser desorption ionizationimaging mass spectrometry: A new methodology to study human osteoarthritic cartilage', *Arthritis and Rheumatism*, 65: 710-20.

Claude Lechene, Francois Hillion, Greg McMahon, Douglas Benson,, J Patrick Kampf Alan M Kleinfeld, Daniel Distel, Yvette Luyten, Joseph, Dirk Hentschel Bonventre, Kwon Moo Park, Susumu Ito, Martin, and Gilles Benichou and Georges Slodzian Schwartz. 2006. 'High-resolution quantitative imaging of mammalian and bacterial cells using stable isotope mass spectrometry', *Journal of Biology*, 5: 30.

Cornett, D. S., T. D. Lee, and J. F. Mahoney. 1994. 'MATRIX-FREE DESORPTION OF BIOMOLECULES USING MASSIVE CLUSTER-IMPACT', *Rapid Communications in Mass Spectrometry*, 8: 996-1000.

Cremer, C., and T. Cremer. 1978. 'CONSIDERATIONS ON A LASER-SCANNING-MICROSCOPE WITH HIGH-RESOLUTION AND DEPTH OF FIELD', *Microscopica Acta*, 81: 31-44.

Dill, Allison L., Livia S. Eberlin, Demian R. Ifa, and R. Graham Cooks. 2011. 'Perspectives in imaging using mass spectrometry', *Chemical Communications*, 47: 2741-46.

Eberlin, Livia S., Christina R. Ferreira, Allison L. Dill, Demian R. Ifa, and R. Graham Cooks. 2011. 'Desorption electrospray ionization mass spectrometry for lipid characterization and biological tissue imaging', *Biochimica Et Biophysica Acta-Molecular and Cell Biology of Lipids*, 1811: 946-60.

Eberlin, Livia S., Xiaohui Liu, Christina R. Ferreira, Sandro Santagata, Nathalie Y. R. Agar, and R. Graham Cooks. 2011. 'Desorption Electrospray Ionization then MALDI Mass Spectrometry Imaging of Lipid and Protein Distributions in Single Tissue Sections', *Anal Chem*, 83: 8366-71.

Eberlin, Livia S., Isaiah Norton, Allison L. Dill, Alexandra J. Golby, Keith L. Ligon, Sandro Santagata, R. Graham Cooks, and Nathalie Y. R. Agar. 2012. 'Classifying Human Brain Tumors by Lipid Imaging with Mass Spectrometry', *Cancer Research*, 72: 645-54.

Ellis, Shane R., Chunping Wu, Jane M. Deeley, Xiangjia Zhu, Roger J. W. Truscott, Marc In Het Panhuis, R. Graham Cooks, Todd W. Mitchell, and Stephen J. Blanksby. 2010. 'Imaging of Human Lens Lipids by Desorption Electrospray Ionization Mass Spectrometry', *Journal of the American Society for Mass Spectrometry*, 21: 2095-104.

Erni, Rolf, Marta D. Rossell, Christian Kisielowski, and Ulrich Dahmen. 2009. 'Atomic-Resolution Imaging with a Sub-50-pm Electron Probe', *Physical Review Letters*, 102.

Faulk, W.; Taylor, G. 1971. 'An immunocolloid method for the electron microscope', *Immunochemistry*, 8: 3.

Floss, C., F. J. Stadermann, J. P. Bradley, Z. R. Dai, S. Bajt, G. Graham, and A. S. Lea. 2006. 'Identification of isotopically primitive interplanetary dust particles: A NanoSIMS isotopic imaging study', *Geochimica Et Cosmochimica Acta*, 70: 2371-99.

Frisz, Jessica F., Haley A. Klitzing, Kaiyan Lou, Ian D. Hutcheon, Peter K. Weber, Joshua Zimmerberg, and Mary L. Kraft. 2013. 'Sphingolipid Domains in the Plasma Membranes of Fibroblasts Are Not Enriched with Cholesterol', *Journal of Biological Chemistry*, 288: 16855-61.

Fujiwara, Yukio, Naoaki Saito, Hidehiko Nonaka, Taisuke Nakanaga, and Shingo Ichimura. 2010. 'A new cluster-ion-beam source for secondary ion mass spectrometry (SIMS) using the electrospray of a pure ionic liquid under high vacuum', *Nuclear Instruments & Methods in Physics Research Section B-Beam Interactions with Materials and Atoms*, 268: 1938-41.

Fujiwara, Yukio, Naoaki Saito, Hidehiko Nonaka, Taisuke Nakanaga, and Shingo Ichimura. 2011. 'Characteristics of a charged-droplet beam generated by vacuum electrospray of an ionic liquid', *Chemical Physics Letters*, 501: 335-39.

Gebhardt, Christoph R., Anna Tomsic, Hartmut Schroeder, Michael Duerr, and Karl L. Kompa. 2009. 'Matrix-Free Formation of Gas-Phase Biomolecular Ions by Soft Cluster-Induced Desorption', *Angewandte Chemie-International Edition*, 48: 4162-65.

Ghiran, Ionita C. 2011. 'Introduction to Fluorescence Microscopy', *Light Microscopy: Methods and Protocols*, 689: 93-136.

Girod, Marion, Yunzhou Shi, Ji-Xin Cheng, and R. Graham Cooks. 2010. 'Desorption Electrospray Ionization Imaging Mass Spectrometry of Lipids in Rat Spinal Cord', *Journal of the American Society for Mass Spectrometry*, 21: 1177-89.

Guo, Shuai, Yanmin Wang, Dan Zhou, and Zhili Li. 2014. 'Significantly increased monounsaturated lipids relative to polyunsaturated lipids in six types of cancer microenvironment are observed by mass spectrometry imaging', *Scientific Reports*, 4.

Hiraoka, K., D. Asakawa, S. Fujimaki, A. Takamizawa, and K. Mori. 2006. 'Electrosprayed droplet impact/secondary ion mass spectrometry', *European Physical Journal D*, 38: 225-29.

Hiraoka, Kenzo, Daiki Asakawa, and Rio Takaishi. 2013. 'Estimation of useful yields for electrospray droplet impact/secondary ion mass spectrometry (EDI/SIMS)', *Surface and Interface Analysis*, 45: 968-72.

Hiraoka, Kenzo, Kunihiko Mori, and Daiki Asakawa. 2006. 'Fundamental aspects of electrospray droplet impact/SIMS', *Journal of Mass Spectrometry*, 41: 894-902.

Huang, Wei, Jens C. Eickhoff, Farideh Mehraein-Ghomi, Dawn R. Church, George Wilding, and Hirak S. Basu. 2015. 'Expression of spermidine/spermine N-1-acetyl transferase (SSAT) in human prostate tissues is related to prostate cancer progression and metastasis', *Prostate*, 75: 1150-59.

Jungmann, Julia H., Luke MacAleese, Jan Visser, Marc J. J. Vrakking, and Ron M. A. Heeren. 2011. 'High Dynamic Range Bio-Molecular Ion Microscopy with the Timepix Detector', *Anal Chem*, 83: 7888-94.

Kachan, M., J. Hunter, D. Kouzminov, A. Pivovarov, J. Gu, F. Stevie, and D. Griffis. 2004. 'O-2(+) versus Cs+ for high depth resolution depth profiling of III-V nitride-based semiconductor devices', *Applied Surface Science*, 231: 684-87.

Kapuscinski, J. 1995. 'DAPI - A DNA-SPECIFIC FLUORESCENT-PROBE', *Biotechnic & Histochemistry*, 70: 220-33.

Kawamura, A. Jr. 1969. 'FLUORESCENT ANTIBODY TECHNIQUES AND THEIR APPLICATIONS BOOK', *Fluorescent Antibody Techniques and Their Applications Book*: 203-03.

Kiss, Andras, Donald F. Smith, Julia H. Jungmann, and Ron M. A. Heeren. 2013. 'Cluster secondary ion mass spectrometry microscope mode mass spectrometry imaging', *Rapid Communications in Mass Spectrometry*, 27: 2745-50.

Klerk, Leendert A., A. F. Maarten Altelaar, Martin Froesch, Liam A. McDonnell, and Ron M. A. Heeren. 2009. 'Fast and automated large-area imaging MALDI mass spectrometry in microprobe and microscope mode', *International Journal of Mass Spectrometry*, 285: 19-25.

Kudriavtsev, Yu, S. Gallardo, O. Koudriavtseva, A. Escobosa, V. M. Sanchez-R, M. Avendano, R. Asomoza, and M. Lopez-Lopez. 2011. 'SIMS depth profiling of semiconductor interfaces: Experimental study of depth resolution function', *Surface and Interface Analysis*, 43: 1277-81.

Laskin, Julia, Brandi S. Heath, Patrick J. Roach, Lisa Cazares, and O. John Semmes. 2012. 'Tissue Imaging Using Nanospray Desorption Electrospray Ionization Mass Spectrometry', *Anal Chem*, 84: 141-48.

Lee, B. J., M. Baur, C. R. Gebhardt, and M. Duerr. 2013. 'Quantification of the ionization probability during desorption/ionization of oligopeptides induced by neutral cluster impact', *Rapid Communications in Mass Spectrometry*, 27: 1090-94.

Lee, J. L. S., S. Ninomiya, J. Matsuo, I. S. Gilmore, M. P. Seah, and A. G. Shard. 2010. 'Organic Depth Profiling of a Nanostructured Delta Layer Reference Material Using Large Argon Cluster Ions', *Anal Chem*, 82: 98-105.

Luxembourg, S. L., T. H. Mize, L. A. McDonnell, and R. M. A. Heeren. 2004. 'High-spatial resolution mass spectrometric imaging of peptide and protein distributions on a surface', *Anal Chem*, 76: 5339-44.

Luxembourg, Stefan L., Ali R. Vaezaddeh, Erika R. Amstalden, Catherine G. Zimmermann-Ivol, Denis F. Hochstrasser, and Ron M. A. Heeren. 2006. 'The molecular scanner in microscope mode', *Rapid Communications in Mass Spectrometry*, 20: 3435-42.

Mahoney, J. F., Perel, J., Ruatta, S. A., Martino, P. A., Husain, S., Lee, T. D. 1991. 'MASSIVE CLUSTER IMPACT MASS-SPECTROMETRY - A NEW DESORPTION METHOD FOR THE ANALYSIS OF LARGE BIOMOLECULES', *Rapid Communications in Mass Spectrometry*, 5: 441-45.

Mahoney, J. F., J. Perel, T. D. Lee, P. A. Martino, and P. Williams. 1992. 'SHOCK-WAVE MODEL FOR SPUTTERING BIOMOLECULES USING MASSIVE CLUSTER IMPACTS', *Journal of the American Society for Mass Spectrometry*, 3: 311-17.

McDonnell, Liam A., and Ron M. A. Heeren. 2007. 'Imaging mass spectrometry', *Mass Spectrometry Reviews*, 26: 606-43.

Mika, Adriana, Edward Skorkowski, Piotr Stepnowski, and Marek Golebiowski. 2013. 'Identification of Lipid Components in the Abdominal Muscle of Fall-Caught Crangon crangon from a Coastal Area of the Baltic Sea', *Journal of the Brazilian Chemical Society*, 24: 439-48.

Nagle, J. F., and S. Tristram-Nagle. 2000. 'Lipid bilayer structure', *Current Opinion in Structural Biology*, 10: 474-80.

Nelson, R. W., D. Dogruel, and P. Williams. 1994. 'MASS DETERMINATION OF HUMAN-IMMUNOGLOBULIN IGM USING MATRIX-ASSISTED LASER-DESORPTION IONIZATION TIME-OF-FLIGHT MASS-SPECTROMETRY', *Rapid Communications in Mass Spectrometry*, 8: 627-31.

Ninomiya, Satoshi, Lee Chuin Chen, Yuji Sakai, Hiroaki Suzuki, and Kenzo Hiraoka. 2013. 'Development of a high-performance electrospray droplet beam source', *Surface and Interface Analysis*, 45: 126-30.

Ormo, M., A. B. Cubitt, K. Kallio, L. A. Gross, R. Y. Tsien, and S. J. Remington. 1996. 'Crystal structure of the Aequorea victoria green fluorescent protein', *Science*, 273: 1392-95.

Ostrowski, S. G., C. T. Van Bell, N. Winograd, and A. G. Ewing. 2004. 'Mass spectrometric imaging of highly curved membranes during Tetrahymena mating', *Science*, 305: 71-73.

Passarelli, M. K., J. Wang, A. S. Mohammadi, R. Trouillon, I. Gilmore, and A. G. Ewing. 2014. 'Development of an organic lateral resolution test device for imaging mass spectrometry', *Anal Chem*, 86: 9473-80.

Passarelli, Melissa K., Andrew G. Ewing, and Nicholas Winograd. 2013. 'Single-Cell Lipidomics: Characterizing and Imaging Lipids on the Surface of Individual Aplysia californica Neurons with Cluster Secondary Ion Mass Spectrometry', *Anal Chem*, 85: 2231-38.

Piwowar, Alan M., Selda Keskin, Melissa Ortiz Delgado, Kan Shen, Jonathan J. Hue, Ingela Lanekoff, Andrew G. Ewing, and Nicholas Winograd. 2013. 'C60-ToF SIMS imaging of frozen hydrated HeLa cells', *Surface and Interface Analysis*, 45: 302-04.

Porcari, Andreia M., Nicolas V. Schwab, Rosana M. Alberici, Elaine C. Cabral, Damila R. de Moraes, Paula F. Montanher, Christina R. Ferreira, Marcos N. Eberlin, and Jesui V. Visentainer. 2012. 'Intact triacylglycerol profiles of fats and meats via thermal imprinting easy ambient sonic-spray ionization mass spectrometry', *Analytical Methods*, 4: 3551-57.

Romer, Winfried, Ting-Di Wu, Patricia Duchambon, Mohamed Amessou, Daniele Carrez, Ludger Johannes, and Jean-Luc Guerquin-Kern. 2006. 'Sub-cellular localisation of a N-15-labelled peptide vector using NanoSIMS imaging', *Applied Surface Science*, 252: 6925-30.

Schueler, B.; Sander, P.; Reed, D. A. . 1990. 'A time-of-flight secondary ion microscope', *Vacuum*, 41: 1661-64.

Schueler, Bruno W. 1992. 'Microscope imaging by time-of-flight secondary ion mass spectrometry', *Microscopy Microanalysis Microstructures*, 3: 119-39.

Shimma, Shuichi, Yuki Sugiura, Takahiro Hayasaka, Yutaka Hoshikawa, Tetsuo Noda, and Mitsutoshi Setou. 2007. 'MALDI-based imaging mass spectrometry revealed abnormal distribution of phospholipids in colon cancer liver metastasis', *Journal of Chromatography B-Analytical Technologies in the Biomedical and Life Sciences*, 855: 98-103.

Slodzian, G., B. Daigne, F. Girard, F. Boust, and F. Hillion. 1992. 'SCANNING SECONDARY ION ANALYTICAL MICROSCOPY WITH PARALLEL DETECTION', *Biology of the Cell*, 74: 43-50.

Stauber, Jonathan, Luke MacAleese, Julien Franck, Emmanuelle Claude, Marten Snel, Basak Kukrer Kaletas, Ingrid M. V. D. Wiel, Maxence Wisztorski, Isabelle Fournier, and Ron M. A. Heeren. 2010. 'On-Tissue Protein Identification and Imaging by MALDI-Ion Mobility Mass Spectrometry', *Journal of the American Society for Mass Spectrometry*, 21: 338-47.

Steinhauser, Matthew L., Andrew P. Bailey, Samuel E. Senyo, Christelle Guillermier, Todd S. Perlstein, Alex P. Gould, Richard T. Lee, and Claude P. Lechene. 2012. 'Multi-isotope imaging mass spectrometry quantifies stem cell division and metabolism', *Nature*, 481: 516-U131.

Stimpson, B. P., and C. A. Evans. 1978. 'ELECTROHYDRODYNAMIC IONIZATION MASS-SPECTROMETRY - REVIEW OF INSTRUMENTATION, MECHANISMS AND APPLICATIONS', *Journal of Electrostatics*, 5: 411-30.

Stoeckli, M., P. Chaurand, D. E. Hallahan, and R. M. Caprioli. 2001. 'Imaging mass spectrometry: A new technology for the analysis of protein expression in mammalian tissues', *Nature Medicine*, 7: 493-96.

Tanji, N., M. Okamoto, Y. Katayama, M. Hosokawa, N. Takahata, and Y. Sano. 2008. 'Investigation of the cosmetic ingredient distribution in the stratum corneum using NanoSIMS imaging', *Applied Surface Science*, 255: 1116-18.

Thomen, Aurelien, Francois Robert, and Laurent Remusat. 2014. 'Determination of the nitrogen abundance in organic materials by NanoSIMS quantitative imaging', *Journal of Analytical Atomic Spectrometry*, 29: 512-19.

Venter, Andre, Marcela Nefliu, and R. Graham Cooks. 2008. 'Ambient desorption ionization mass spectrometry', *TrAC Trends in Analytical Chemistry*, 27: 284-90.

Weber, P. K., G. A. Graham, N. E. Teslich, W. Moberly Chan, S. Ghosal, T. J. Leighton, and K. E. Wheeler. 2010. 'NanoSIMS imaging of Bacillus spores sectioned by focused ion beam', *Journal of Microscopy*, 238: 189-99.

Winograd, N. 2005. 'The magic of cluster SIMS', *Anal Chem*, 77: 142A-49A.

Zavalin, Andre, Junhai Yang, Kevin Hayden, Marvin Vestal, and Richard M. Caprioli. 2015. 'Tissue protein imaging at 1 mu m laser spot diameter for high spatial resolution and high imaging speed using transmission geometry MALDI TOF MS', *Analytical and Bioanalytical Chemistry*, 407: 2337-42.

Zhang, Jitao, Klaus Franzreb, and Peter Williams. 2014. 'Imaging with biomolecular ions generated by massive cluster impact in a time-of-flight secondary ion microscope', *Rapid Communications in Mass Spectrometry*, 28: 2211-16.

Zhigilei, Leonid. 2001. *Proceedings of the 49th ASMS Conference on Mass Spectrometry and Allied Topics*. Chicago, Illinois.

APPENDIX A

MCI SOURCE SCHEMATICS

Figure A.1. Schematic of Electrospray Reservoir

Reservoir Lid

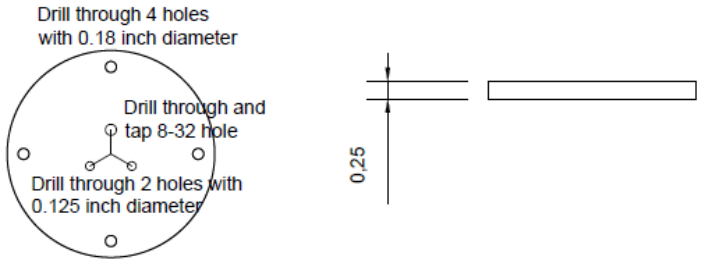

Reservoir Body

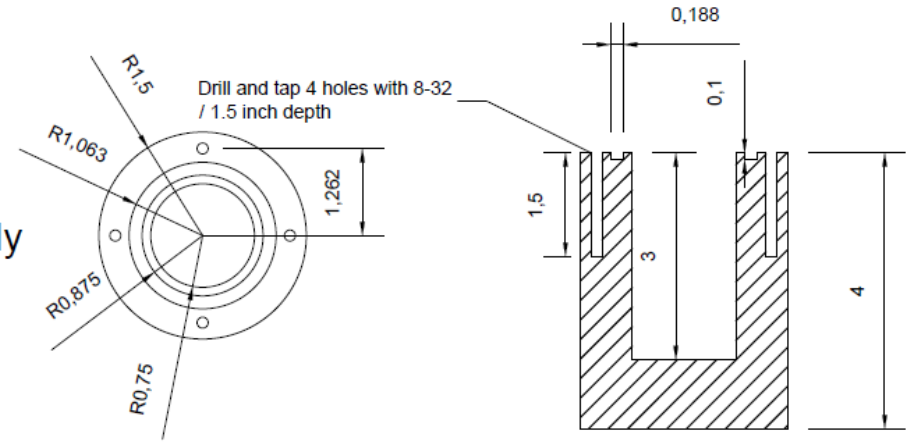

Date: 06/25/2013	Author: Jitao Zhang
Description: Electrospray Reservoir	Unit: Inch
Material: Delrin	Scale: 1/2 X

Figure A.2. Schematic of MCI source flange

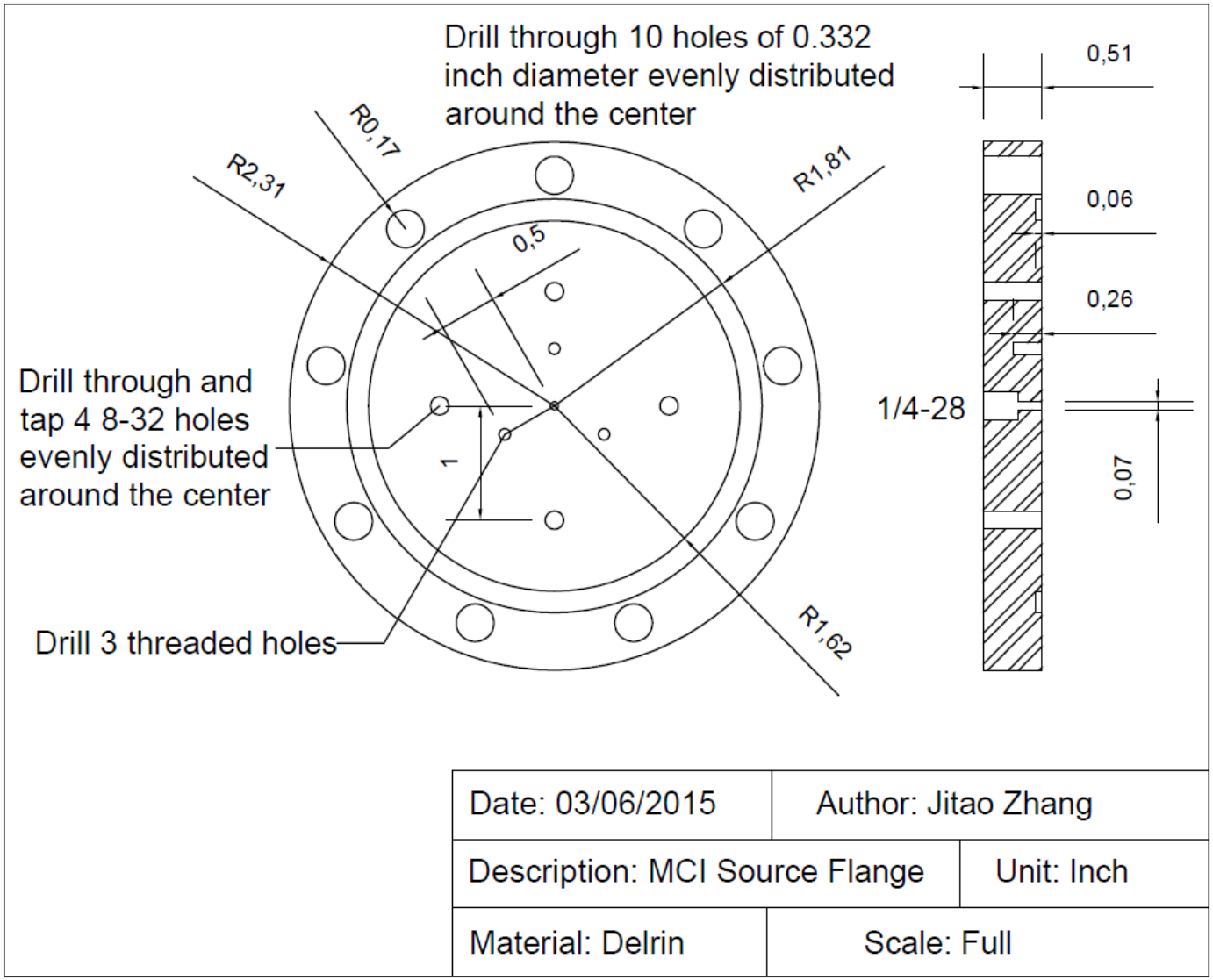

Date: 03/06/2015	Author: Jitao Zhang
Description: MCI Source Flange	Unit: Inch
Material: Delrin	Scale: Full

Figure A.3. Schematic of Extraction Electrode

Drill and tap 2-56 hole with 4mm depth. Drill through a vent hole with 2mm diameter.

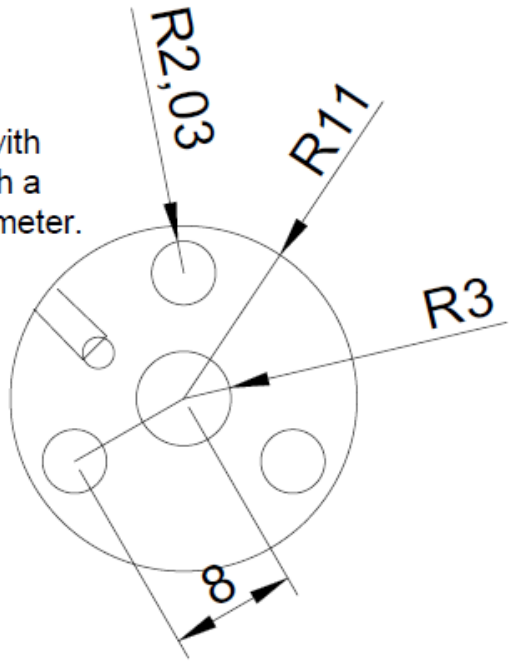

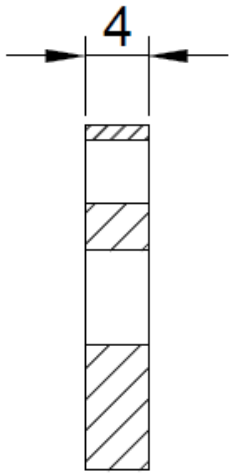

Date:03/18/2013	Author: Jitao Zhang
Description: Extraction Electrode	Unit: mm
Material: Stainless Steel	Scale: 3X